

NATIONAL INSTITUTE FOR FUSION SCIENCE

Line Intensity Ratios of Helium Atom in an Ionizing Plasma

S. Sasaki, M. Goto, T. Kato and S. Takamura

(Received - June 17, 1998)

NIFS-DATA-49

Oct. 1998

RESEARCH REPORT NIFS-DATA Series

This report was prepared as a preprint of compilation of evaluated atomic, molecular, plasma-wall interaction, or nuclear data for fusion research, performed as a collaboration research of the Data and Planning Center, the National Institute for Fusion Science (NIFS) of Japan. This document is intended for future publication in a journal or data book after some rearrangements of its contents.

Inquiries about copyright and reproduction should be addressed to the Research Information Center, National Institute for Fusion Science, Nagoya 464-01, Japan.

NAGOYA, JAPAN

Line intensity ratios of helium atom in an ionizing plasma

Satoshi Sasaki

Machinery and Equipment Department, Toshiba Corporation, 2-4 Suehiro-cho, Tsurumi-ku, Yokohama 230-0045, Japan
E-mail: bin.sasaki@toshiba.co.jp

Motoshi Goto, and Takako Kato

National Institute for Fusion Science, Toki 509-5202, Japan

Shuichi Takamura

Department of Energy Engineering and Science, Nagoya University, Nagoya 464-01, Japan

Abstract

Effective emission rate coefficients $C_{em}^{eff}(\lambda)$, line intensity ratios, $C_{em}^{eff}(\lambda_1) / C_{em}^{eff}(\lambda_2)$, and $S_{eff}^{eff} / C_{em}^{eff}(\lambda)$, with S_{eff} the ionization rate coefficient, are obtained by the collisional radiative model for an ionizing plasma using new excitation and ionization rate coefficients. In the plasma with electron density $n_e > 10^4 \text{ cm}^{-3}$, $C_{em}^{eff}(\lambda)$ for various lines are enlarged, since the normalized population densities for the metastable states, $n(2^{1,3}S)/n_{He}$, becomes large, and the excitation rate coefficients from $2^{1,3}S$, $C_{2^{1,3}S \rightarrow i}$, are large compared to that from the ground state $C_{1^1S \rightarrow i}$. In high n_e plasma ($n_e > 10^{12} \text{ cm}^{-3}$), with frequent electron impacts on the excited heliums, $n(i)/n_{He}$ become constant to n_e , which results in the decrease of $C_{em}^{eff}(\lambda)$. Hot electrons and resonance scattering, which are often important for the experimental applications, are included in this model. A small amount of hot electrons (several percents) can enhance the line emission and ionization rates for low electron temperature plasma with T_e ($T_e < 10 \text{ eV}$). The resonance scattering reduces the emission of the resonance lines ($1^1S - n^1P$) and enlarges n^1P and 2^1S populations when the column density of helium gas $n_{He} \times L$ exceeds $2 \times 10^{13} [\text{cm}^{-2}]$.

Key words: helium atom, plasma diagnostics, line intensity ratio, collisional radiative model, hot electrons, resonance scattering

I. INTRODUCTION

Helium atom is an attractive atomic species for electron temperature (T_e) and density (n_e) measurements, since it has various advantages as a probe particle, i.e., well-known atomic data, strong visible lines, and an intrinsic species in the fusion burning plasma. So far, T_e measurement technique using He I line intensity ratios has been developed and improved [1-7]. Recently, n_e and T_e measurements based on the collisional radiative (C.R.) model for helium atom [8] have been applied to the TEXTOR tokamak [9], the PSI-1 linear device [10], and the NAGDIS-I linear device [11-13]. Helium is also important for the fusion plasma from the viewpoints of

fuel dilution and energy balances [14]. The C.R. model, which involves excited heliums and various plasma particles such as electrons, ions, atoms, molecules, is indispensable for the investigations of the fusion plasmas with high $n_e (> 10^{12} \text{ cm}^{-3})$. A numerical code of the C.R. model for helium atom is developed by Fujimoto [8], and various improvements were made [12]. In this work, the C.R. model was revised using recommended excitation and ionization rate coefficients [15-19].

Hot electron or superthermal electrons sometimes exist in the RF and DC glow discharge as well as the fusion edge, and play an important role on the plasma confinement and the sheath formations [20,21]. Hot electrons are also important for the spectroscopic diagnostics, since they have a large contribution on the excitation processes [12]. In the typical helium glow discharge plasma, with pressure above 10^{-4} Torr, the resonance scattering or imprisonment of resonance lines apparently reduces transition probabilities A_{ij} , which reduces the emission of resonance lines ($1^1S - n^1P$) and enlarges n^1P and 2^1S populations [22]. The reduction of A_{ij} is included in this model using an optical escape factor $\Lambda(\lambda)$ [23,24]. It has been reported that the increase of 501.6 nm line emission ($2^1S - 3^1P$) is consistent with the C.R. model in NAGDIS-I [12].

The ratio of the effective rate coefficient for ionization to that for emission, $S_{eff}^{eff} / C_{em}^{eff}(\lambda)$, is often used for the density determination of the probe atomic beams in the plasma, and the measurement of impurity flux released from the wall. So far, the n_e measurement using Li beam, and the T_e measurement using Al, Ti, C, and He beams using $S_{eff}^{eff} / C_{em}^{eff}(\lambda)$ have been developed [7,26].

II. COLLISIONAL RADIATIVE MODEL AND NORMALIZED POPULATION DENSITIES

The population densities $n(i)$ are derived from the numerical code by Fujimoto [8] revised by the recommended rate coefficients for ionization and excitations from the ground state 1^1S and the two metastable states $2^{1,3}S$ [15-19]. The excited states with principal quantum number $n \leq 20$ are included in this work as shown in Fig. 1. Energy levels $E(i)$ for the excited states with $n \leq 7$ are

summarized in Table I [25]. Excited states with $n = 8 - 20$ are grouped by the same principal quantum numbers as shown in Fig. 1 and Table II. In the C.R. model for the ionizing plasma, rate equations for the population density $n(i)$ are expressed as,

$$\frac{dn(i)}{dt} = \left(n_e \sum_{k \neq i} C_{ki} n(k) + \sum_{k > i} A_{ki} n(k) \right) - \left(n_e \sum_{k \neq i} C_{ik} n(i) + \sum_{k < i} A_{ik} n(i) \right) - n_e S_i n(i) = 0, \quad (1)$$

where A_{ij} is the transition probability for $i \rightarrow j$ transition [s^{-1}]. The wavelengths λ and A_{ij} for the lines presented in this article are summarized in Table III [25]. The C_{ij} and S_i are the excitation/de-excitation rate coefficients, and the ionization rate coefficient for electron impact, respectively. The population densities $n(i)$ are obtained by solving the rate equations for all excited states with putting $dn(i)/dt = 0$. The normalized population density is defined as $n(i)/n_{He}$, with n_{He} the density of helium atom ($n_{He} = \sum_k n(k)$).

Figure 2.1 (a) and (b) show the T_e and n_e dependences of $n(i)/n_{He}$ for 2^1S and 2^3S , and the sum of $n(i)/n_{He}$ for singlet and triplet, $\sum_s n(s)/n_{He}$ (s:singlet, $E(s) > E(2^1S)$) and $\sum_t n(t)/n_{He}$ (t:triplet, $E(t) > E(2^3S)$). Population balance involving 2^1S is shown as percentage contributions of electron in/out flows in Fig. 2.2. For low n_e ($n_e \leq 10^5 \text{ cm}^{-3}$), population balance can be described with neglecting radiative electron in flows ($\leq 5\%$), described as,

$$n_e C_{1^1S \rightarrow 2^1S} \frac{n(1^1S)}{n_{He}} = A_{2^1S \rightarrow 1^1S} \frac{n(2^1S)}{n_{He}}, \quad (2)$$

which gives the relation of $n(2^1S)/n_{He}$ proportional to n_e . For $n_e > 10^8 \text{ cm}^{-3}$ (middle n_e region), excitations to the singlet states, and ionization becomes dominant processes as follows:

$$n_e C_{1^1S \rightarrow 2^1S} \frac{n(1^1S)}{n_{He}} = n_e \left(\sum_{s:\text{singlet}} C_{2^1S \rightarrow s} + S_{2^1S} \right) \frac{n(2^1S)}{n_{He}}, \quad (3)$$

which gives constant $n(2^1S)/n_{He}$. As n_e exceeds 10^{13} cm^{-3} , $n(2^1S)/n_{He}$ increases with n_e due to the de-excitations from the singlet excited states down to 2^1S . In very high n_e plasma ($n_e > 10^{16} \text{ cm}^{-3}$), the population balances are determined by the collisional processes between 2^1S and all singlet states:

$$n_e \sum_{s:\text{singlet}} C_{s \rightarrow 2^1S} \frac{n(s)}{n_{He}} = n_e \left(\sum_{s:\text{singlet}} C_{2^1S \rightarrow s} + S_{2^1S} \right) \frac{n(2^1S)}{n_{He}}. \quad (4)$$

Figure 2.3 shows the percentage contributions of the electron in/out flows to/from 2^3S . In the low n_e plasma ($n_e \leq 10^6 \text{ cm}^{-3}$), the population balance involving 2^3S can be approximated as,

$$\begin{aligned} \left(\sum_n A_{n^3P \rightarrow 2^3S} \frac{n(n^3P)}{n_{He}} \right) &\approx \sum_n n_e C_{1^1S \rightarrow n^3P} \frac{n(1^1S)}{n_{He}} \\ &= A_{2^3S \rightarrow 1^1S} \frac{n(2^3S)}{n_{He}}. \end{aligned} \quad (5)$$

Since the radiative de-excitation can be replaced by the $1^1S - n^3P$ excitations, $n(2^3S)/n_{He}$ is proportional to n_e . For $n_e > 10^6 \text{ cm}^{-3}$, excitation to the triplets and ionization become the dominant out-flows as follows:

$$\begin{aligned} \left(\sum_n A_{n^3P \rightarrow 2^3S} \frac{n(n^3P)}{n_{He}} \right) &\approx \sum_n n_e C_{1^1S \rightarrow n^3P} \frac{n(1^1S)}{n_{He}} \\ &= n_e \left(\sum_{t:\text{triplet}} C_{2^3S \rightarrow t} + S_{2^3S} \right) \frac{n(2^3S)}{n_{He}}, \end{aligned} \quad (6)$$

which gives constant $n(2^3S)/n_{He}$ independent to n_e ($\approx 5 \times 10^{-3}$ at $T_e = 20 \text{ eV}$). For high n_e plasma ($n_e \geq 10^{12} \text{ cm}^{-3}$), the radiative electron in-flows to 2^3S becomes small, and the population balance is described as,

$$\begin{aligned} n_e \sum_{t:\text{triplet}} C_{t \rightarrow 2^3S} \frac{n(t)}{n_{He}} + n_e C_{1^1S \rightarrow 2^3S} \frac{n(1^1S)}{n_{He}} \\ = n_e \left(\sum_{t:\text{triplet}} C_{2^3S \rightarrow t} + S_{2^3S} \right) \frac{n(2^3S)}{n_{He}}, \end{aligned} \quad (7)$$

where $n(2^3S)/n_{He}$ is smaller compared to that in the middle n_e region ($\approx 3 \times 10^{-4}$ at $T_e = 20 \text{ eV}$).

Figures 2.4 and 2.5 show T_e and n_e dependences of $n(i)/n_{He}$ for several singlet (2^1P , 3^1S , 3^1P , 4^1D) and triplet (2^3P , 3^3S , 3^3P) excited states. The T_e dependences of $n(i)/n_{He}$ are similar to those for $C_{1^1S \rightarrow i}$. The T_e dependences of $n(i)/n_{He}$ for the triplet have a peak around $T_e = 20 \text{ eV}$ and gradually decrease with T_e for $T_e > 20 \text{ eV}$, while those for the singlet monotonously increase with T_e for $T_e < 1000 \text{ eV}$. Figure 2.6 shows the population balance involving 4^1D , for example. The radiative electron in-flows, which is often called as "cascade", $\sum_s A_{s \rightarrow 4^1D} n(s)/n_{He}$, is larger than 10 % of the total electron in-flows for $n_e < 10^{11} \text{ cm}^{-3}$. As n_e exceeds 10^{13} cm^{-3} , the population balance is determined by the collisional processes between 4^1D and the singlet states with $n \geq 3$.

III. EFFECTIVE EMISSION RATE COEFFICIENTS

The effective emission rate coefficient in the C.R. model $C_{em}^{eff}(\lambda) [\text{cm}^3/\text{s}]$ is defined as,

$$C_{em}^{eff}(\lambda; i \rightarrow j) = \frac{A_{ij}n(i)}{n_e \sum_k n(k)} = \frac{A_{ij}n(i)}{n_e n_{He}}. \quad (8)$$

Photon production rate per unit volume is given as $n_e C_{em}^{eff}(\lambda) n_{He}$ [cm⁻³s⁻¹]. The $C_{em}^{eff}(\lambda)$ for various lines, $1^1S - n^1P$, $2^1P - n^1S$, $2^1S - n^1P$, $2^1P - n^1D$, $2^3P - n^3S$, $2^3S - n^3P$, and $2^3P - n^3D$ are shown as T_e and n_e dependences in Figs. 3.1 - 3.7.

The $C_{em}^{eff}(58.4 \text{ nm}; 1^1S - 2^1P)$, for the resonance line, is almost constant for a wide n_e range ($n_e \leq 10^{14} \text{ cm}^{-3}$) because of large value of $A_{2^1P \rightarrow 1^1S}$. It is slightly enlarged by the excitation from 2^1S for $n_e = 10^7 - 10^{14} \text{ cm}^{-3}$. As n_e exceed 10^{14} cm^{-3} , where the rate for collisional de-excitations becomes large compared to those for radiations, $C_{em}^{eff}(58.4 \text{ nm})$ gradually decreases because $n(i)/n_{He}$ becomes almost constant. The $C_{em}^{eff}(\lambda)$ for the other lines with small $\Sigma_k A_{ik}$ have small critical densities ($n_e = 10^{11} - 10^{12} \text{ cm}^{-3}$). The 2^1S metastable state slightly influences on the $n = 3$ or n^1D lines, e.g. 58.4 nm ($2^1S - 3^1P$), 728.1 nm ($2^1P - 3^1S$), 667.8 nm ($2^1P - 3^1D$), and 492.2 nm ($2^1P - 4^1D$). For the triplet lines, 2^3S has a big influences on n_e dependence of $C_{em}^{eff}(\lambda)$, since $C_{2^3S \rightarrow t}$ is much larger than $C_{1^1S \rightarrow t}$ (from the ground state).

IV. LINE INTENSITY RATIOS

The line intensity ratios, $C_{em}^{eff}(\lambda_1)/C_{em}^{eff}(\lambda_2)$, for the use of n_e and T_e measurements are shown in Figs. 4.1 - 4.6. Figure 4.1 shows T_e and n_e dependences of the line intensity ratios for singlet - triplet line pairs, 504.8 nm ($2^1P - 4^1S$) / 471.3 nm ($2^3P - 4^3S$), 501.6 nm ($2^1S - 3^1P$) / 471.3 nm, and 492.2 nm ($2^1P - 4^1D$) / 471.3 nm, whose wavelengths are around 500 nm. Since $C_{em}^{eff}(\lambda)$ for the singlet and triplet lines have different T_e dependences each other, the line intensity ratios have strong T_e dependences, which are suitable for T_e measurement. As n_e exceeds 10^4 cm^{-3} , these line intensity ratios are slightly decreased by the increase of $C_{em}^{eff}(471.3 \text{ nm})$ due to the enhanced excitation from 2^3S . The 504.8 nm / 471.3 nm line intensity ratio has an advantage of relatively weak n_e dependence compared to the other ones in high n_e plasma ($n_e \geq 10^{11} \text{ cm}^{-3}$). Figure 4.2 shows the T_e dependences of these line intensity ratios for $T_e = 5 - 50 \text{ eV}$ for the experimental applications. Figure 4.3 shows T_e and n_e dependences of the singlet - singlet intensity ratios of 501.6 nm / 504.8 nm, 501.6 nm / 492.2 nm, and 492.2 nm / 504.8 nm. The strong n_e dependences for $n_e \geq 10^{11} \text{ cm}^{-3}$ and weak T_e dependence due to the similar T_e dependence of $C_{em}^{eff}(\lambda)$ is suitable for n_e measurement. Figure 4.4 shows n_e dependences of these line intensity ratios for $n_e = 10^9 - 10^{14} \text{ cm}^{-3}$.

Figure 4.5 shows T_e and n_e dependences of the line intensity ratios of 728.1 nm ($2^1P - 3^1S$) / 706.5 nm ($2^3P - 3^3S$), 667.8 nm ($2^1P - 3^1D$) / 706.5 nm, and 667.8 nm / 728.1 nm, whose wavelengths are around 700 nm. Since $C_{em}^{eff}(706.5 \text{ nm})$ is enlarged due to the large $n(2^3S)/n_{He}$, the line intensity ratios of 728.1 nm / 706.5 nm and 667.8

nm / 706.5 nm are slightly reduced for $n_e = 10^6 - 10^{12} \text{ cm}^{-3}$. The 728.1 nm / 706.5 nm line intensity ratio is suitable for the T_e measurement in high n_e plasma due to the small n_e dependence. The T_e dependences of the 728.8 nm / 706.5 nm and 667.8 nm / 706.5 nm for $T_e = 5 - 50 \text{ eV}$ and the n_e dependence of the 667.8 nm / 728.1 nm line intensity ratio for $n_e = 10^9 - 10^{14} \text{ cm}^{-3}$ are shown in Fig. 4.6.

Simultaneous T_e and n_e measurements are available by using singlet - singlet and singlet - triplet line pairs. Firstly, n_e is obtained from the singlet - singlet intensity ratio with assuming T_e . Secondly, T_e is obtained from the singlet - triplet line pairs with using n_e obtained from the singlet - singlet ratios. It is recommend to use the 492.2 nm / 504.8 nm intensity ratio for n_e measurement and 504.8 nm / 471.3 nm for T_e measurement. Detailed data of the intensity ratios are shown in Appendix A as contour plots and n_e and T_e dependences.

V. RATIO OF EFFECTIVE RATE COEFFICIENT FOR IONIZATION TO THAT OF LINE EMISSION

The quantity of $S_{eff}/C_{em}^{eff}(\lambda)$, with S_{eff} the effective ionization rate coefficient, is often used for the density determination of the atomic beam in a plasma [7]. The effective ionization rate coefficient S_{eff} is defined as,

$$S_{eff} = \frac{\sum_i S_i n(i)}{\sum_k n(k)} = \frac{\sum_i S_i n(i)}{n_{He}}. \quad (9)$$

Since S_i (from the excited state) are larger than S_{1^1S} (from the ground state), S_{eff} is greater than S_{1^1S} . The T_e and n_e dependences of S_{eff} are shown in Fig. 5.1. In the plasma with $T_e > 20 \text{ eV}$, S_{eff} has small n_e dependence. For low T_e plasmas ($T_e \leq 20 \text{ eV}$), however, n_e dependence is strong due to small value of S_{1^1S} , while S_i from the excited states including 2^1S and 2^3S are large as shown in Fig. B4. S_{eff} is enlarged due to the ionization from 2^3S for $n_e = 10^6 - 10^{13} \text{ cm}^{-3}$. As n_e exceeds 10^{13} cm^{-3} , S_{eff} increases with n_e due to the ionizations from various excited states.

In this technique, the density of the helium atomic beam n_{He} is obtained from the line intensity $I_{He}(z)$, which is expressed by,

$$I_{He}(z) = n_e C_{em}^{eff}(\lambda) n_{He} \eta, \quad (10)$$

where z and η are the position along the beam and the sensitivity of the optical detector, respectively. For the monochromatic helium atomic beam with velocity of v_{He} , beam attenuation due to the ionization is described as,

$$\frac{dn_{He}}{dt} = \frac{dn_{He}}{dz} v_{He} = -n_e S_{eff} n_{He}. \quad (11)$$

Helium atoms injected into the plasma are ionized and removed away from the beam with trapped by the magnetic field, usually perpendicular to the beam. By using eqs. (10) and (11), $n_{He}(z)$ is given by,

$$n_{He}(z) = \frac{\int_z \frac{S^{eff}}{C_{em}^{eff}(\lambda)} I_{He}(\zeta) d\zeta}{v_{He}\eta}. \quad (12)$$

Figures 5.2 - 5.7 show T_e and n_e dependences of $S^{eff}/C_{em}^{eff}(\lambda)$ for various visible lines. The line of 501.6 nm ($2^1S - 3^1P$) is attractive because of its small n_e and T_e dependences for $n_e \leq 10^{13} \text{ cm}^{-3}$ and $T_e \geq 5 \text{ eV}$.

VI. EFFECT OF HOT ELECTRON IN A PLASMA

For the investigation of hot electrons in a plasma, we consider two temperature plasma with electron temperature of T_{ec} and T_{eh} for cold and hot components. The electron velocity distribution function $f(v_e)$ is expressed as a superposition of two Maxwellians, $f_c(v_e)$ and $f_h(v_e)$ with electron temperature of T_{ec} and T_{eh} :

$$f(v_e) = (1 - \alpha)f_c(v_e) + \alpha f_h(v_e), \quad (13)$$

where α is the abundance of the hot component given by $\alpha = n_{eh}/n_e$, with n_{eh} the density of the hot electron component. Then, C_{ij} is expressed as,

$$\begin{aligned} C_{ij} &= \int_0^\infty \sigma_{ij} v_e f(v_e) 4\pi v_e^2 dv_e \\ &= (1 - \alpha)C_{ij}(T_{ec}) + \alpha C_{ij}(T_{eh}), \end{aligned} \quad (14)$$

where $C_{ij}(T_{ec})$ and $C_{ij}(T_{eh})$ are C_{ij} at T_{ec} and T_{eh} , respectively. In the similar way, the ionization rate coefficient S_i can be obtained as $S_i = (1 - \alpha)S_i(T_{ec}) + \alpha S_i(T_{eh})$.

Examples of $C_{em}^{eff}(\lambda)$ for 54.8 nm and 667.8 nm, $C_{em}^{eff}(\lambda_1) / C_{em}^{eff}(\lambda_2)$ for 504.8 nm / 471.3 nm and 492.2 nm / 471.3 nm, and S^{eff} in the presence of hot electrons with $T_{eh} = 20 \text{ eV}$ and 40 eV at $\alpha = 10\%$ are shown in Figs. 6.1 - 6.3. Since C_{1^1S-i} and S_{1^1S} (from the ground state) are very small for $T_e \leq 3 \text{ eV}$, $C_{em}^{eff}(\lambda)$ and S^{eff} at $\alpha = 10\%$ are rather similar to $0.1 \times C_{em}^{eff}(\lambda)$ and $0.1 \times S^{eff}$ at $T_e = T_{eh}$, respectively. The hot electrons are very important for the T_e measurement in a low T_{ec} plasma ($T_{ec} < 10 \text{ eV}$), since the experimental result seems like a monochromatic temperature plasma with $T_e = T_{eh}$.

VII. EFFECT OF RESONANCE SCATTERING BY THE HELIUM GAS

In the typical helium discharge plasma, with pressure above 10^{-4} Torr , helium gas has large optical depths $\tau(\lambda)$ for the resonance lines ($1^1S - n^1P$). Figure 7.1 shows $\tau(\lambda)$ for 58.4 nm ($1^1S - 2^1P$), 53.7 nm ($1^1S - 3^1P$), and 52.2 nm ($1^1S - 4^1P$) in the helium gas with 300 K (room temperature). This figure suggests we must consider the resonance scattering when the column density $n_{He} \times L$ exceeds 10^{13} cm^{-2} , since $\tau(58.4 \text{ nm})$ exceeds unity. It corresponds to the helium gas pressure of $2.8 \times 10^{-5} \text{ Torr}$ in the vacuum vessel with radius of $L = 10 \text{ cm}$. The

effects of resonance scattering are included in this model using an optical escape factor $\Lambda(\lambda)$, which is obtained by the following formulae for large $\tau(\lambda)$ [22-24, 28]:

$$\Lambda(\lambda) = \frac{1}{\tau(\lambda)\sqrt{\pi \ln(\tau(\lambda))}}. \quad (15)$$

The optical escape factor $\Lambda(\lambda)$ has a value of $\Lambda(\lambda) < 1$, and $\Lambda(\lambda) = 1$ corresponds $\tau(\lambda) = 0$. The resonance scattering is included in the model using $\Lambda(\lambda) \times A_{ij}$ instead of A_{ij} . The $\Lambda(\lambda)$ for 58.4 nm, 53.7 nm and 52.2 nm included in this model are shown in Fig. 7.1. Photon absorptions by the metastable states $2^1, 3^1S$ and the other excited states are neglected because the population densities and the absorption coefficients are small.

Figure 7.2 shows the modifications of $n(i)/n_{He}$ for 2^1S , 2^3S , 2^1P , 3^1P , and 4^1P by the resonance scattering at $n_e = 10^{12} \text{ cm}^{-3}$ and $T_e = 20 \text{ eV}$. The $n(n^1P)/n_{He}$ are enhanced by the reduction of $\Lambda(\lambda; 1^1S - n^1P)$, resulting in the increase of $C_{em}^{eff}(\lambda; 2^1S - n^1P)$ and $n(2^1S)/n_{He}$. The $C_{em}^{eff}(\lambda)$ for the resonance lines, 53.7 nm and 52.2 nm, decrease with $n_{He} \times L$ because of the reduction of $\Lambda(\lambda)$ as shown in Fig. 7.3. The $C_{em}^{eff}(\lambda)$ for the $2^1P - n^1D$ and $2^1P - n^1S$ lines are enlarged by the excitations from the $n(2^1S)/n_{He}$ and $n(n^1P)/n_{He}$. Line intensity ratios are shown in Fig. 7.4 as a function of $n_{He} \times L$. The $C_{em}^{eff}(501.6 \text{ nm})$ is very sensitive to the resonance scattering for $n_{He} \times L > 2 \times 10^{13} \text{ cm}^{-2}$. Figure 7.5 shows the increase of S^{eff} because of the enlargement of $n(i)/n_{He}$ for 2^1S and the other excited states.

VIII. DISCUSSION

A. Accuracy of data

The accuracy of $C_{em}^{eff}(\lambda)$, $C_{em}^{eff}(\lambda_1) / C_{em}^{eff}(\lambda_2)$, S^{eff} , and $S^{eff}/C_{em}^{eff}(\lambda)$ primarily depends on the reliability of atomic data. The transition probability A_{ij} has a good accuracy within 5 %. The accuracy of C_{ij} and S_i from the ground state can be estimated within 10 - 20 % for $T_e \leq 50 \text{ eV}$ by including the analytical fitting error [15-18]. For $T_e \geq 50 \text{ eV}$, C_{ij} has a better accuracy because of less uncertainty of excitation cross sections σ_{ij} for high electron impact energy, especially for the allowed excitations. So, we can estimate the accuracy of $C_{em}^{eff}(\lambda)$ and S^{eff} within 10 - 20 % for low n_e plasma ($n_e < 10^4 \text{ cm}^{-3}$), where excitation and ionization from the ground state are the dominant process to determine those quantities.

As n_e exceeds 10^4 cm^{-3} , the reliability of atomic data for the atomic processes involving the excited states becomes important. Shevelko has compared his model calculations to various theoretical and experimental data of σ_{ij} from the excited states including 2^1S and 2^3S [19]. The accuracy for the excitation data involving metastable and excited states will be within 20 - 50 %, and $C_{em}^{eff}(\lambda)$ will have accuracy of the same values. The number of

excited states included in the calculation ($n \leq 20$) is sufficient for the investigation of the lines with $n \leq 4$.

B. Comparison of line intensity ratios to the other works

The line intensity ratios presented by Schweer [9], and Behrendt [10], including the excited states with principal quantum number $n \leq 4$, are compared to this work (including $n \leq 20$). Figure 8.1(a) compares the 667.8 nm / 728.1 nm intensity ratios to Schweer's. The line intensity ratios obtained including and removing $n > 4$ excited states in this work have small discrepancy each other, within $\pm 10\%$ at $n_e = 10^{11} \text{ cm}^{-3}$. Discrepancy between this work and Schweer's at $n_e = 10^{11} \text{ cm}^{-3}$ is as large as factor of two, which may come from the difference in $C_{1^1S \rightarrow i}$ (from the ground state) and $n(2^{1,3}S)/n_{He}$. Figure 8.1(b) compares the 501.6 nm / 504.8 nm intensity ratio to Behrendt's work. The contribution of $n > 4$ excited states is small for $n_e \leq 10^{13} \text{ cm}^{-3}$, but rapidly increases for $n_e > 10^{13} \text{ cm}^{-3}$. Behrendt's result is in good agreement to this work within 5 - 10 % for $n_e = 10^{11} - 10^{13} \text{ cm}^{-3}$ [10]. Figure 8.1(c) compares the 728.1 nm / 706.5 nm intensity ratio to Schweer's at $n_e = 10^{12} \text{ cm}^{-3}$. The discrepancy may come from the difference in the T_e dependence of $C_{1^1S \rightarrow i}$.

These results show the accuracy of line intensity ratio is very important for the T_e and n_e measurements. Only several tens percent difference in the line intensity ratio results in several factor and one order of deviations in T_e and n_e determination, respectively. The accuracy of atomic data especially for C_{ij} from the excited states including $2^{1,3}S$ is important as well as the contribution of excited states with $n > 4$.

C. Recombination of helium ions

This work considers pure ionizing plasma and neglect recombination of the helium ions. In the low T_e or high n_e plasma, however, the recombination of helium ions is not negligible on the population balance. By including recombinations, the population density $n(i)$ is expressed as $n(i) = n(i)_{ion} + n(i)_{rec}$, the sum of pure ionizing and recombining components $n(i)_{ion}$ and $n(i)_{rec}$. Figure 8.2 shows $n(i)_{rec}/n(i)$ for 4^1D and 4^3S in the plasma with $n_{He^+}/n_{He} = 0.1$, where n_{He^+} is the density of He^+ ions. The ratio of $n_{He^+}/n_{He} = 0.1$ is an example in the NAGDIS-I helium discharge plasma with $T_e = 8 - 20 \text{ eV}$ and $n_e = 10^{11} - 4 \times 10^{12} \text{ cm}^{-3}$. For low T_e ($\leq 5 \text{ eV}$) or very high n_e ($> 10^{17} \text{ cm}^{-3}$), recombination cannot be neglected. Figure 8.3 shows the influence of recombination on the several line intensity ratios at $n_e = 10^{14} \text{ cm}^{-3}$, which shows the recombination can be neglected for $T_e \geq 3 - 5 \text{ eV}$.

D. Relaxation time of the population densities

The population densities of the metastable states, 2^1S and 2^3S , have large relaxation times, since $A_{21,3S \rightarrow 1^1S}$ (to the ground state) are very small, e.g. $A_{2^3S \rightarrow 1^1S} = 1.7 \times 10^{-4} \text{ s}^{-1}$ [27]. Then, the relaxation times of the $2^{1,3}S$ metastable states can be estimated as $\approx 1/n_e S_{21,3S}$ in the middle or high density plasma, where $n_e S_{21,3S} > A_{21,3S \rightarrow 1^1S}$. Here, the ionization is considered to have a largest contribution on the population balance because of the large values of $S_{21,3S}$ (e.g. $S_{2^3S} \approx 10^{-7} \text{ cm}^3/\text{s}$ at $T_e = 20 \text{ eV}$). As suggested by the n_e dependence of $C_{em}^{eff}(\lambda)$, the contributions of 2^1S on the singlet populations are small. The relaxation times for the singlets can be estimated as $\approx 1/A_{ij}$ (\approx several tens of nanoseconds), while those for the triplets depend on the relaxation time of $n(2^3S)/n_{He}$.

IX. EXPERIMENTAL APPLICATIONS OF T_e AND N_e MEASUREMENTS

A. Limitations for the experimental applications

T_e and n_e measurement technique using He I line intensity ratios neglects several factors which can deteriorate the accuracy of measurements such as,

- a) hot electrons in a plasma,
- b) recombinations of helium ions,
- c) atomic or molecular processes modifying population balance of helium atoms not include in the model,
- d) resonance scattering by ambient helium gas,
- e) movement of helium atoms in the plasma.

Here, the limitations of this technique due to these factors are discussed.

(a) Since the rate coefficient C_{ij} is obtained for Maxwellian velocity distribution function, it is inherently impossible to discriminate hot electron component from the thermalized one. This method is rather sensitive to hot electrons especially for $T_e < 10 \text{ eV}$, compared to standard T_e measurement methods such as Langmuir probe and Thomson scattering. However, it can be a good indication of existence of hot electrons if we can measure T_e of cold or thermalized component by the other method [12]. It also may be useful for the investigation of hot electrons in the R.F. heated plasma where hot electrons are often produced.

(b) Population balances for the recombining plasma is quite different from those for the ionizing plasma. Empirically, the contribution of recombination can be neglected for $T_e > 1/3 \times E_i$ ($E_i = 24.6 \text{ eV}$) for volume recombination. For the beam probe application, where a small amount of helium atom is injected into the plasma, the recombination can be neglected since the helium ions are quickly removed away with trapped by the magnetic

fields [9,10]. Surface recombination should be also considered for the wall facing regions in relation to the movement of recombined helium atoms.

(c) Complicated atomic processes such as charge transfer from/to various atoms and molecules or ion impact excitation and ionization can modify the population balances [29]. Proton impact must be included for high temperature hydrogen plasma (> several hundreds eV) and for the fast helium atomic beam experiment [18].

(d) The resonance scattering influences the populations balances as a column density of the helium gas $n_{He} \times L$ exceeds $2 \times 10^{13} \text{ cm}^{-2}$, which corresponds partial pressure of helium gas of 10^{-5} Torr for $L = 10 \text{ cm}$. For the cylindrical plasma, L corresponds to the radius of vacuum vessel. Reducing partial pressure of helium gas or using helium beam probe technique will solve this problem, although we should note various atomic processes involving atoms and ions in the target plasma.

(e) Movement of helium atom must be considered for low n_e plasma with large relaxation time τ_{relax} or fast beam application with high helium velocity v_{He} , where $v_{He} \times \tau_{relax}$ is comparable or larger than the spatial length we concerned. For the plasma with low n_e or small vacuum vessel, where $v_{He} \times \tau_{relax}$ is comparable to the dimensions of the vacuum vessel, population balances involving $2^3 S$ metastable states will be modified. The spatial resolution of this method concerns with $v_{He} \times \tau_{relax}$, which is important for the fast beam application. Line intensity ratio data with the parameter of $n(2^1,3S)/n_{He}$ are necessary to obtain high spatial resolution. So far, the time dependent population behavior has been considered for the fast He beam probe spectroscopy in TEXTOR [9].

B. Experimental error of T_e and n_e measurements

Here, the experimental error of T_e and n_e measurement with assuming the limitations discussed above are solved. For example, errors in the T_e measurement using the 492.2 nm / 471.3 nm line intensity ratio, Fig. 4.2(c), is considered for a target plasma with $T_e = 20 \text{ eV}$ and $n_e = 10^{12} \text{ cm}^{-3}$. The theoretical error due to the reliability of $C_{em}^{eff}(\lambda)$ is estimated within 20 %, giving the resultant T_e error of $\pm 4 \text{ eV}$. Adding 10 % of the experimental error on the reliability of atomic data results in $\pm 7 \text{ eV}$ error. The uncertainty of n_e as much as a factor of two, for example $5 \times 10^{11} - 2 \times 10^{12} \text{ cm}^{-3}$, gives a deviation in the 492.2 nm / 471.3 nm line intensity ratio of $\pm 25 \%$. Then, the resultant T_e error can be estimated as $\pm 8 \text{ eV}$. The error in n_e measurements is considered with the 492.2 nm / 504.8 nm line intensity ratio. The reliability of $C_{em}^{eff}(\lambda_1)/C_{em}^{eff}(\lambda_2)$ is within 20 - 50 % for $n_e > 10^{10} \text{ cm}^{-3}$. Then, the resultant n_e error reaches up to a factor of 1.5 - 2 by adding the experimental error of $\pm 10 \%$. The uncertainty of T_e gives small variation of the 492.2 nm / 504.8 nm intensity ratio as shown in Fig. 4.4(c). For example, $\pm 5 \text{ eV}$ uncertainty of T_e corre-

sponds a variation of the line intensity ratio smaller than $\pm 10 \%$.

The experimental errors of T_e and n_e measurements depend on the plasma parameters and employed line pairs. Cross check using several line pairs will improve the reliability of the measurements. Empirically, T_e and n_e errors in this technique are considered within 50 % and a factor of two for the plasma with $T_e = 5 - 50 \text{ eV}$ and $n_e < 10^{13} \text{ cm}^{-3}$, respectively.

C. Conclusion

Helium I line intensity ratios have been obtained with the revised C.R. model, and summarized as a database for the T_e and n_e measurements. Although this technique has several limitations for experimental applications, depending on atomic and molecular species in the plasma, energy distributions of the plasma electrons and the other various particles, pressure of helium gas, and the dimensions and configurations of the device, it is still attractive for the investigations or indications of hot electrons, resonance scattering, and change in T_e and n_e . The reliability of the line intensity ratios will be improved by including various experimental conditions in the C.R. model.

X. APPENDIX

The line intensity ratios for the experimental use are summarized as contour plots and n_e and T_e dependences in Figs. A1-A9. Rate coefficients for excitation and ionization C_{ij} and S_i from the ground state and the two metastable states $2^1,3S$ included in this work are shown in Figs. B1 - B4 [15-18].

ACKNOWLEDGMENTS

The authors are grateful to Prof. T. Fujimoto for the valuable discussions and for the original numerical code of the collisional radiative model.

-
- [1] S. P. Cunningham, *Conference on Thermonuclear Reactors*, Livermore, U.S. Atomic Energy Commission Report, No. 279, p.289 (1955).
- [2] A. H. Gabriel, and D. W. O. Heddle, Proc. Roy. Soc. (London) **A258**, 124 (1960).
- [3] C. C. Lin, and R. M. St. John, Phys. Rev. **128**, 1749 (1962).
- [4] R. J. Sovie, Phys. Fluids **7**, 613 (1964).
- [5] R. F de Vries, and R. Mewe, Phys. Fluids **9**, 414 (1966).
- [6] B. J. Eastlund, D. Spero, M. Johnson, P. Korn, C. B. Wharton, and E. R. Wilson, J. Appl. Phys. **44**, 4930 (1973).
- [7] A. Pospieszczyk, F. Aumayr, H. L. Bay, E. Hintz P. Leisemann, Y. T. Lie, G. G. Ross, D. Rusbült, R. P. Schorn, B. Schweer, and H. Winter, J. Nucl. Mater. **162-164**, 574 (1989).
- [8] T. Fujimoto, J. Quant. Spectrosc. Radiat. Transfer **21**, 439 (1979).
- [9] B. Schweer, G. Mank, A. Pospieszczyk, B. Brosda, B. Pohlmeier, J. Nucl. Mater. **196-198**, 174 (1992).
- [10] H. Behrendt, W. Bohmeyer, L. Dietrich, G. Fussmann, H. Greuner, H. Grote, M. Kammeyer, P. Kornejew, M. Laux, E. Pasch, *21st EPS Conference on Controlled Fusion and Plasma Physics*, Montpellier, France, III p.1328 (1994).
- [11] S. Sasaki, S. Takamura, T. Kato, J. Fusion Energy and Design, **34-35**, 747 (1997).
- [12] S. Sasaki, S. Takamura, S. Watanabe, S. Masuzaki, T. Kato, and K. Kadota, Rev. Sci. Instrum. **67**, 3521 (1996).
- [13] S. Masuzaki, and S. Takamura, Jpn. J. Appl. Phys. **29**, 2835 (1990).
- [14] D. E. Post, A review of recent development in atomic processes for divertor and edge plasmas, J. Nucl. Mater. **220-222** (1995) 143-157.
- [15] F. J. de Heer, R. Hoekstra, A. E. Kingston, and H. P. Summers, Nucl. Fusion Suppl. **3**, 19 (1992).
- [16] T. Kato, and R. K. Janev, Nucl. Fusion Suppl. **3**, 33 (1992).
- [17] F. J. de Heer, H. O. Folkerts, F. W. Bliek, R. Hoekstra, T. Kato, A. E. Kingston, K. A. Berrington, H. P. Summers, Nucl. Fusion Suppl. **6**, 7 (1995).
- [18] M. Goto, and T. Fujimoto, Research Report, **NIFS-DATA-43**, National Institute for Fusion Science, Nagoya, Japan (1997).
- [19] V. P. Shevelko, and H. Tawara, Nucl. Fusion Suppl. **6**, 27 (1995).
- [20] S. Takamura, A. Sato, Y. Shen, and T. Okuda, J. Nucl. Mater. **149**, 212 (1987).
- [21] K. Shiraishi, and S. Takamura, J. Nucl. Mater. **176-177**, 251 (1990).
- [22] T. Holstein, Phys. Rev. **72**, 1212 (1947).
- [23] H. W. Drawin, and F. Emard, Beitr. Plasmaphysik **30a**, 143 (1973).
- [24] B. Dubreuil, and A. Catherinot, Physica **93C**, 408 (1978).
- [25] National Standard Reference Data Series 3, National Bureau of Standard, (1970) Section 3, A6I-1.
- [26] S. Sasaki, S. Takamura, Y. Uesugi, Y. Ohkouchi, and K. Kadota, Rev. Sci. Instrum. **64**, 2277 (1993).
- [27] C. D. Lin, W. R. Johnson, and A. Dalgarno, Phys. Rev. A, **15**, 154 (1977).
- [28] N. Brenning, J. Quant. Spectrosc. Radiat. Transfer **24**, 319 (1980).
- [29] R. A. Hulse, D. E. Post, D. R. Mikkelsen, J. Phys. B: Molec. Phys., **13**, 3895 (1980).
- [30] N. Shimakura, M. Kimura, N. F. Lane, Phys. Rev. A, **47**, 709 (1993).

Tables

TABLE I. Energy level $E(i)$ of helium atom with principal quantum number $n \leq 7$ [25].

Term	$E(i)$ [eV]						
1^1S	0	2^1P	21.218	3^1D	23.074		
2^1S	20.616	3^1P	23.087	4^1D	23.736	4^1F	23.737
3^1S	22.920	4^1P	23.742	5^1D	24.042	5^1F	24.043
4^1S	23.673	5^1P	24.045	6^1D	24.209	6^1F	24.209
5^1S	24.011	6^1P	24.211	7^1D	24.309	7^1F	24.309
6^1S	24.191	7^1P	24.310				
7^1S	24.298						
2^3S	19.819	2^3P	20.964	3^3D	23.073		
3^3S	22.718	3^3P	23.007	4^3D	23.736	4^3F	23.737
4^3S	23.594	4^3P	23.708	5^3D	24.042	5^3F	24.043
5^3S	23.972	5^3P	24.028	6^3D	24.209	6^3F	24.209
6^3S	24.169	6^3P	24.200	7^3D	24.309	7^3F	24.309
7^3S	24.284	7^3P	24.304				

TABLE II. Energy level $E(i)$ of helium atom with principal quantum number $n = 8 - 20$ employed in this work.

n	$E(i)$ [eV]						
8	24.374	12	24.492	16	24.533	20	24.552
9	24.418	13	24.506	17	24.539		
10	24.450	14	24.517	18	24.544		
11	24.474	15	24.526	19	24.549		

TABLE III. Wavelength λ [nm] and transition probability A_{ij} [1/s] of helium atom for $i \rightarrow j$ transition helium atom [25].

Transition $i \rightarrow j$	Wavelength λ [nm]	Transition probability A_{ij} [10^8 1/s]	Transition $i \rightarrow j$	Wavelength λ [nm]	Transition probability A_{ij} [10^8 1/s]
$2^1P \rightarrow 1^1S$	58.4	17.99			
$3^1P \rightarrow 1^1S$	53.7	5.66			
$4^1P \rightarrow 1^1S$	52.2	2.46			
$5^1P \rightarrow 1^1S$	51.6	1.28			
$2^1P \rightarrow 2^1S$	2058.1	0.01976	$2^3P \rightarrow 2^3S$	1083.0	0.1022
$3^1P \rightarrow 2^1S$	501.6	0.1338	$3^3P \rightarrow 2^3S$	388.9	0.09478
$4^1P \rightarrow 2^1S$	396.5	0.0717	$4^3P \rightarrow 2^3S$	318.8	0.0505
$5^1P \rightarrow 2^1S$	361.4	0.0376	$5^3P \rightarrow 2^3S$	294.5	0.0293
$3^1S \rightarrow 2^1P$	728.1	0.181	$3^3S \rightarrow 2^3P$	706.5	0.278
$4^1S \rightarrow 2^1P$	504.8	0.0655	$4^3S \rightarrow 2^3P$	471.3	0.106
$5^1S \rightarrow 2^1P$	443.8	0.0313	$5^3S \rightarrow 2^3P$	412.1	0.0430
$3^1D \rightarrow 2^1P$	667.8	0.638	$3^3D \rightarrow 2^3P$	587.6	0.706
$4^1D \rightarrow 2^1P$	492.2	0.202	$4^3D \rightarrow 2^3P$	447.2	0.251
$5^1D \rightarrow 2^1P$	438.8	0.0907	$5^3D \rightarrow 2^3P$	402.6	0.117

Figure Captions

Fig. 1 Energy level $E(i)$ of helium atom.

Fig. 2.1 Normalized population densities, $n(i)/n_{He}$, for 2^1S and 2^3S , and the sums of $n(i)/n_{He}$ for singlet (s) and triplet (t) are shown as (a) T_e dependence at $n_e = 10^{12} \text{ cm}^{-3}$, and (b) n_e dependence at $T_e = 20 \text{ eV}$.

Fig. 2.2 Percentage contributions of (a) in-flows and (b) out-flows of electrons involving 2^1S at $T_e = 20 \text{ eV}$.

Fig. 2.3 Percentage contributions of (a) in-flows and (b) out-flows of electrons involving 2^3S at $T_e = 20 \text{ eV}$.

Fig. 2.4 Normalized population densities, $n(i)/n_{He}$, for 2^1P , 3^1P , 3^1S , and 4^1D are shown in (a) T_e dependence at $n_e = 10^{12} \text{ cm}^{-3}$, and (b) n_e dependence at $T_e = 20 \text{ eV}$.

Fig. 2.5 Normalized population densities, $n(i)/n_{He}$, for 2^3P , 3^3P , and 3^3S are shown in (a) T_e dependence at $n_e = 10^{12} \text{ cm}^{-3}$, and (b) n_e dependence at $T_e = 20 \text{ eV}$.

Fig. 2.6 Percentage contributions of (a) in-flows and (b) out flows of electrons involving 4^1D at $T_e = 20 \text{ eV}$.

Fig. 3.1 Effective emission rate coefficients $C_{em}^{eff}(\lambda)$ for the resonance lines ($1^1S - n^1P$) are shown in (a) T_e dependence at $n_e = 10^{12} \text{ cm}^{-3}$, and (b) n_e dependence at $T_e = 20 \text{ eV}$.

Fig. 3.2 Effective emission rate coefficients $C_{em}^{eff}(\lambda)$ for the singlet S lines ($2^1P - n^1S$) are shown in (a) T_e dependence at $n_e = 10^{12} \text{ cm}^{-3}$, and (b) n_e dependence at $T_e = 20 \text{ eV}$.

Fig. 3.3 Effective emission rate coefficients $C_{em}^{eff}(\lambda)$ for the singlet P ($2^1S - n^1P$) lines are shown in (a) T_e dependence at $n_e = 10^{12} \text{ cm}^{-3}$, and (b) n_e dependence at $T_e = 20 \text{ eV}$.

Fig. 3.4 Effective emission rate coefficients $C_{em}^{eff}(\lambda)$ for the singlet D ($2^1P - n^1D$) lines are shown in (a) T_e dependence at $n_e = 10^{12} \text{ cm}^{-3}$, and (b) n_e dependence at $T_e = 20 \text{ eV}$.

Fig. 3.5 Effective emission rate coefficients $C_{em}^{eff}(\lambda)$ for the triplet S lines ($2^3P - n^3S$) are shown in (a) T_e dependence at $n_e = 10^{12} \text{ cm}^{-3}$, and (b) n_e dependence at $T_e = 20 \text{ eV}$.

Fig. 3.6 Effective emission rate coefficients $C_{em}^{eff}(\lambda)$ for the triplet P lines ($2^3S - n^3P$) are shown in (a) T_e dependence at $n_e = 10^{12} \text{ cm}^{-3}$, and (b) n_e dependence at $T_e = 20 \text{ eV}$.

Fig. 3.7 Effective emission rate coefficients $C_{em}^{eff}(\lambda)$ for the triplet D lines ($2^3P - n^3D$) are shown in (a) T_e dependence at $n_e = 10^{12} \text{ cm}^{-3}$, and (b) n_e dependence at $T_e = 20 \text{ eV}$.

Fig. 4.1 Line intensity ratios for singlet - triplet line pairs with $\lambda \approx 500 \text{ nm}$ for T_e measurement are shown in (a) T_e dependence at $n_e = 10^{12} \text{ cm}^{-3}$, and (b) n_e dependence at $T_e = 20 \text{ eV}$.

Fig. 4.2 The T_e dependence of the singlet - triplet line intensity ratios with $\lambda \approx 500 \text{ nm}$, (a) 504.8 nm / 471.3 nm, (b) 501.6 nm / 471.3 nm, (c) 492.2 nm / 471.3 nm.

Fig. 4.3 Line intensity ratios for singlet - singlet line pairs with $\lambda \approx 500 \text{ nm}$ for n_e measurement are shown in (a) T_e dependence at $n_e = 10^{12} \text{ cm}^{-3}$, and (b) n_e dependence at $T_e = 20 \text{ eV}$.

Fig. 4.4 The n_e dependence of singlet - singlet line intensity ratios with $\lambda \approx 500 \text{ nm}$, (a) 501.6 nm / 504.8 nm, (b) 501.6 nm / 492.2 nm, (c) 492.2 nm / 504.8 nm.

Fig. 4.5 Line intensity ratios for the line pairs with $\lambda \approx 700 \text{ nm}$ are shown in (a) T_e dependence at $n_e = 10^{12} \text{ cm}^{-3}$, and (b) n_e dependence at $T_e = 20 \text{ eV}$.

Fig. 4.6 Line intensity ratios with $\lambda \approx 700 \text{ nm}$ for experimental applications; (a) T_e dependence of 728.1 nm / 706.5 nm at $n_e = 10^{12} \text{ cm}^{-3}$, (b) T_e dependence of 667.8 nm / 706.5 nm at $n_e = 10^{12} \text{ cm}^{-3}$, (c) n_e dependence of 667.8 nm / 728.1 nm at $T_e = 20 \text{ eV}$.

Fig. 5.1 Effective ionization rate coefficient S^{eff} are shown in (a) T_e dependence at $n_e = 10^{12} \text{ cm}^{-3}$, and (b) n_e dependence at $T_e = 20 \text{ eV}$.

Fig. 5.2 $S^{eff}/C_{em}^{eff}(\lambda)$ for singlet S lines are shown in (a) T_e dependence at $n_e = 10^{12} \text{ cm}^{-3}$, and (b) n_e dependence at $T_e = 20 \text{ eV}$.

Fig. 5.3 $S^{eff}/C_{em}^{eff}(\lambda)$ for singlet P lines are shown in (a) T_e dependence at $n_e = 10^{12} \text{ cm}^{-3}$, and (b) n_e dependence at $T_e = 20 \text{ eV}$.

Fig. 5.4 $S^{eff}/C_{em}^{eff}(\lambda)$ for singlet D lines are shown in (a) T_e dependence at $n_e = 10^{12} \text{ cm}^{-3}$, and (b) n_e dependence at $T_e = 20 \text{ eV}$.

Fig. 5.5 $S^{eff}/C_{em}^{eff}(\lambda)$ for triplet S lines are shown in (a) T_e dependence at $n_e = 10^{12} \text{ cm}^{-3}$, and (b) n_e dependence at $T_e = 20 \text{ eV}$.

Fig. 5.6 $S^{eff}/C_{em}^{eff}(\lambda)$ for triplet P lines are shown in (a) T_e dependence at $n_e = 10^{12} \text{ cm}^{-3}$, and (b) n_e dependence at $T_e = 20 \text{ eV}$.

Fig. 5.7 $S^{eff}/C_{em}^{eff}(\lambda)$ for triplet D lines are shown in (a) T_e dependence at $n_e = 10^{12} \text{ cm}^{-3}$, and (b) n_e dependence at $T_e = 20 \text{ eV}$.

Fig. 6.1 Effective emission rate coefficient $C_{em}^{eff}(\lambda)$ for (a) 54.8 nm and (b) 667.8 nm in the presence of hot electrons with $T_{eh} = 20 \text{ eV}$ and 40 eV , $\alpha = 10\%$ at $n_e = 10^{12} \text{ cm}^{-3}$.

Fig. 6.2 Line intensity ratios in the presence of hot electrons, (a) 504.8 nm / 471.3 nm, (b) 492.2 nm / 471.3 nm, (c) 728.1 nm / 706.5 nm, (d) 667.8 nm / 706.5 nm.

Fig. 6.3 Effective ionization rate coefficient S^{eff} in the presence of hot electrons.

Fig. 7.1 Optical depth $\tau(\lambda)$ and optical escape factor $\Lambda(\lambda)$ for 58.2 nm ($1^1S - 2^1P$), 53.7 nm ($1^1S - 3^1P$), and 52.2 nm ($1^1S - 4^1P$) lines.

Fig. 7.2 Normalized population densities $n(i)/n_{He}$ as a function of helium column density $n_{He} \times L$ at $n_e = 10^{12} \text{ cm}^{-3}$ and $T_e = 20 \text{ eV}$.

Fig. 7.3 Effective emission rate coefficients $C_{em}^{eff}(\lambda)$ as functions of helium column density $n_{He} \times L$ at $n_e = 10^{12} \text{ cm}^{-3}$ and $T_e = 20 \text{ eV}$; (a) $1^1S - n^1P$, (b) $2^1P - n^1S$, (c) $2^1S - n^1P$, (d) $2^1P - n^1D$.

Fig. 7.4 Line intensity ratios $C_{em}^{eff}(\lambda_1)/C_{em}^{eff}(\lambda_2)$ as functions of helium column density $n_{He} \times L$. (a) Singlet - triplet pairs with $\lambda \approx 500 \text{ nm}$. (b) Singlet - triplet pairs with $\lambda \approx 500 \text{ nm}$. (c) Line intensity ratios with $\lambda \approx 700 \text{ nm}$.

Fig. 7.5 Effective ionization rate coefficient S^{eff} as a function of helium column density $n_{He} \times L$.

Fig. 8.1 Line intensity ratios in this work are compared to the results by Schweer and Behrendt; (a) 667.8 nm / 728.1 nm, (b) 501.6 nm / 504.8 nm, (c) 728.1 nm / 706.5 nm.

Fig. 8.2 Contribution of the recombining component on the population density, $n(i)_{rec} / n(i)$ at ion / atom density ratio $n_{He}^+ / n_{He} = 0.1$; (a) $n(4^1D)_{rec}/n(4^1D)$, (b) $n(4^3S)_{rec}/n(4^3S)$.

Fig. 8.3 Modification of the line intensity ratios for singlet - triplet pair, 492.2 nm / 471.3 nm, 501.6 nm / 471.3 nm, 504.8 nm / 471.3 nm due to the recombining components of the excited state at ion / atom density ratio $n_{He}^+ / n_{He} = 0.1$ and $n_e = 10^{12} \text{ cm}^{-3}$.

Appendix

Fig. A1 The 504.8 nm / 471.3 nm line intensity ratio is shown as (a) contour plot, (b) T_e dependence at $n_e = 10^{12} \text{ cm}^{-3}$, and (c) n_e dependence at $T_e = 20 \text{ eV}$.

Fig. A2 The 501.6 nm / 471.3 nm line intensity ratio is shown as (a) contour plot, (b) T_e dependence at $n_e = 10^{12} \text{ cm}^{-3}$, and (c) n_e dependence at $T_e = 20 \text{ eV}$.

Fig. A3 The 492.2 nm / 471.3 nm line intensity ratio is shown as (a) contour plot, (b) T_e dependence at $n_e = 10^{12} \text{ cm}^{-3}$, and (c) n_e dependence at $T_e = 20 \text{ eV}$.

Fig. A4 The 501.6 nm / 504.8 nm line intensity ratio is shown as (a) contour plot, (b) T_e dependence at $n_e = 10^{12} \text{ cm}^{-3}$, and (c) n_e dependence at $T_e = 20 \text{ eV}$.

Fig. A5 The 501.6 nm / 492.2 nm line intensity ratio is shown as (a) contour plot, (b) T_e dependence at $n_e = 10^{12} \text{ cm}^{-3}$, and (c) n_e dependence at $T_e = 20 \text{ eV}$.

Fig. A6 The 492.2 nm / 504.8 nm line intensity ratio is shown as (a) contour plot, (b) T_e dependence at $n_e = 10^{12} \text{ cm}^{-3}$, and (c) n_e dependence at $T_e = 20 \text{ eV}$.

Fig. A7 The 728.1 nm / 706.5 nm line intensity ratio is shown as (a) contour plot, (b) T_e dependence at $n_e = 10^{12} \text{ cm}^{-3}$, and (c) n_e dependence at $T_e = 20 \text{ eV}$.

Fig. A8 The 667.8 nm / 706.5 nm line intensity ratio is shown as (a) contour plot, (b) T_e dependence at $n_e = 10^{12} \text{ cm}^{-3}$, and (c) n_e dependence at $T_e = 20 \text{ eV}$.

Fig. A9 The 728.1 nm / 667.8 nm line intensity ratio is shown as (a) contour plot, (b) T_e dependence at $n_e = 10^{12} \text{ cm}^{-3}$, and (c) n_e dependence at $T_e = 20 \text{ eV}$.

Fig. B1 Excitation rate coefficients from the ground state 1^1S ; (a) $1^1S - n^1S$, (b) $1^1S - n^1P$, (c) $1^1S - n^1D$, (d) $1^1S - n^3S$, (e) $1^1S - n^3P$, (f) $1^1S - n^3D$.

Fig. B2 Excitation rate coefficients from the metastable state 2^1S ; (a) $2^1S - n^1S$, (b) $2^1S - n^1P$, (c) $2^1S - n^1D$, (d) $2^1S - n^3S$, (e) $2^1S - n^3P$, (f) $2^1S - n^3D$.

Fig. B3 Excitation rate coefficients from the metastable state 2^3S ; (a) $2^3S - n^1S$, (b) $2^3S - n^1P$, (c) $2^3S - n^1D$, (d) $2^3S - n^3S$, (e) $2^3S - n^3P$, (f) $2^3S - n^3D$.

Fig. B4 Ionization rate coefficients from the ground state 1^1S and the metastable states 2^1S and 2^3S .

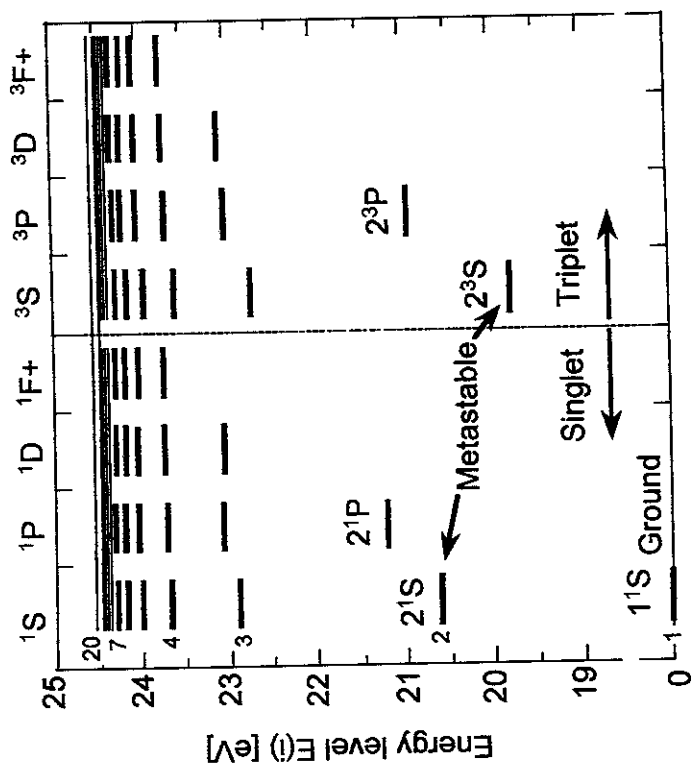


Fig. 1

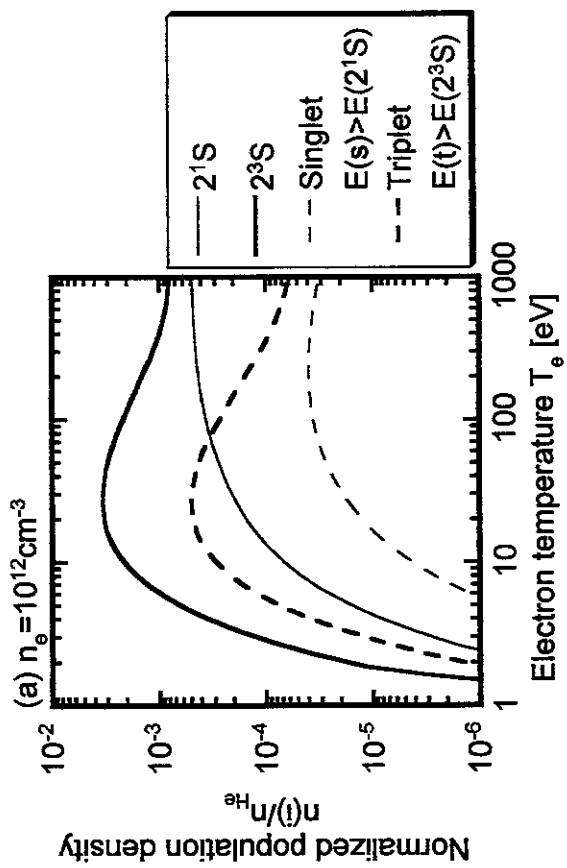


Fig. 2.1(a)

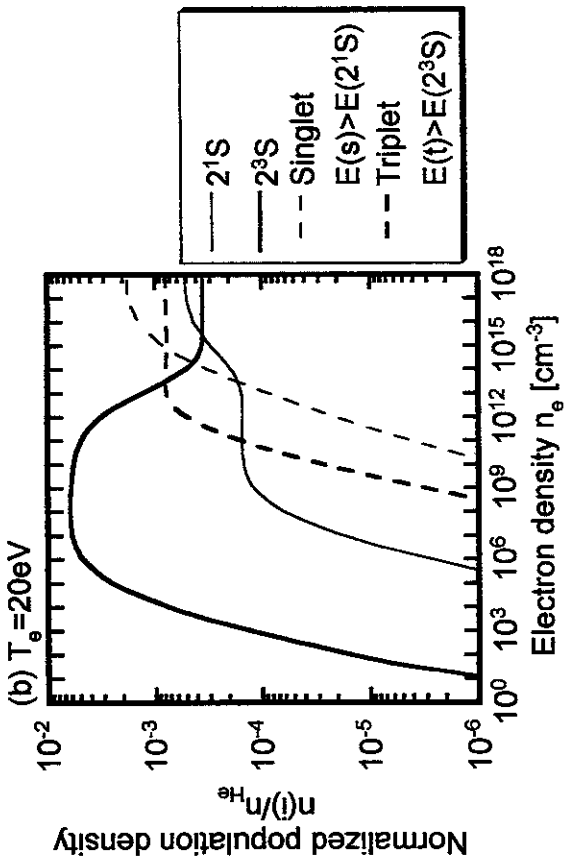


Fig. 2.1(b)

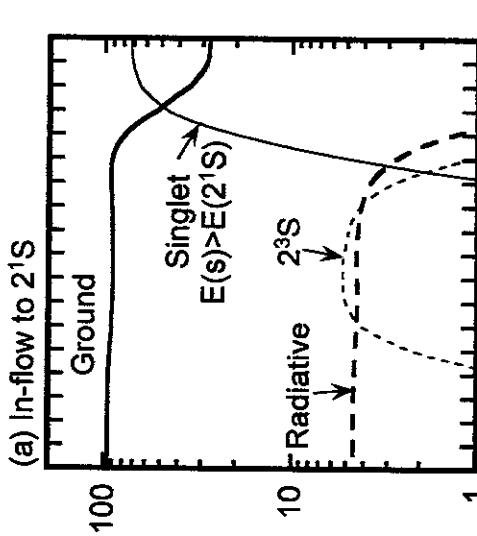


Fig. 2.2(a)

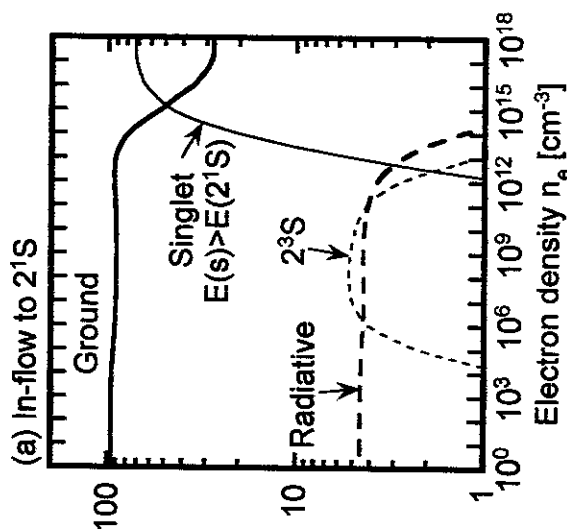


Fig. 2.2(b)

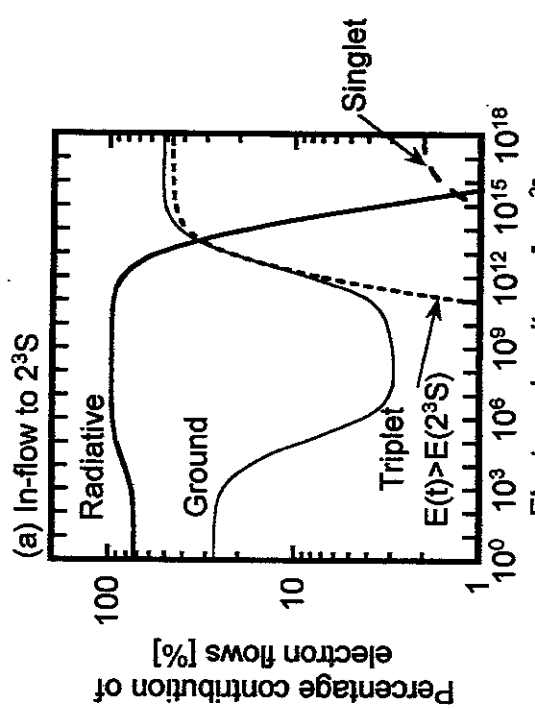


Fig. 2.3(a)

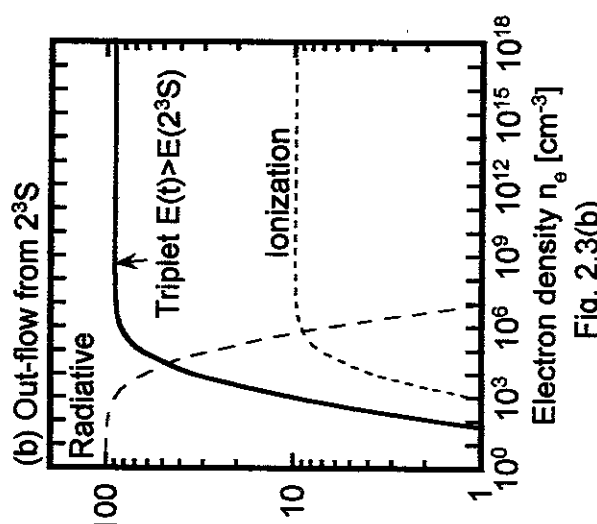


Fig. 2.3(b)

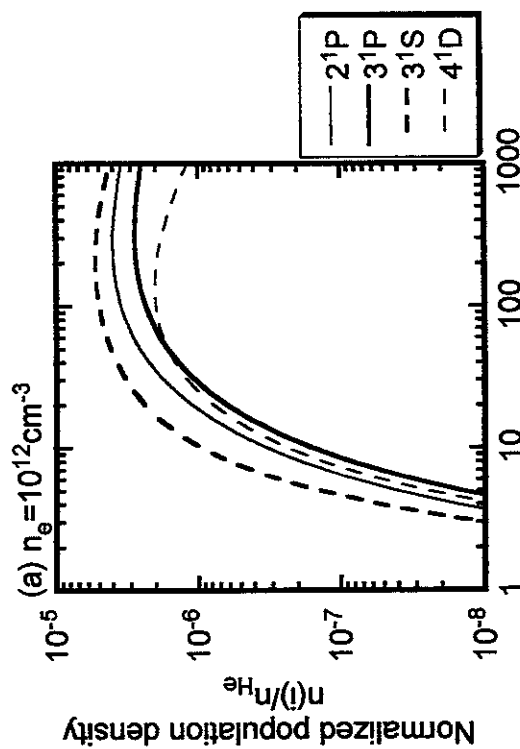


Fig. 2.4(a)

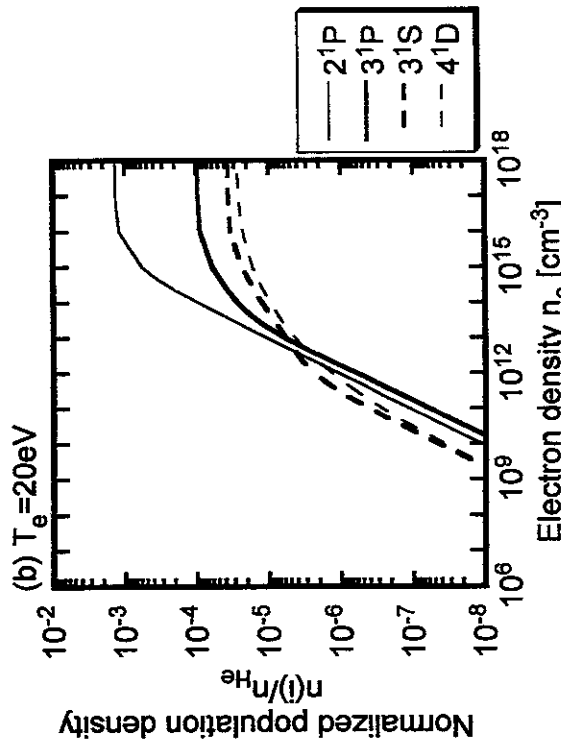


Fig. 2.4(b)

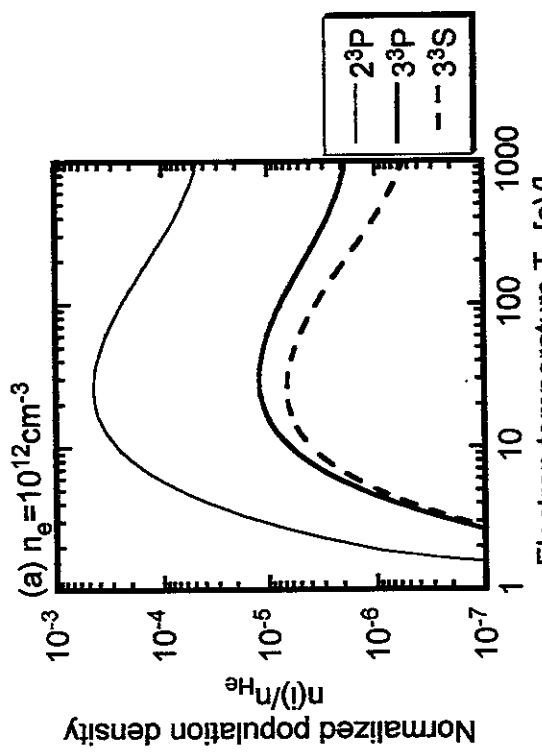


Fig. 2.5(a)

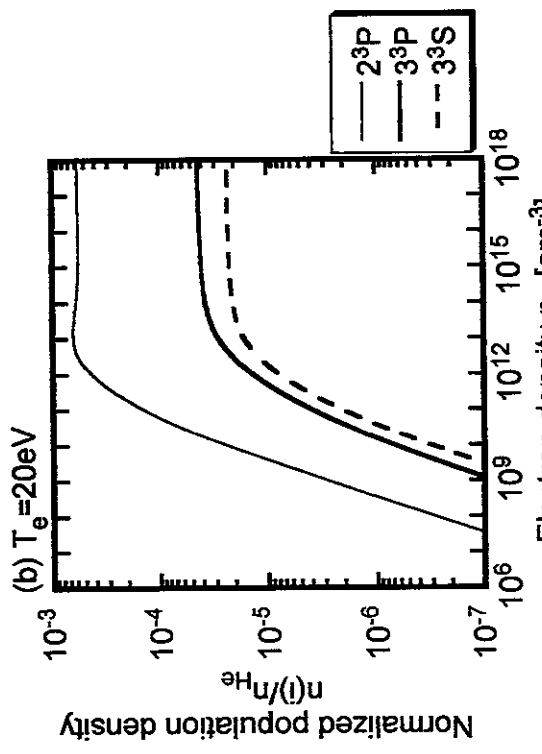


Fig. 2.5(b)

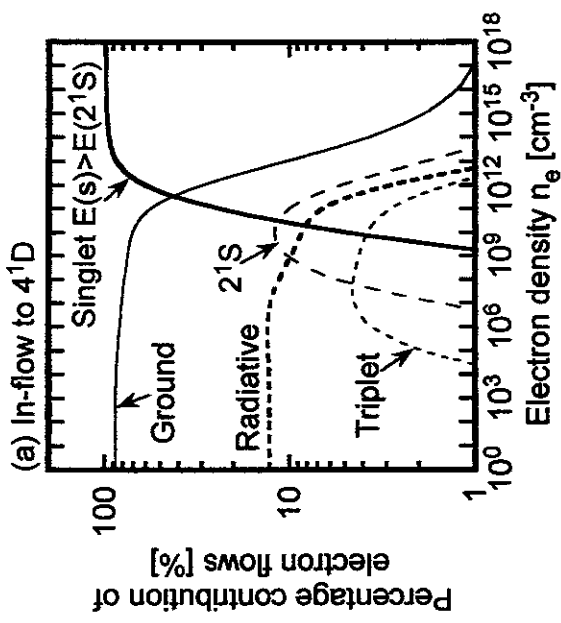


Fig. 2.6(a)

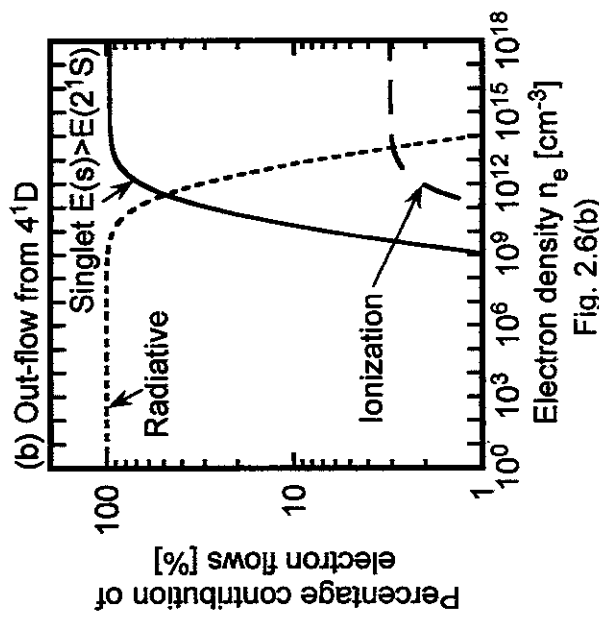


Fig. 2.6(b)

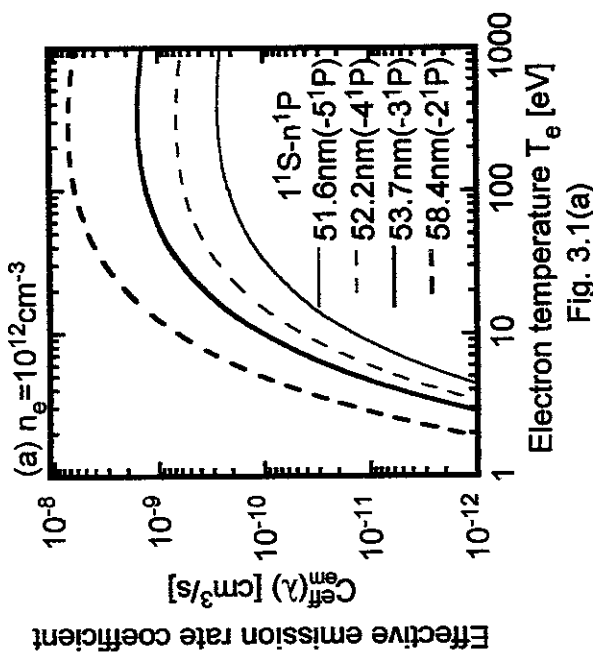


Fig. 3.1(a)

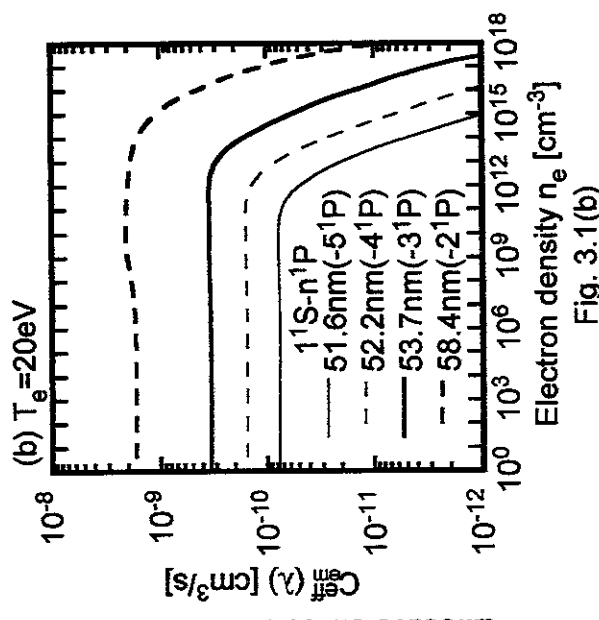


Fig. 3.1(b)

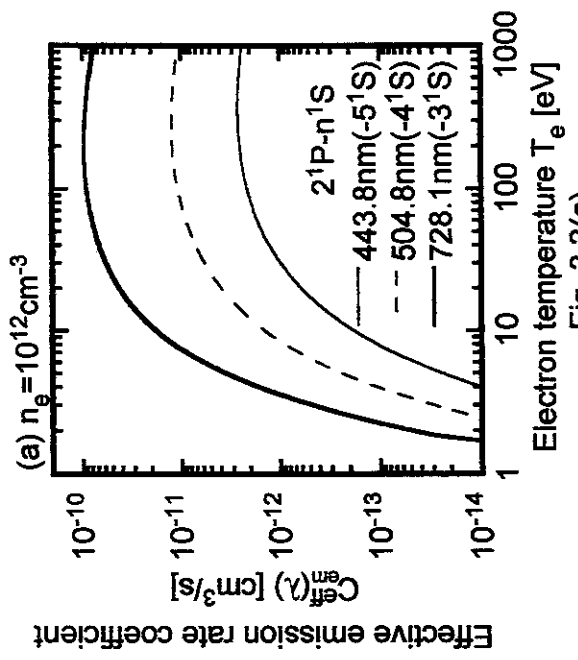


Fig. 3.2(a)

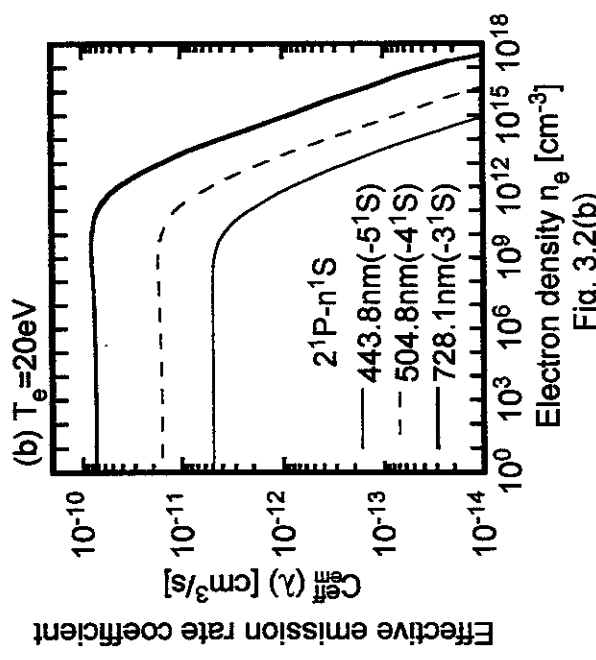


Fig. 3.2(b)

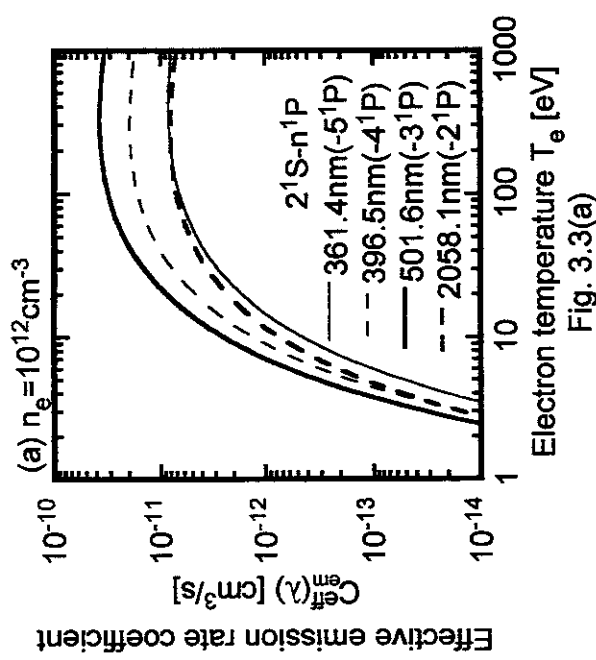


Fig. 3.3(a)

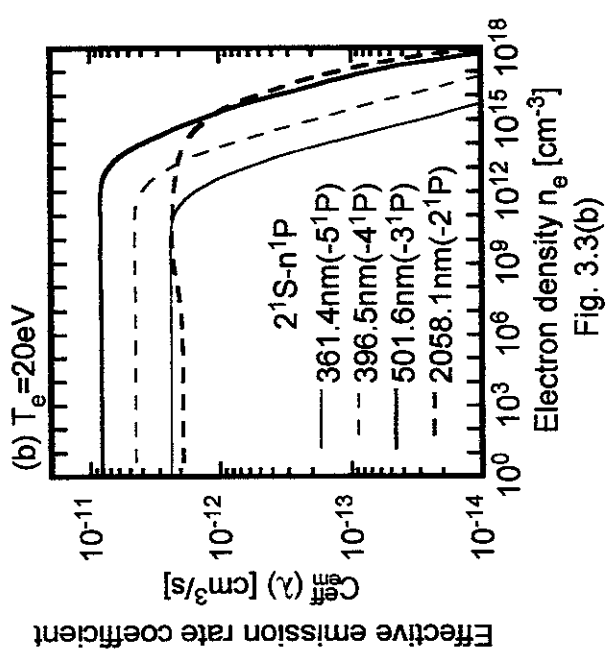


Fig. 3.3(b)

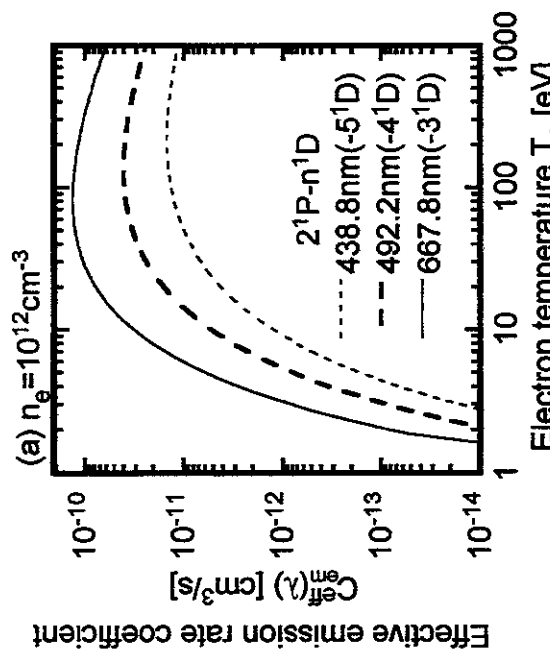


Fig. 3.4(a)

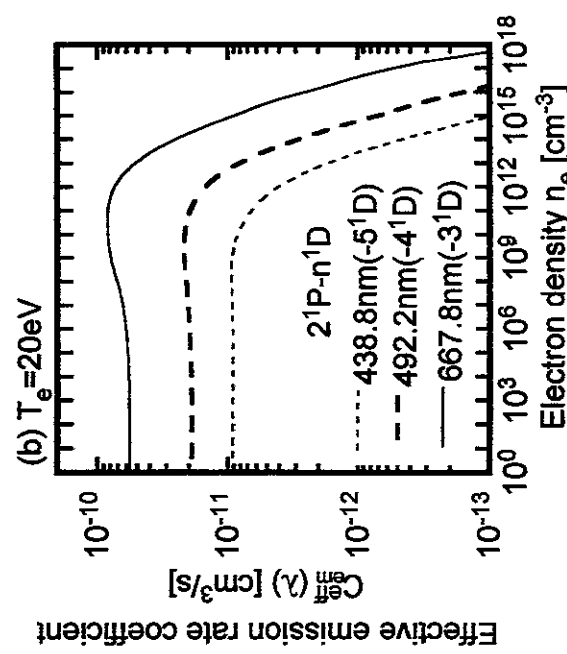


Fig. 3.4(b)

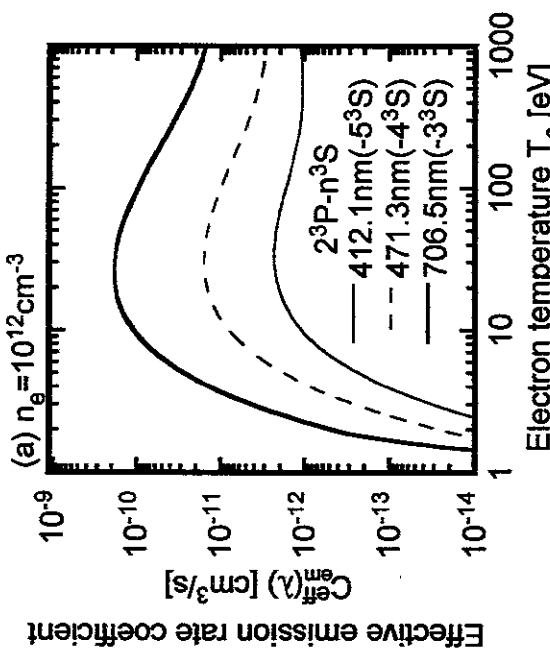


Fig. 3.5(a)

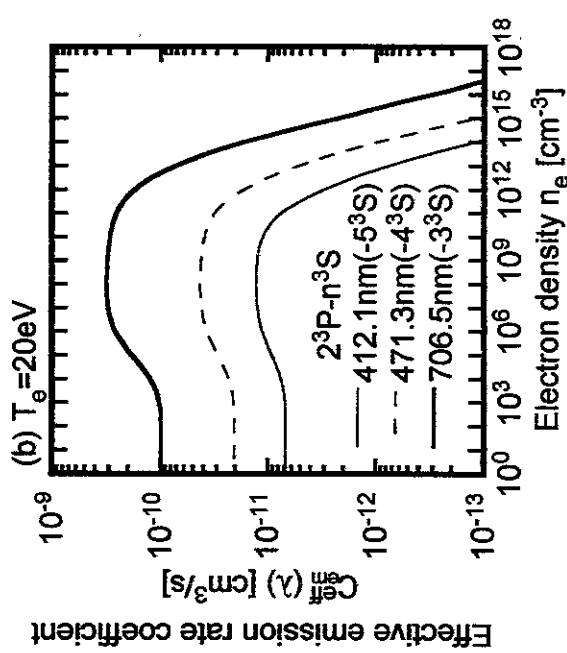


Fig. 3.5(b)

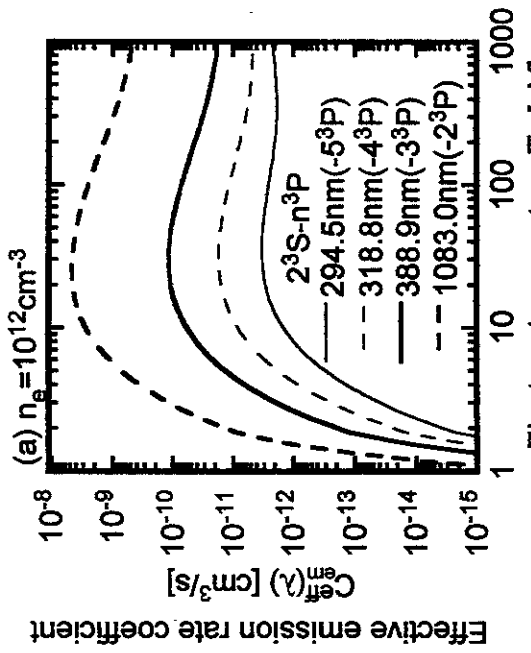


Fig. 3.6(a)

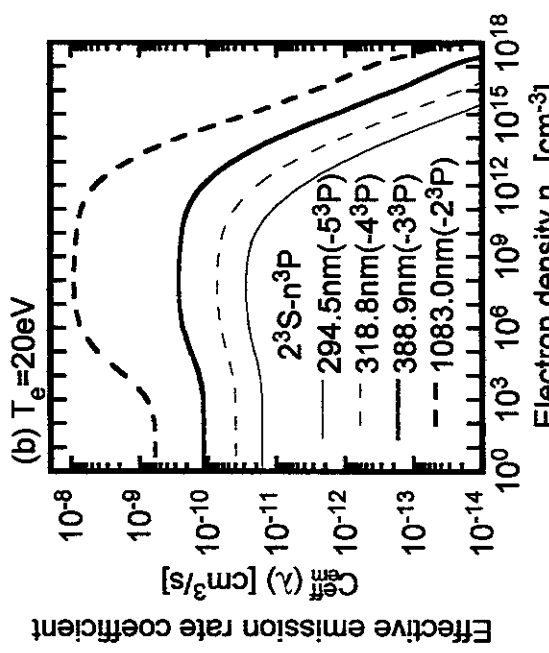


Fig. 3.6(b)

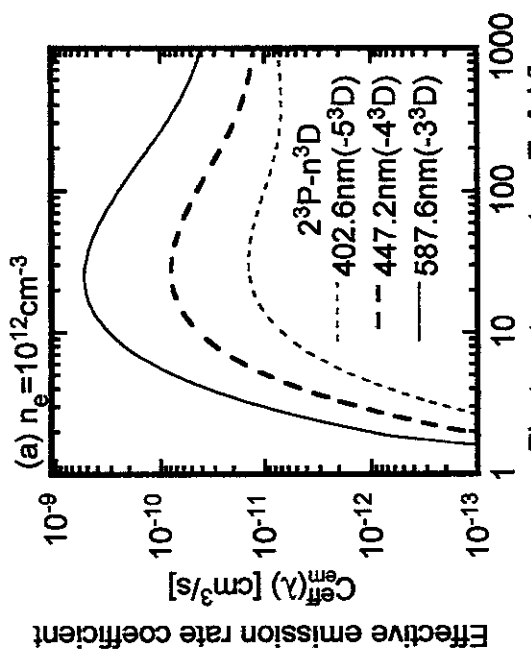


Fig. 3.7(a)

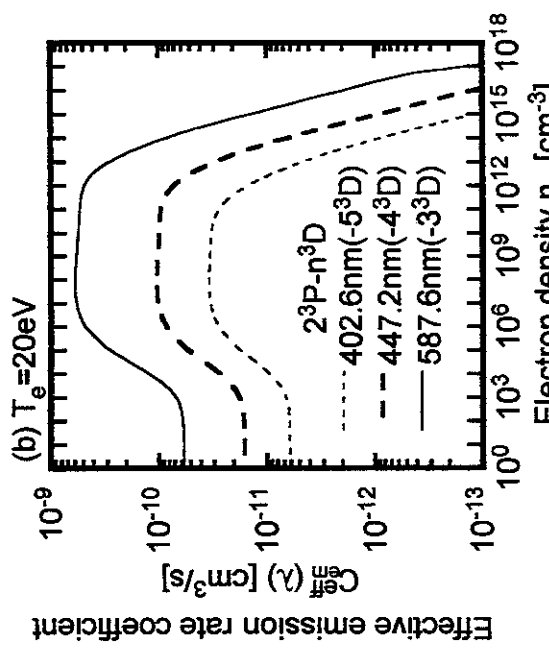


Fig. 3.7(b)

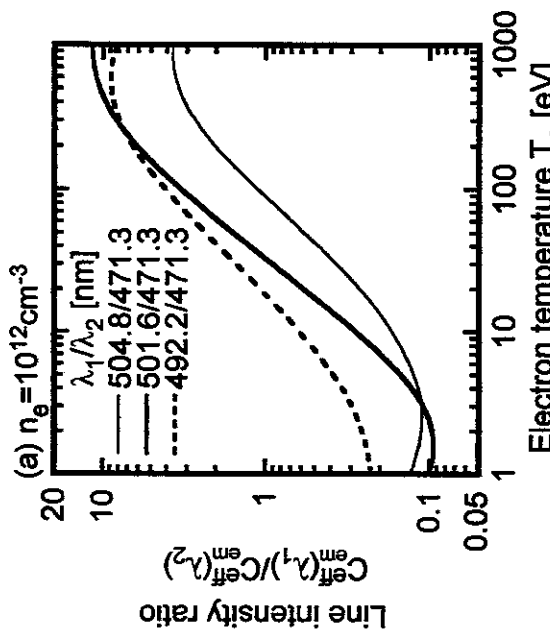


Fig. 4.1(a)

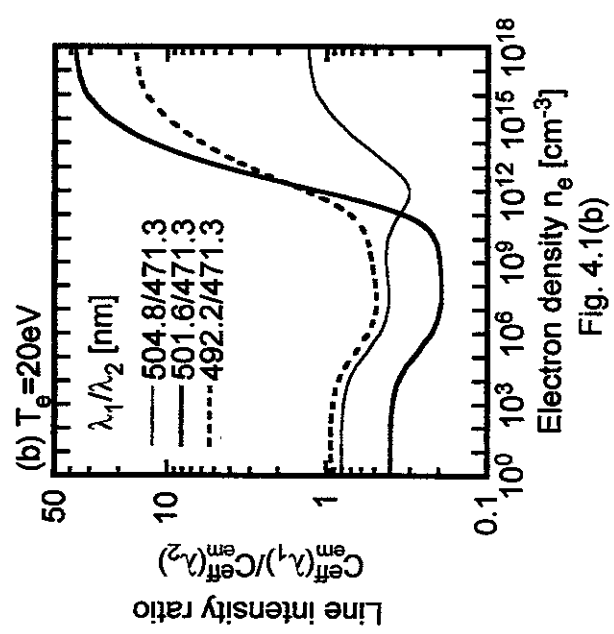


Fig. 4.1(b)

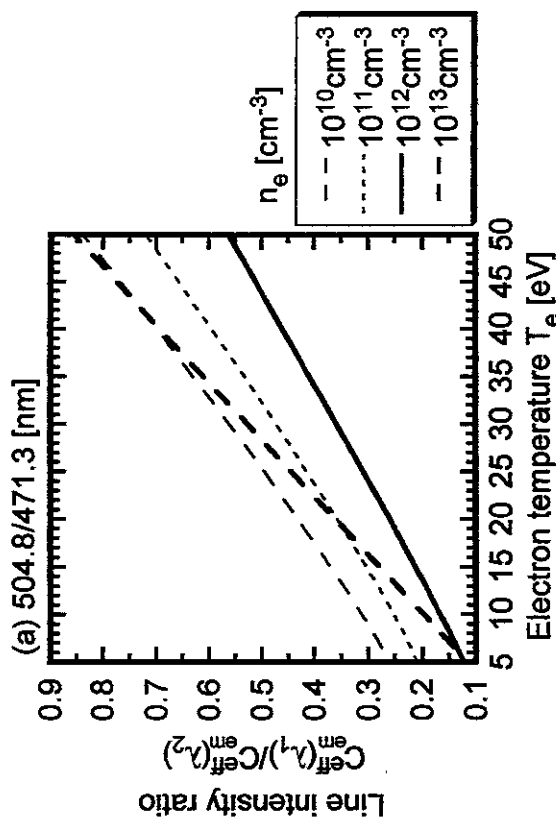


Fig. 4.2(a)

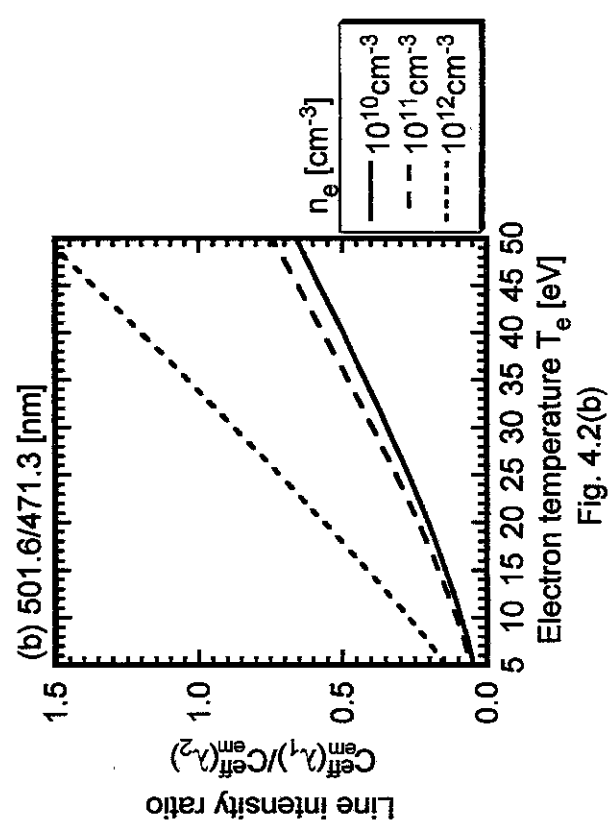


Fig. 4.2(b)

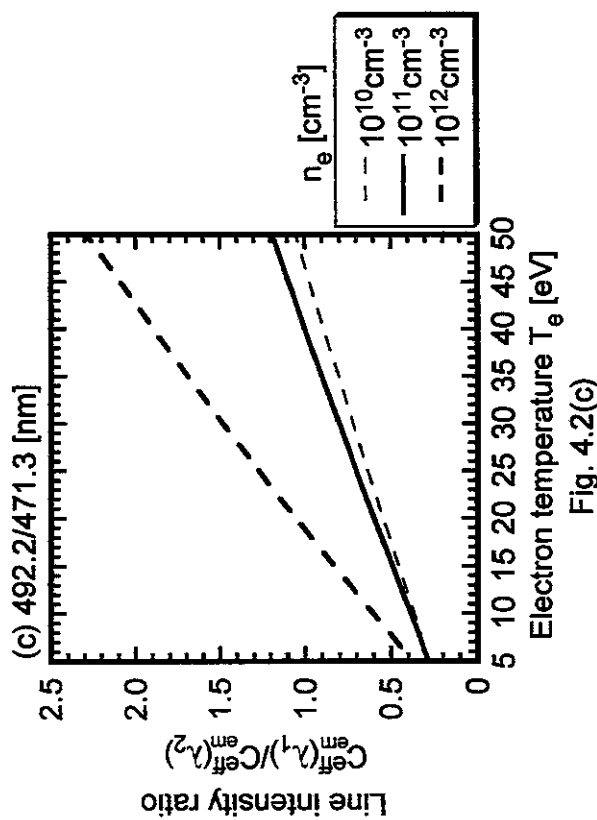


Fig. 4.2(c)

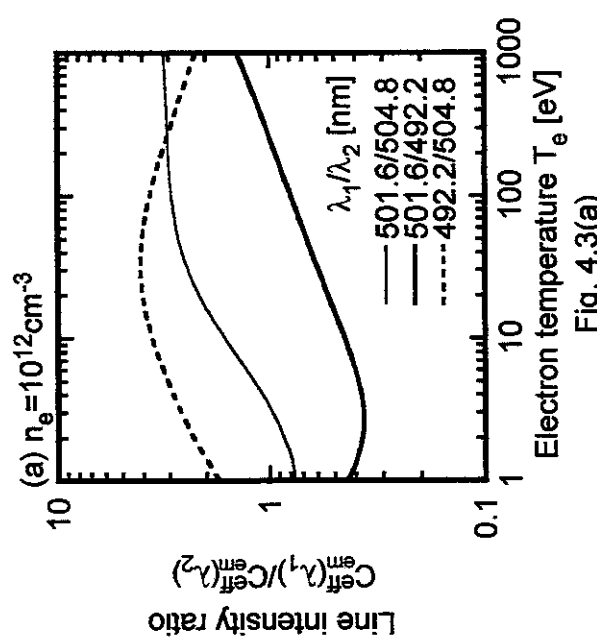


Fig. 4.3(a)

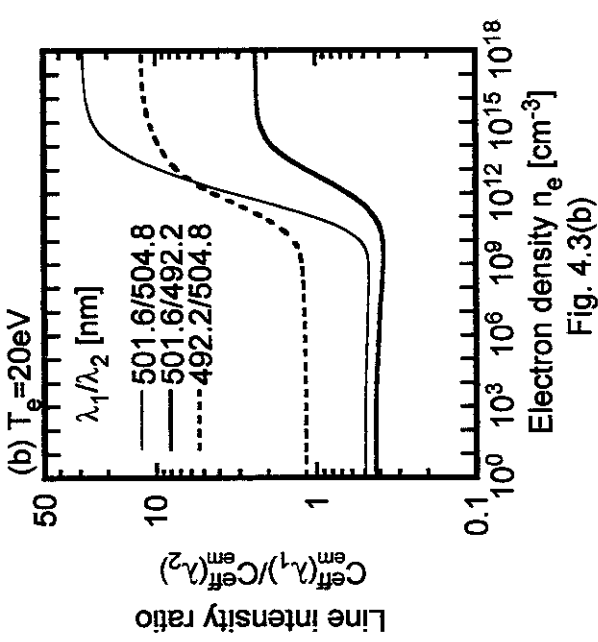


Fig. 4.3(b)

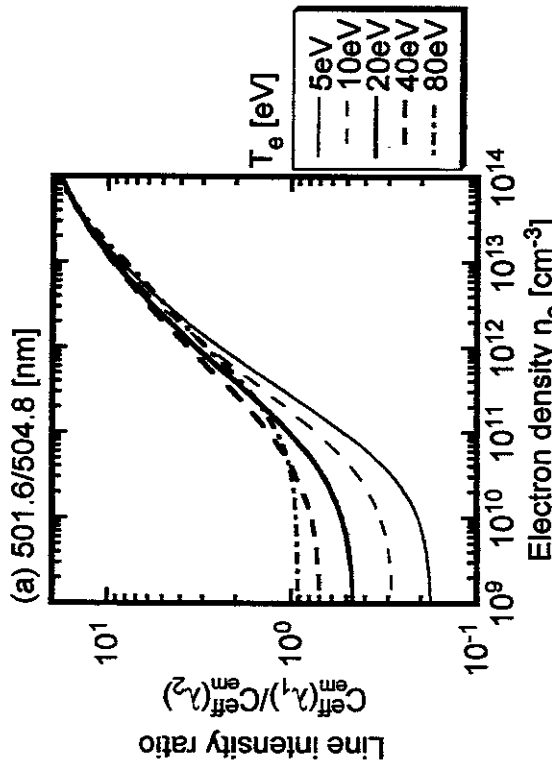


Fig. 4.4(a)

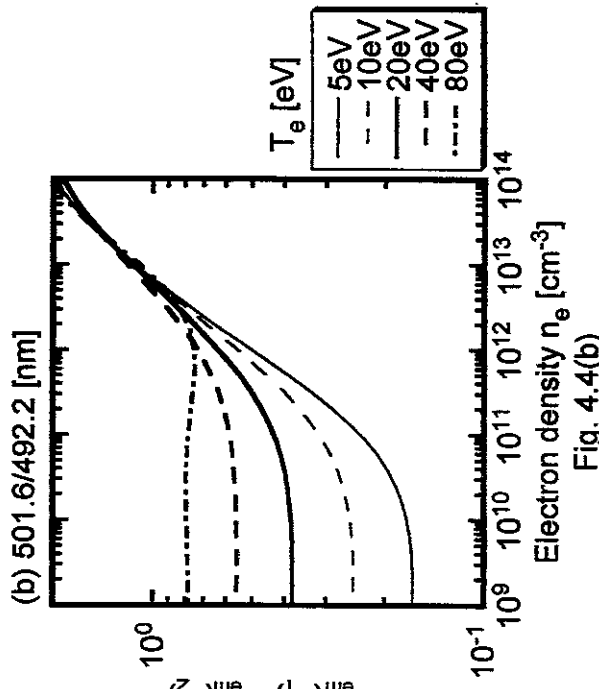


Fig. 4.4(b)

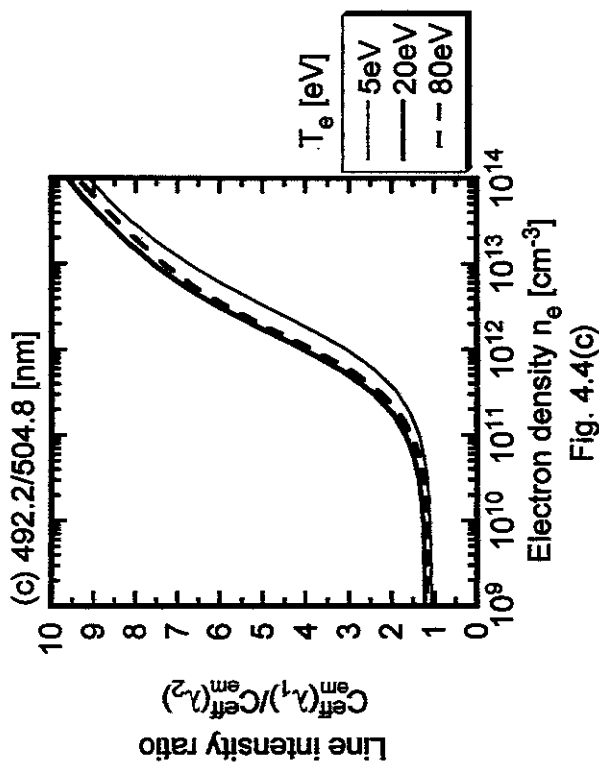


Fig. 4.4(c)

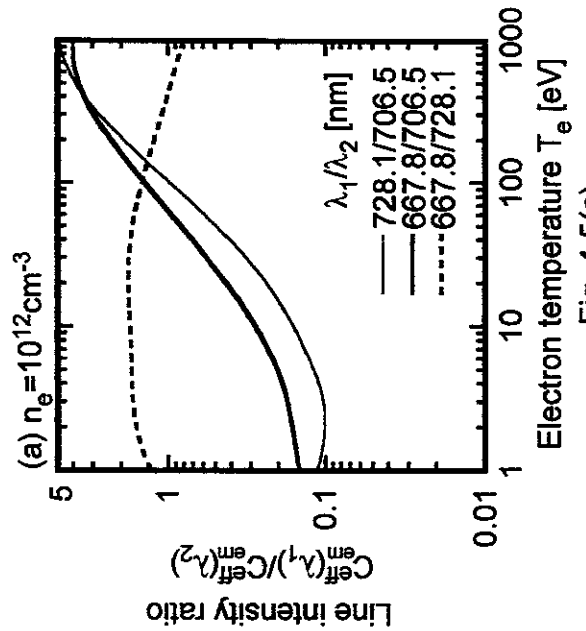


Fig. 4.5(a)

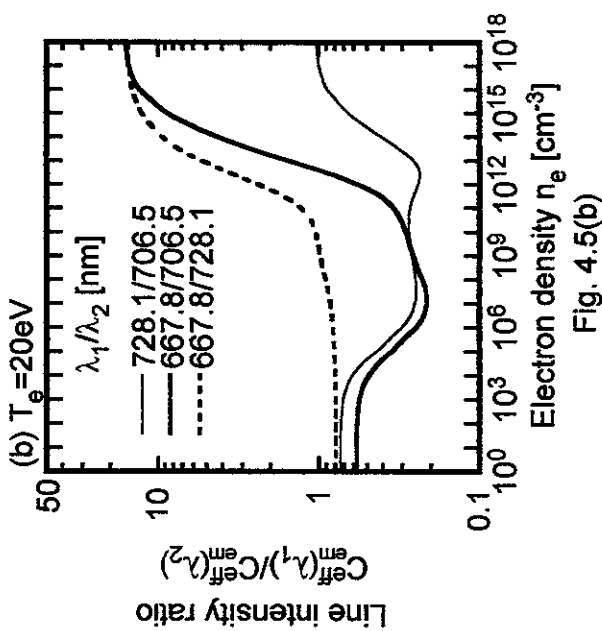


Fig. 4.5(b)

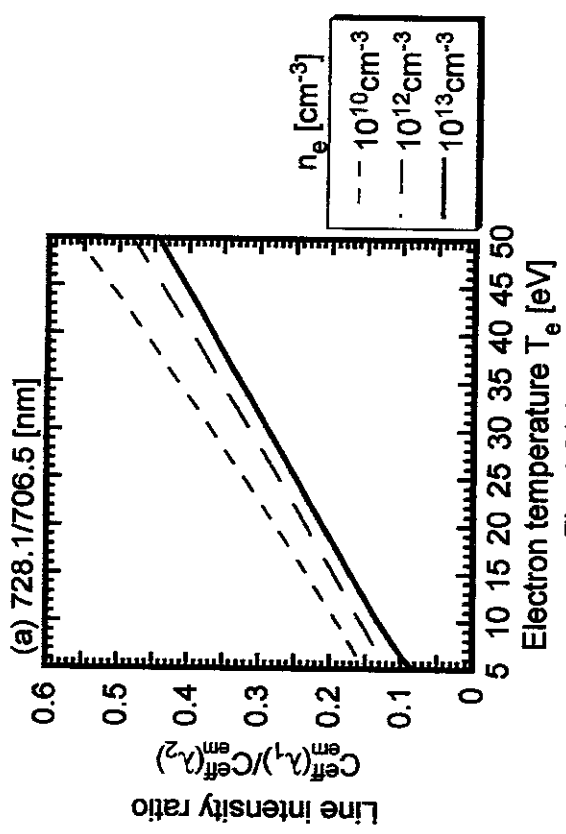


Fig. 4.6(a)

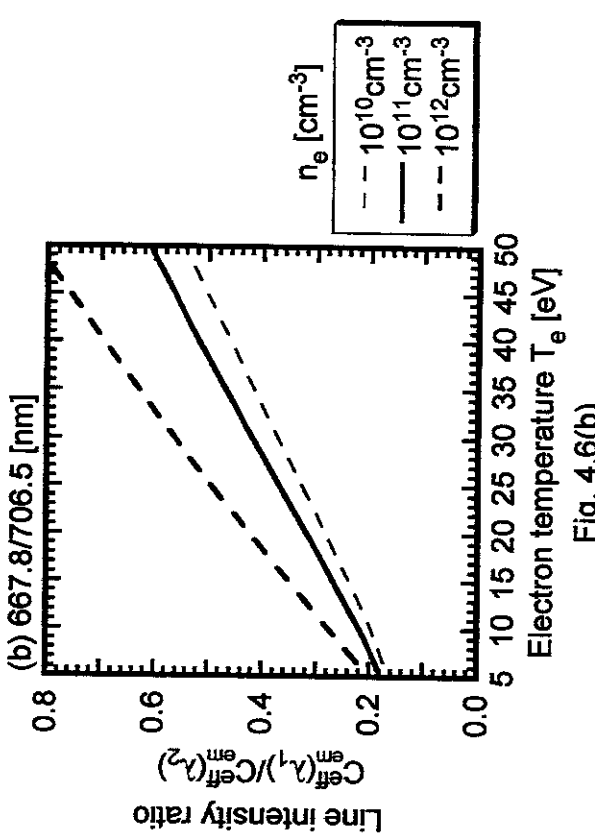


Fig. 4.6(b)

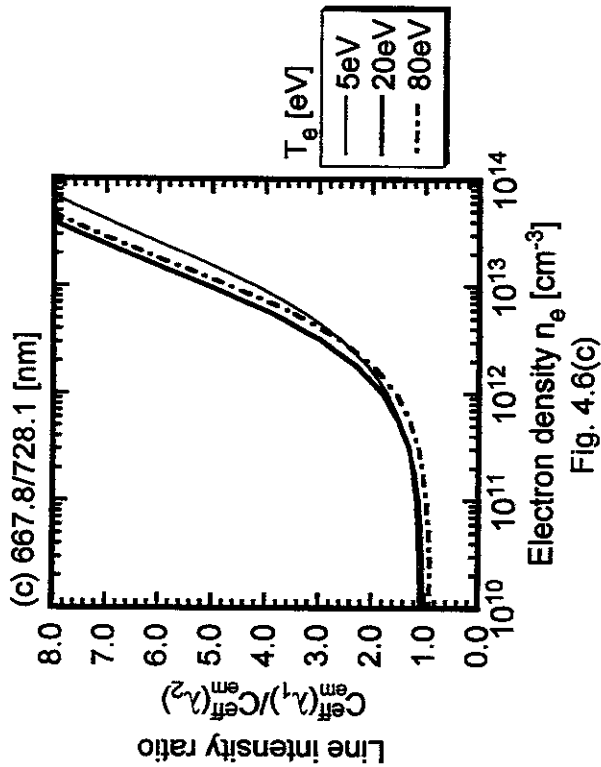


Fig. 4.6(c)

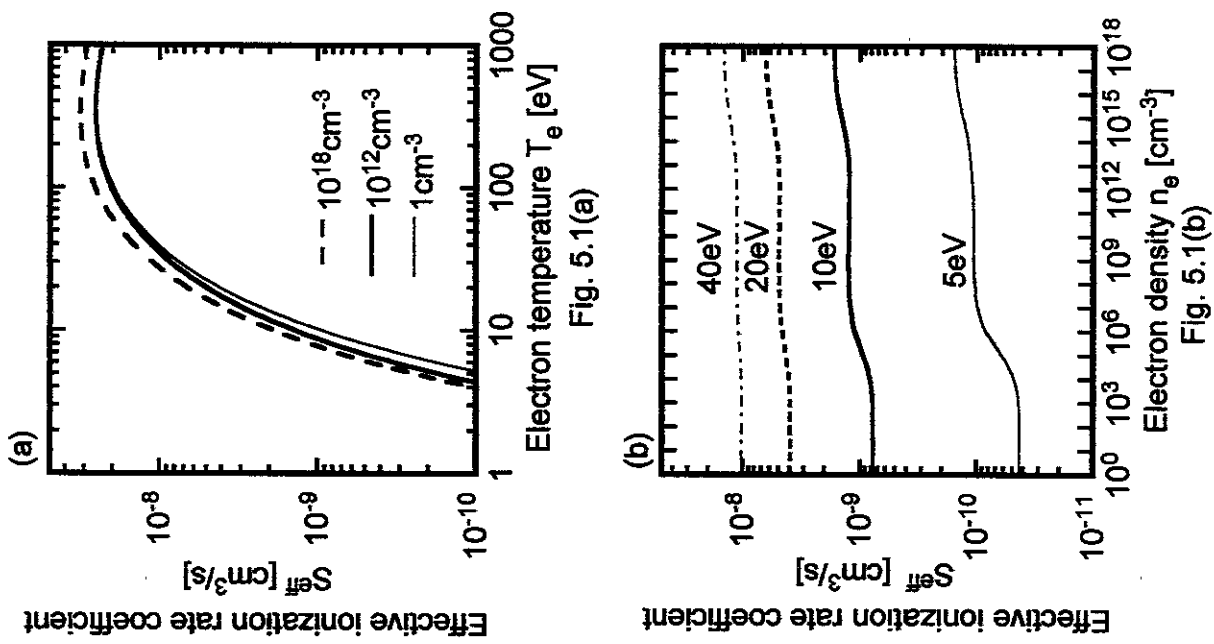


Fig. 5.1(a)

Fig. 5.1(b)

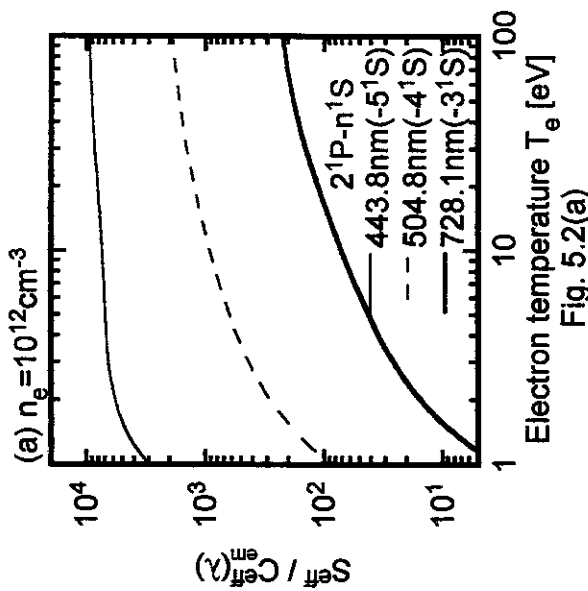


Fig. 5.2(a)

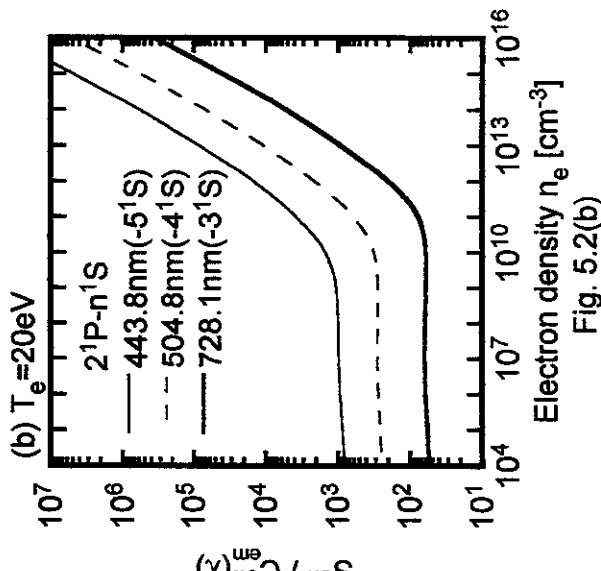


Fig. 5.2(b)

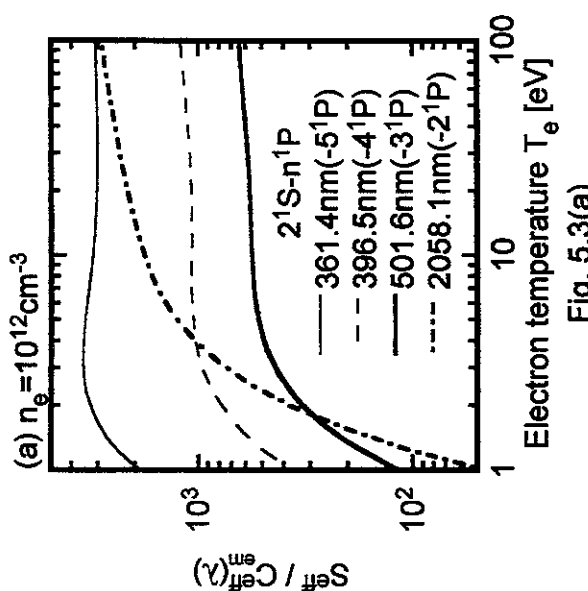


Fig. 5.3(a)

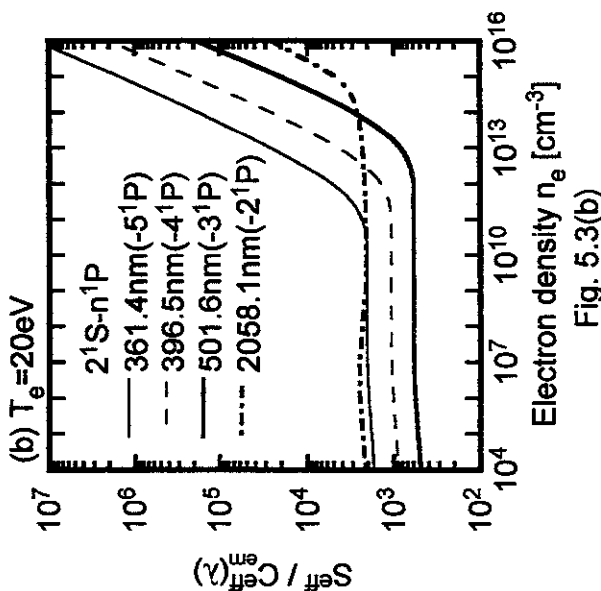


Fig. 5.3(b)

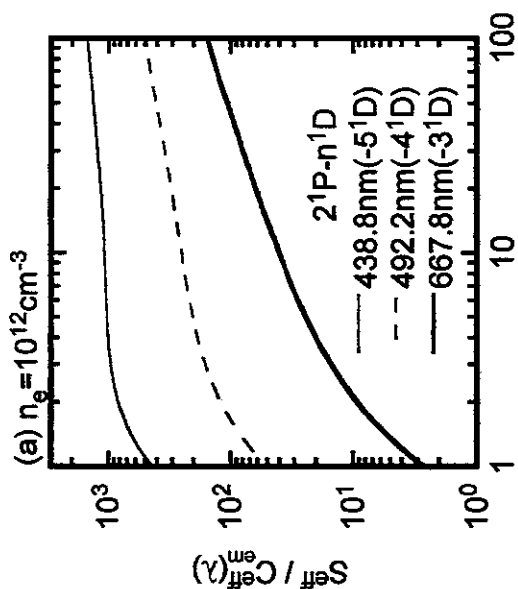


Fig. 5.4(a)

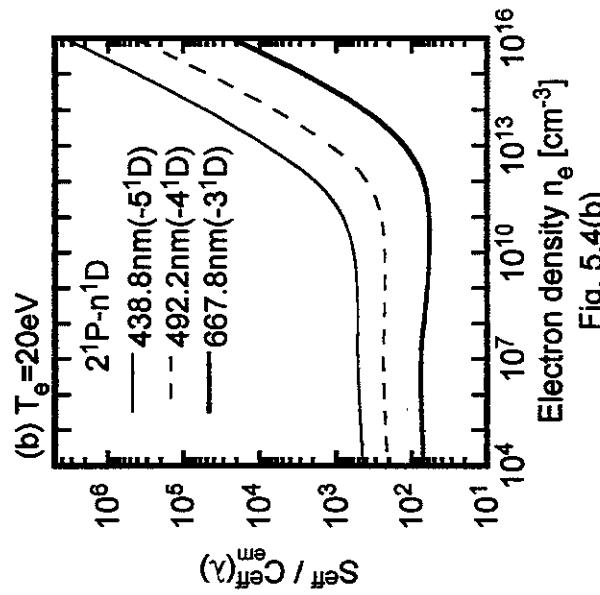


Fig. 5.4(b)

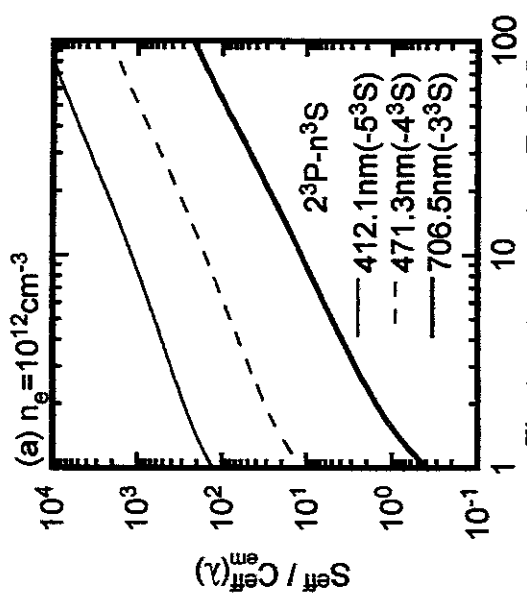


Fig. 5.5(a)

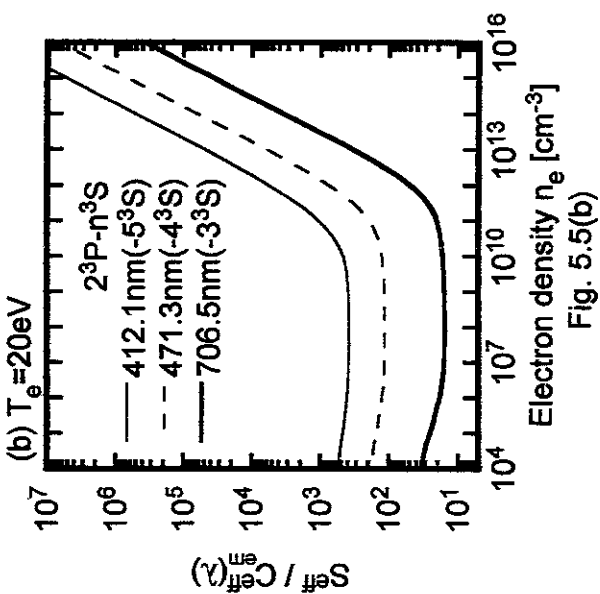


Fig. 5.5(b)

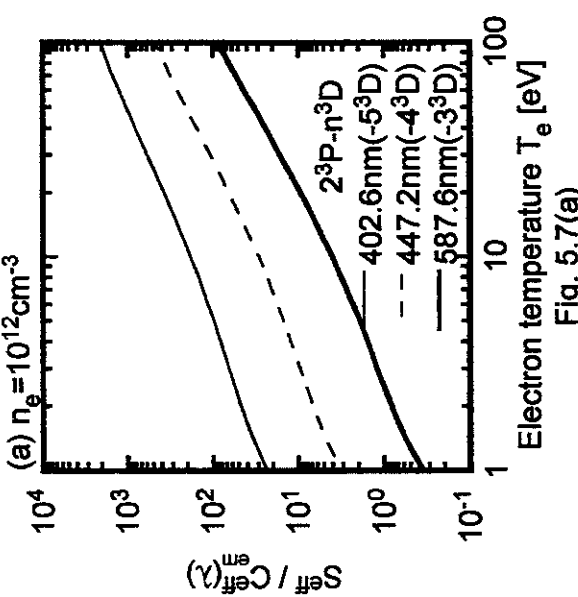


Fig. 5.7(a)

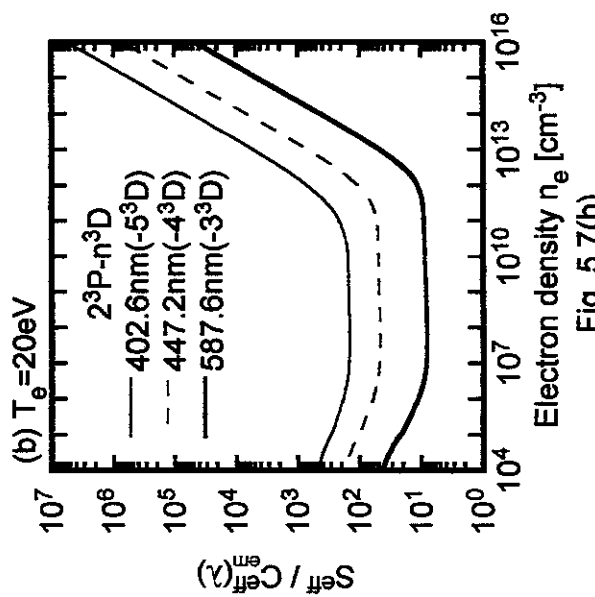


Fig. 5.7(b)

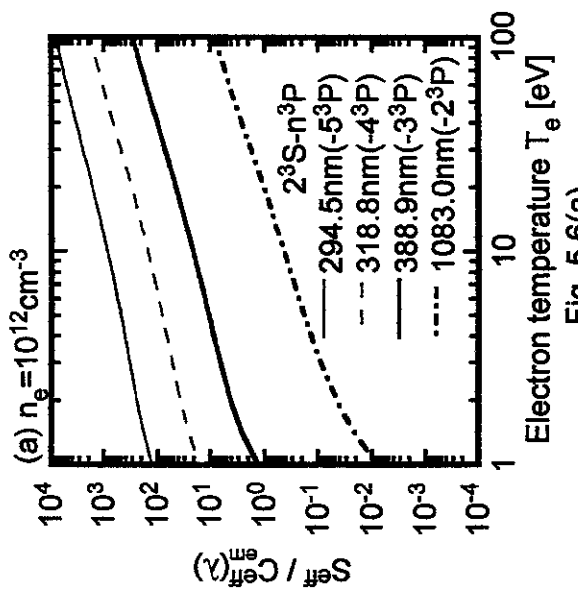


Fig. 5.6(a)

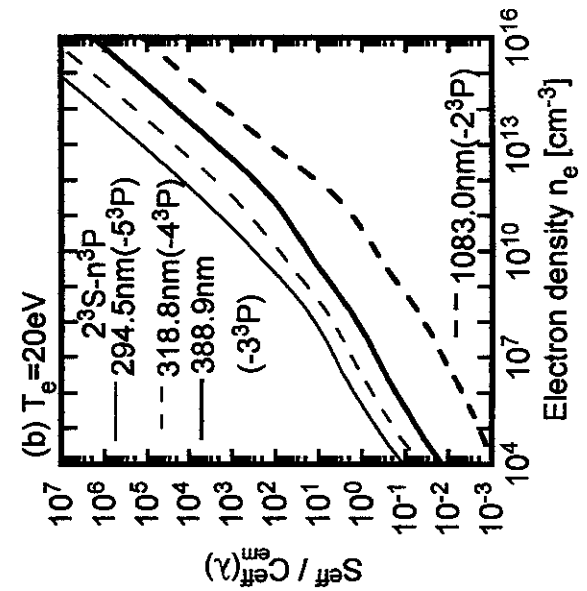


Fig. 5.6(b)

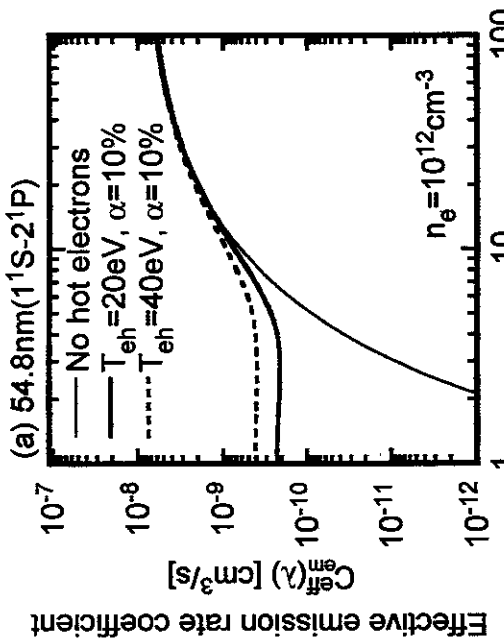


Fig. 6.1(a)
Effective emission rate coefficient
 $C_{\text{eff}}(\lambda) [\text{cm}^3/\text{s}]$
Electron temperature $T_{\text{ec}} [\text{eV}]$

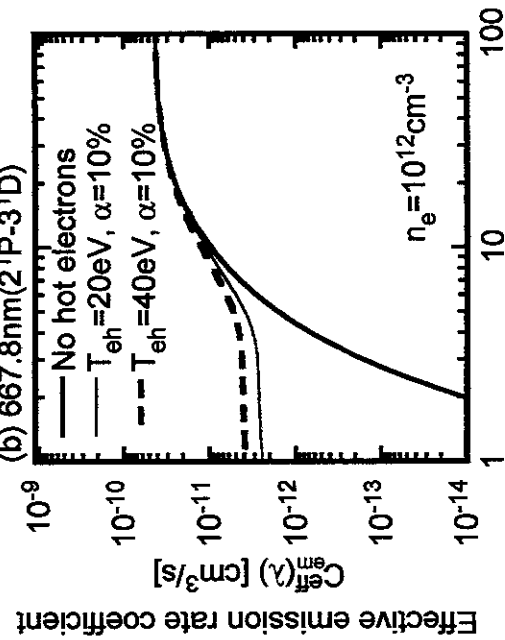


Fig. 6.1(b)
Effective emission rate coefficient
 $C_{\text{eff}}(\lambda) [\text{cm}^3/\text{s}]$
Electron temperature $T_{\text{ec}} [\text{eV}]$

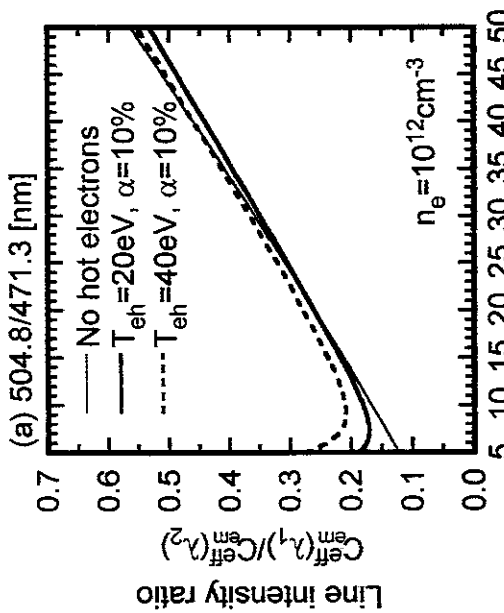


Fig. 6.2(a)
Line intensity ratio
 $C_{\text{eff}}(\lambda_1)/C_{\text{eff}}(\lambda_2)$
Electron temperature $T_{\text{ec}} [\text{eV}]$

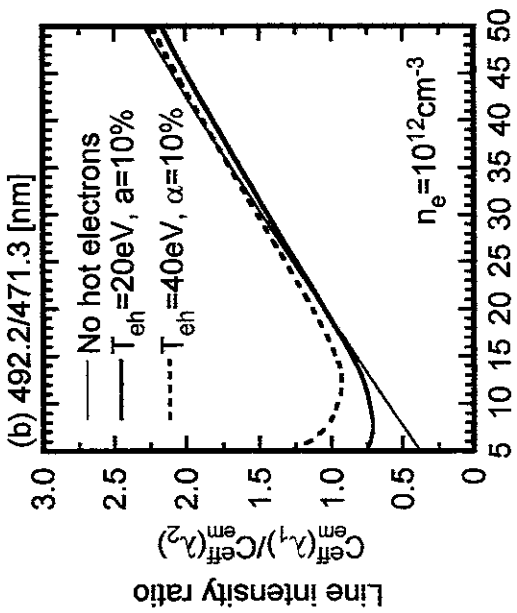


Fig. 6.2(b)
Line intensity ratio
 $C_{\text{eff}}(\lambda_1)/C_{\text{eff}}(\lambda_2)$
Electron temperature $T_{\text{ec}} [\text{eV}]$

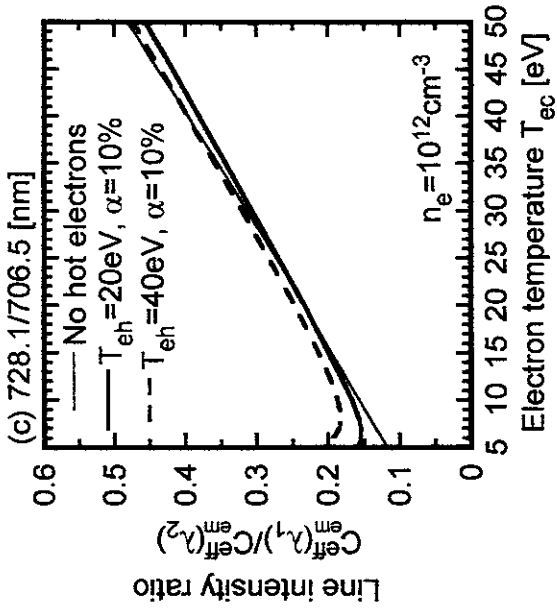


Fig. 6.2(c)

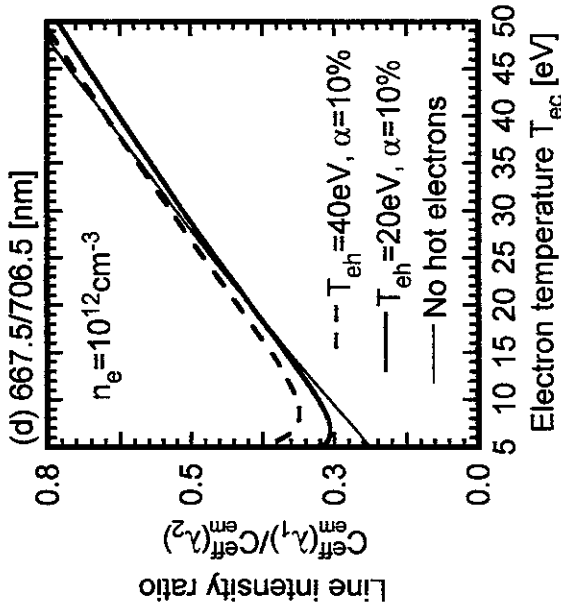


Fig. 6.2(d)

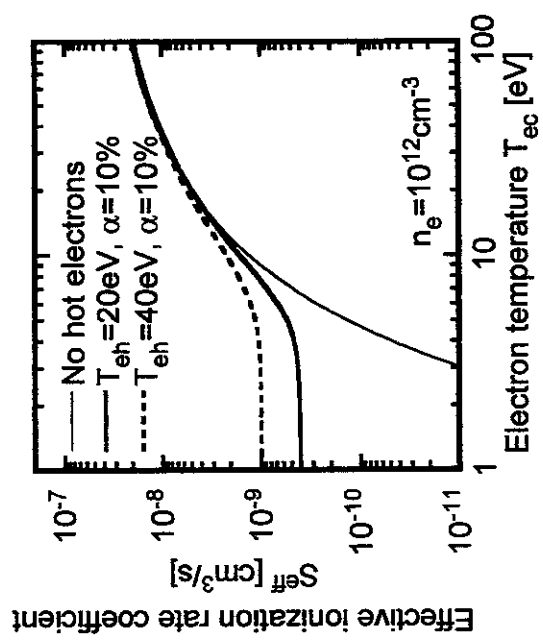


Fig. 6.3

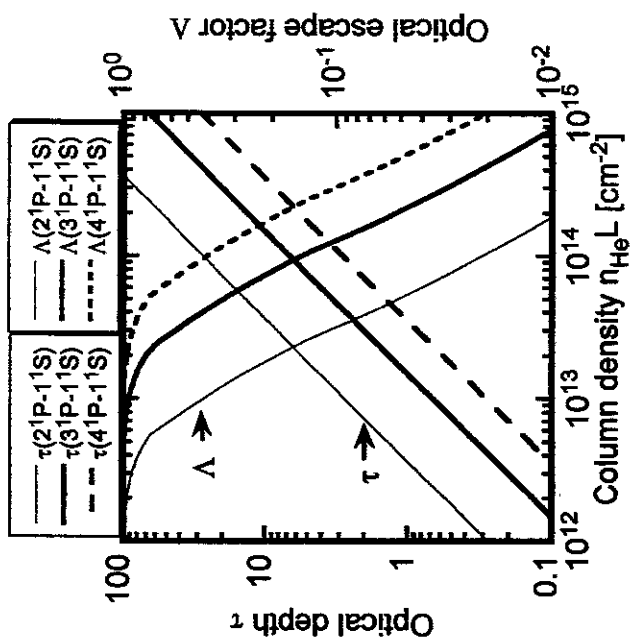


Fig. 7.1

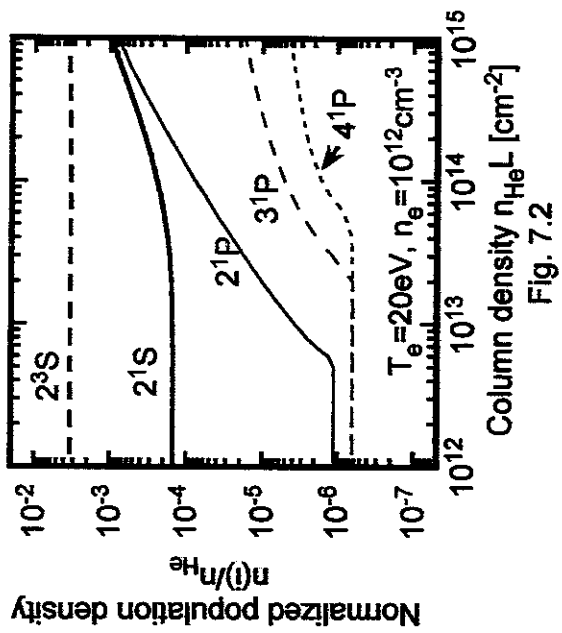


Fig. 7.2

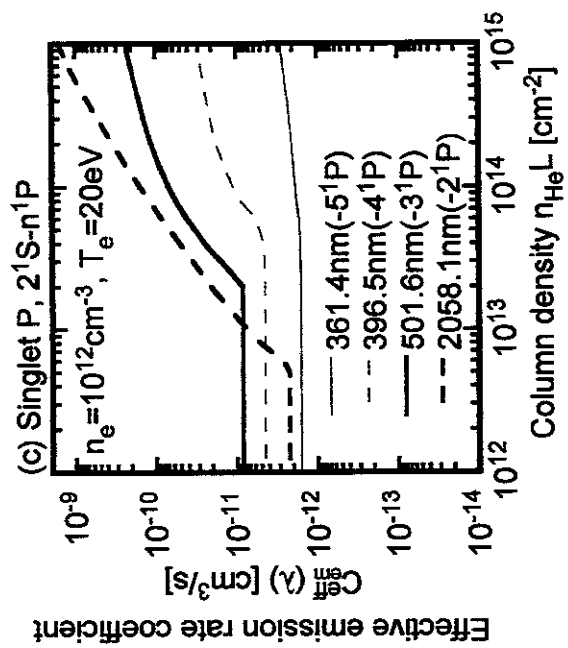


Fig. 7.3(c)

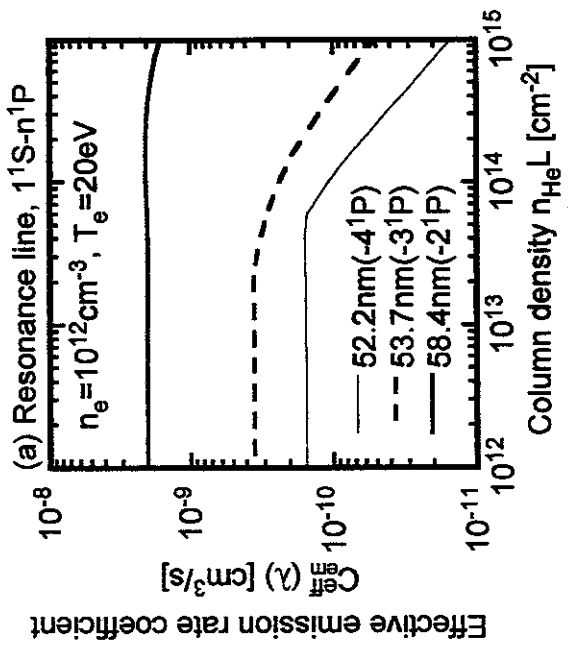


Fig. 7.3(a)

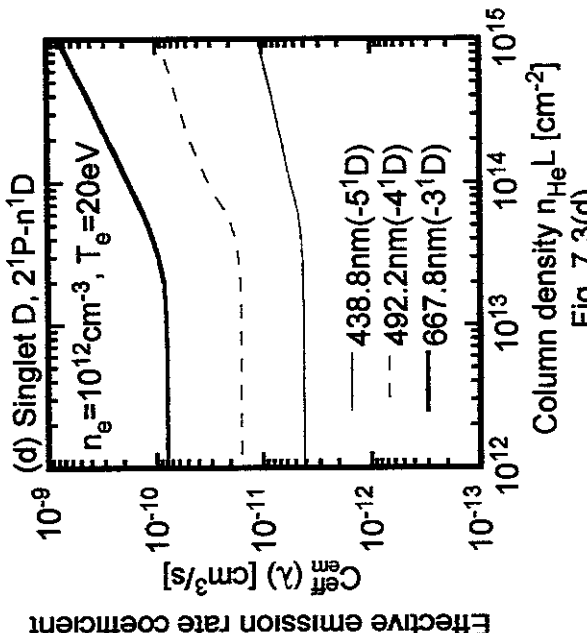


Fig. 7.3(d)

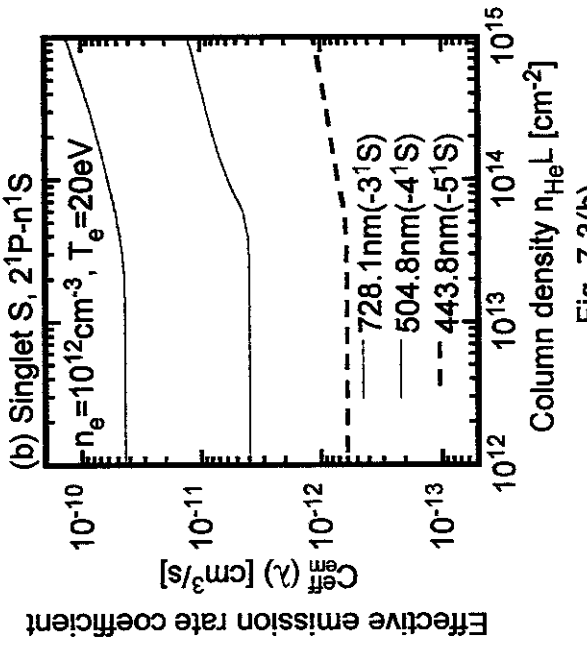


Fig. 7.3(b)

Effective emission rate coefficient

Fig. 7.3(a)

Effective emission rate coefficient

Fig. 7.3(b)

Effective emission rate coefficient

Fig. 7.3(c)

Effective emission rate coefficient

Fig. 7.3(d)

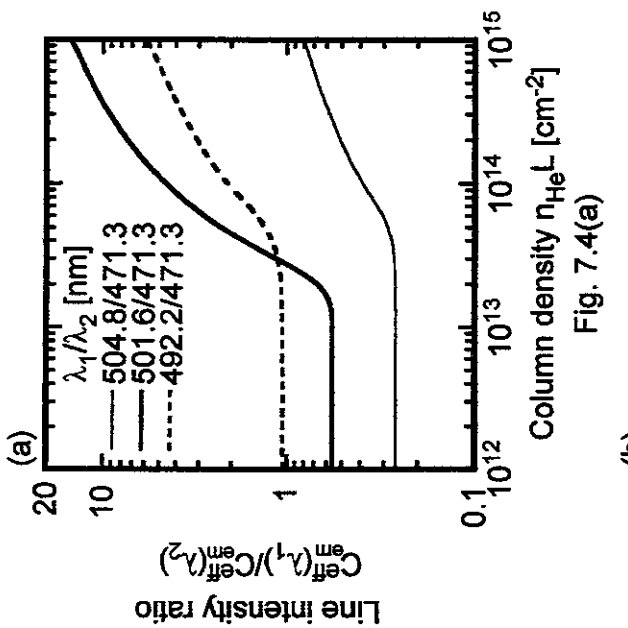


Fig. 7.4(a)

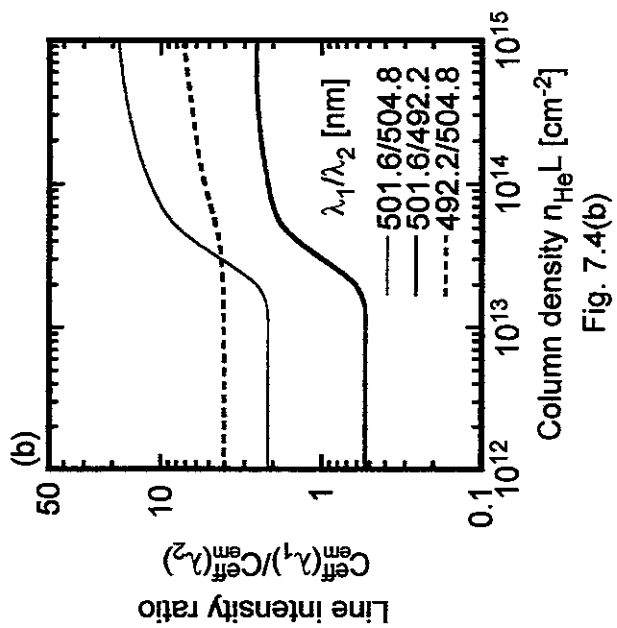


Fig. 7.4(b)

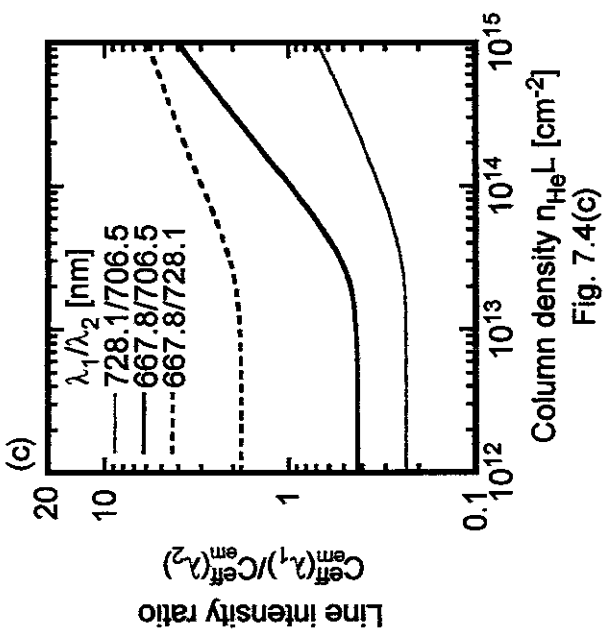
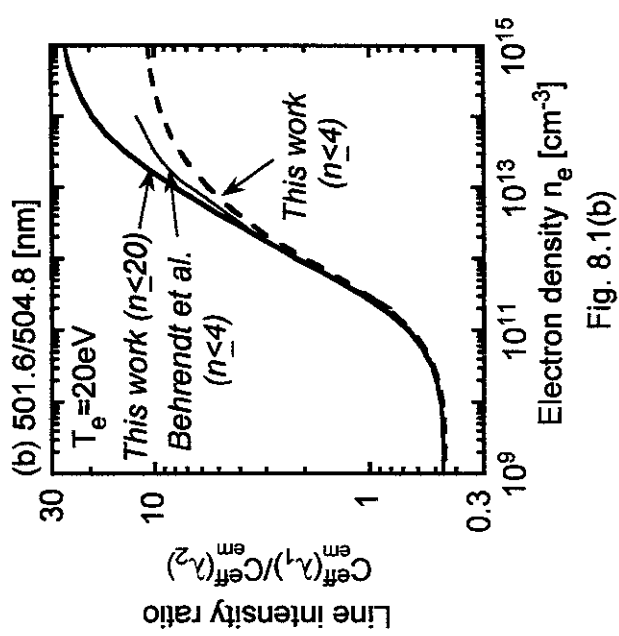
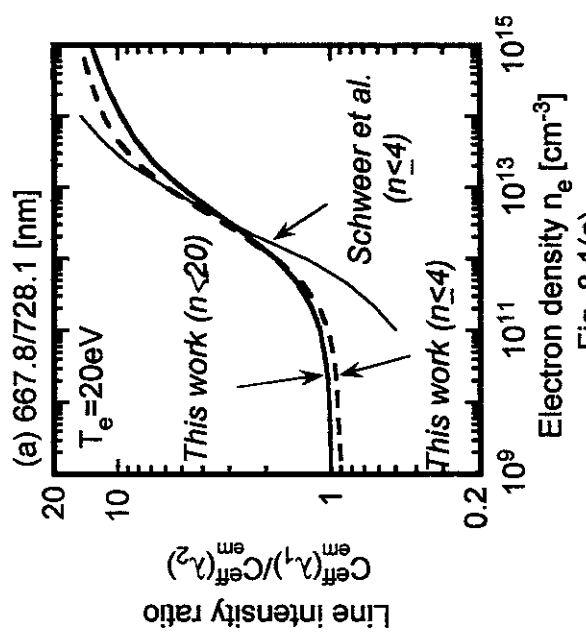
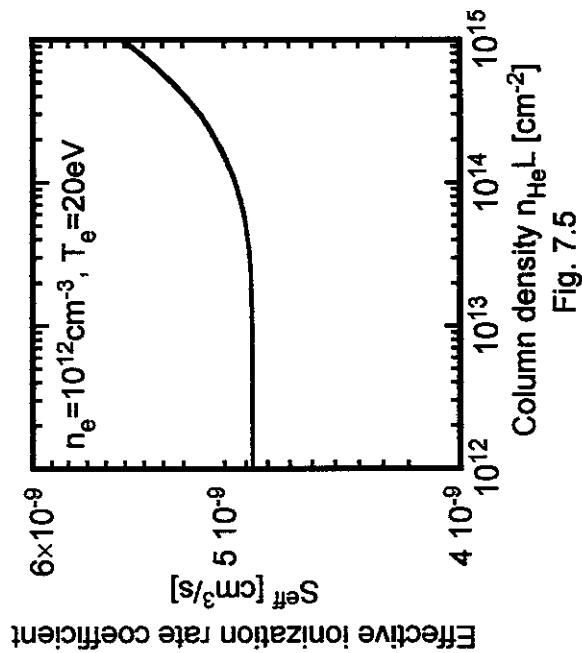


Fig. 7.4(c)



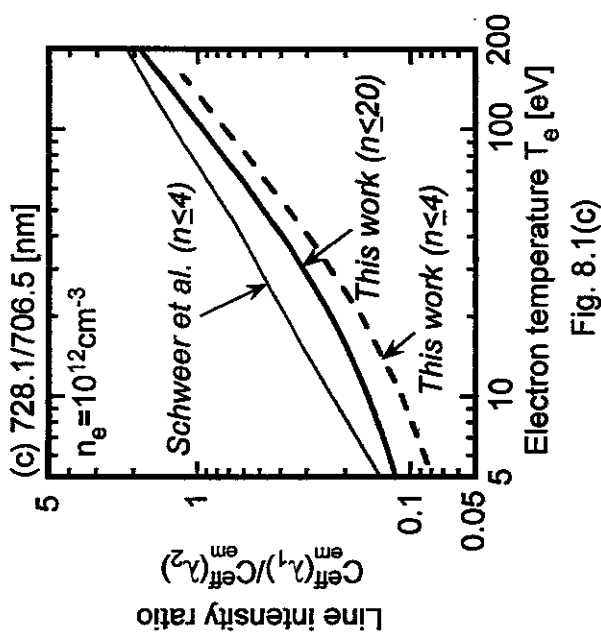


Fig. 8.1(c)

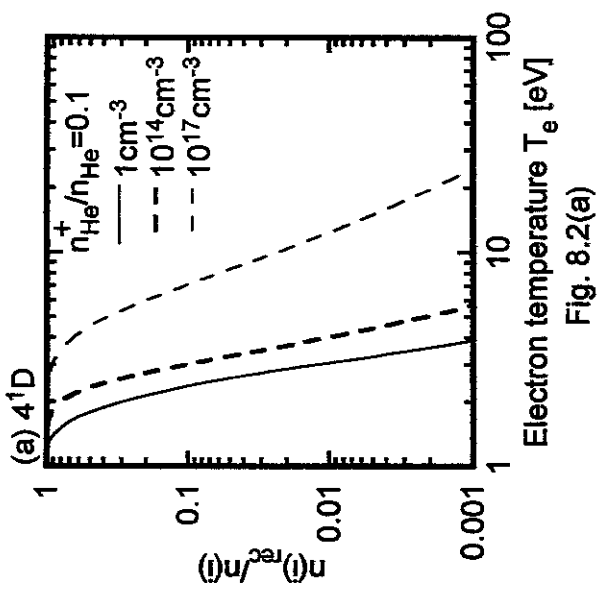


Fig. 8.2(a)

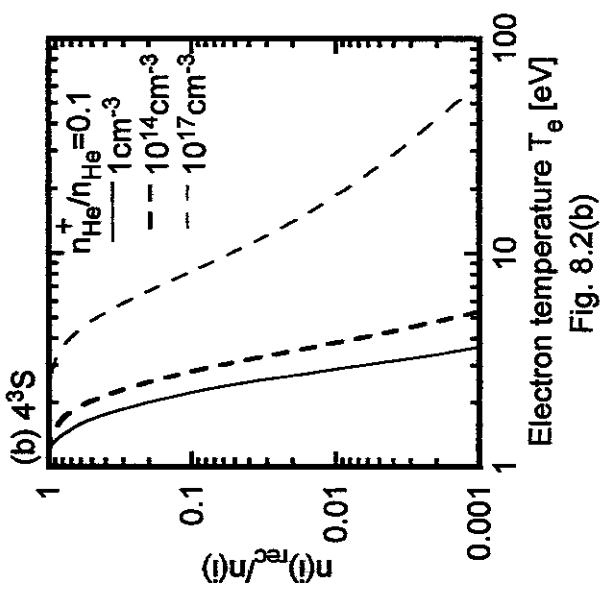


Fig. 8.2(b)

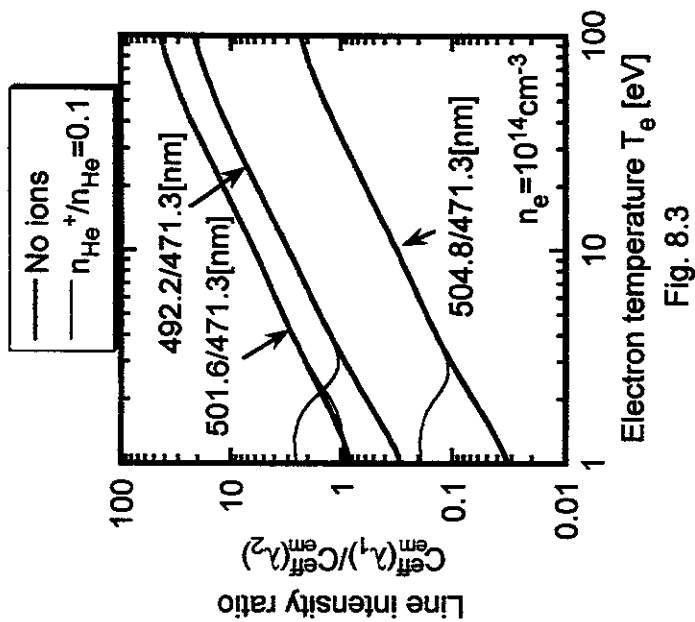


Fig. 8.3

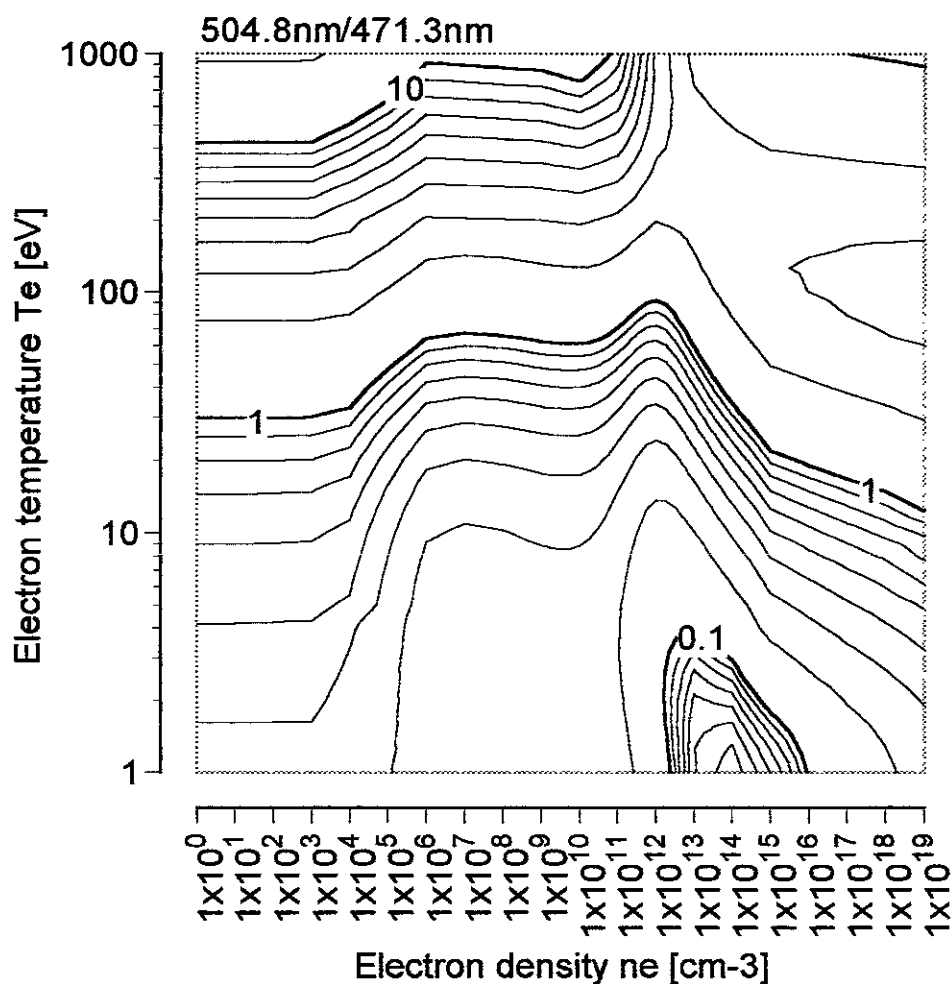


Fig. A1(a)

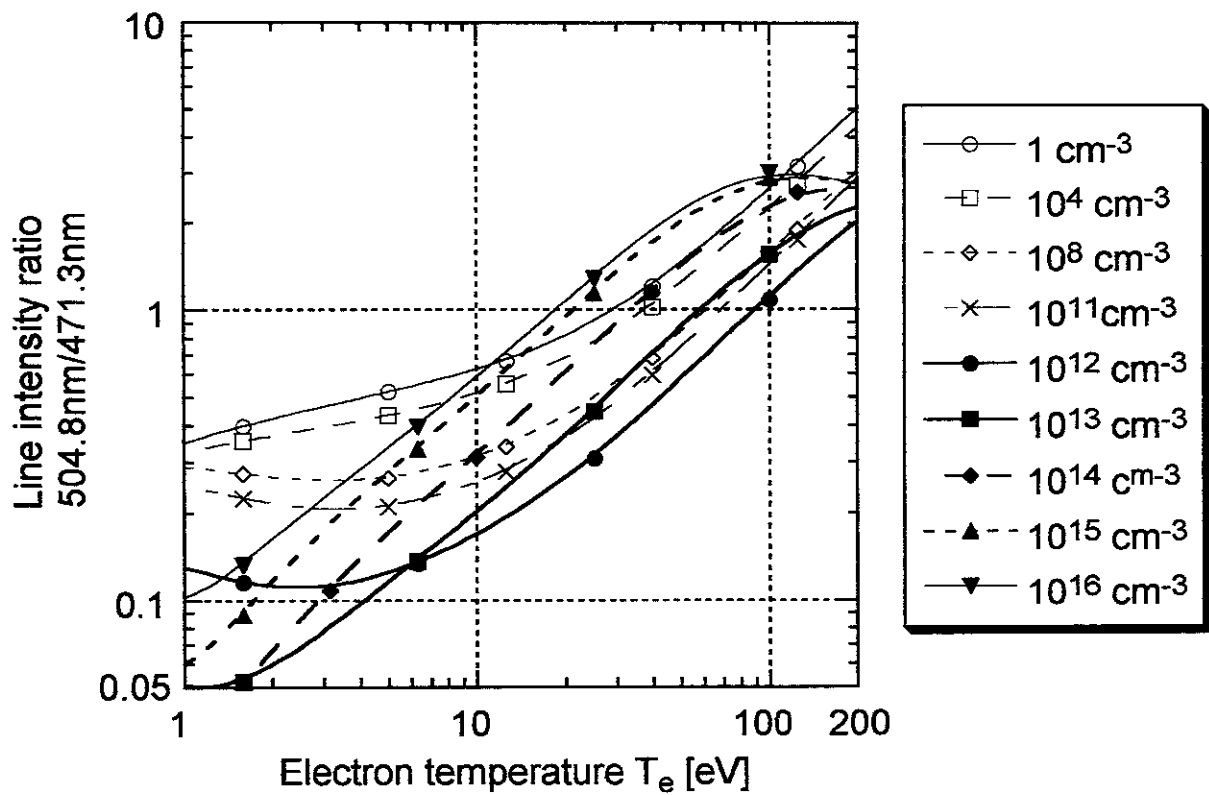


Fig A1(b)

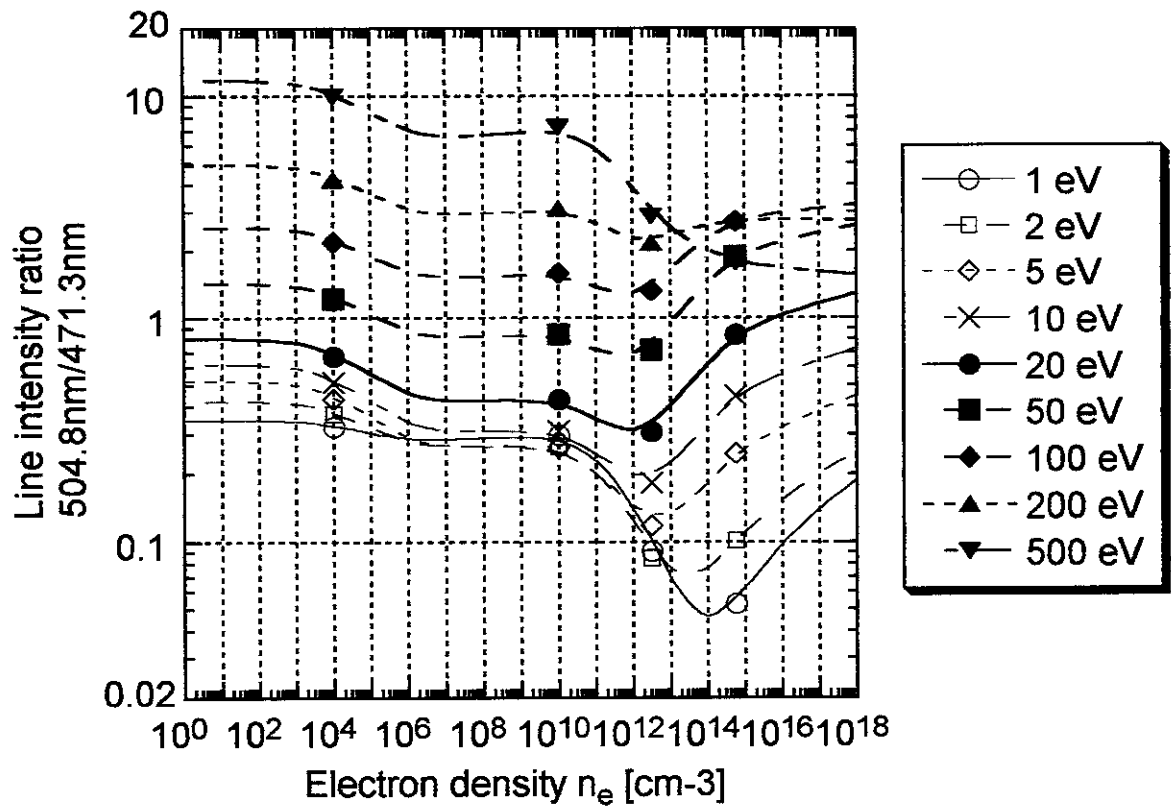


Fig. A1(c)

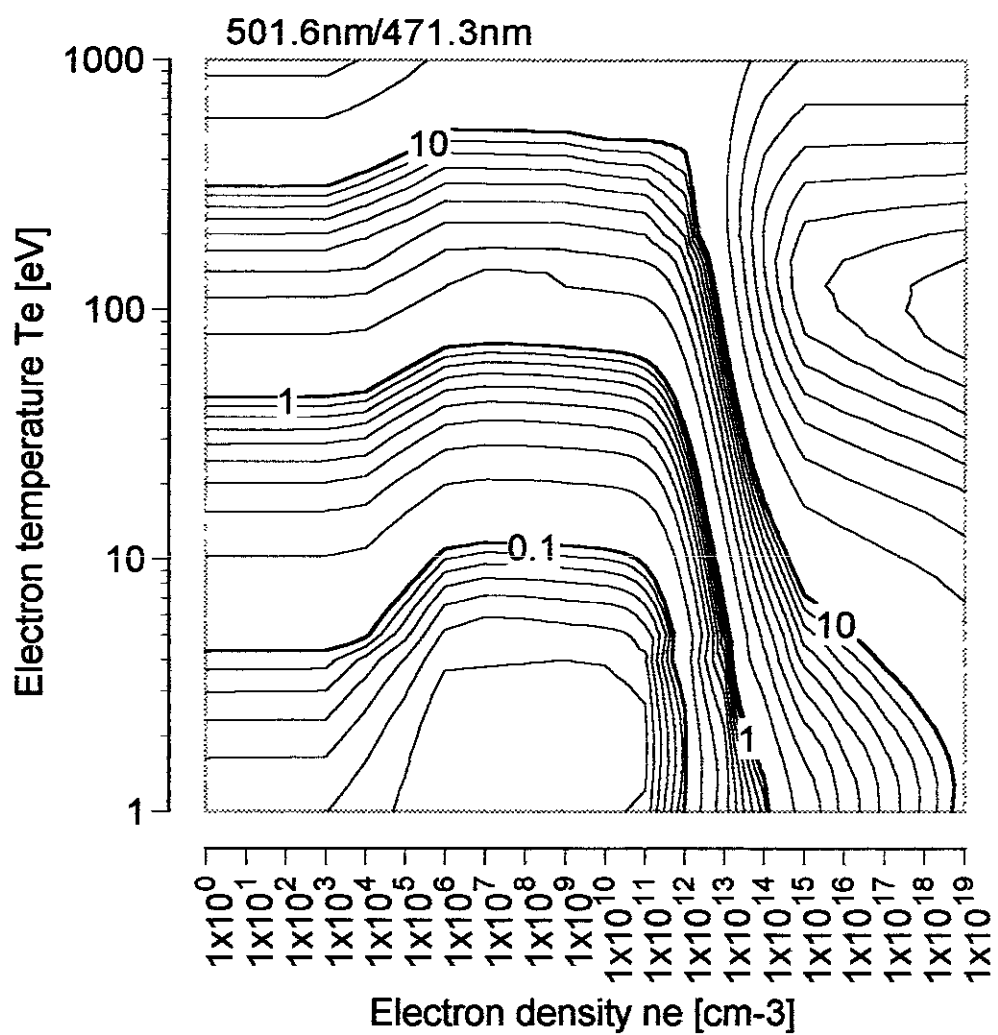


Fig. A2(a)

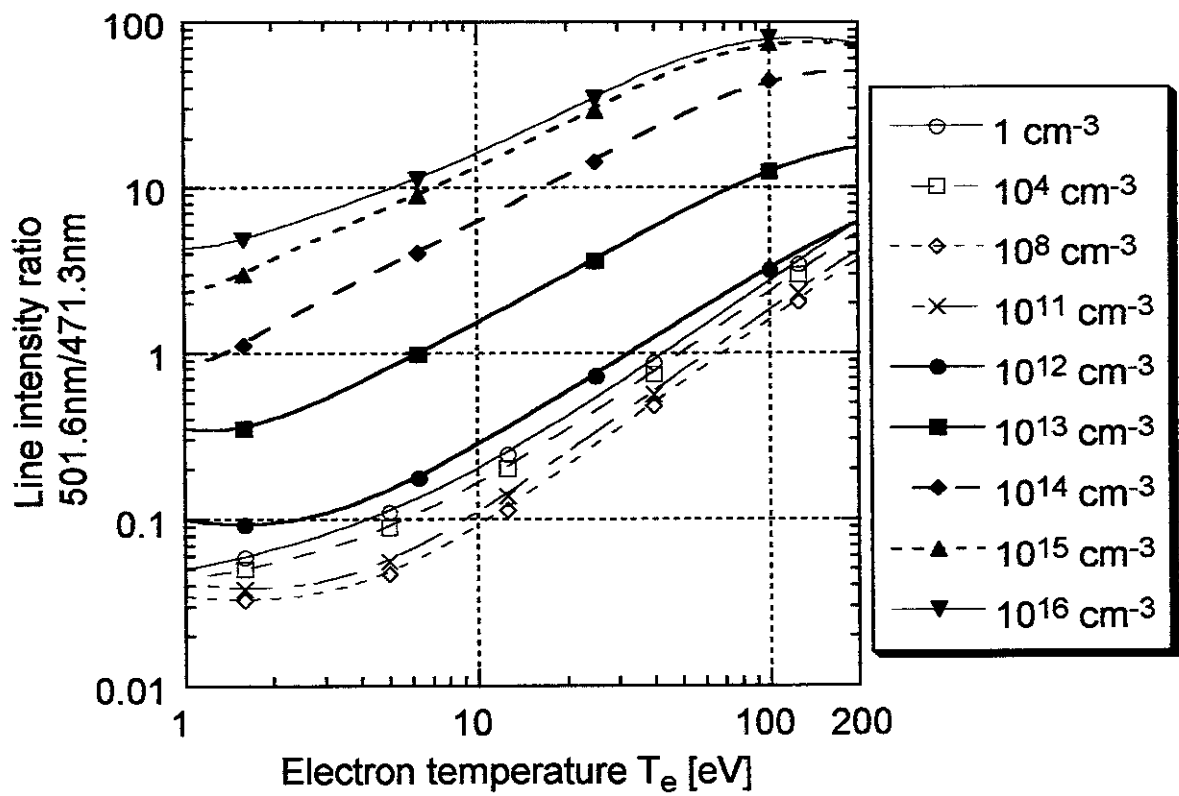


Fig. A2(b)

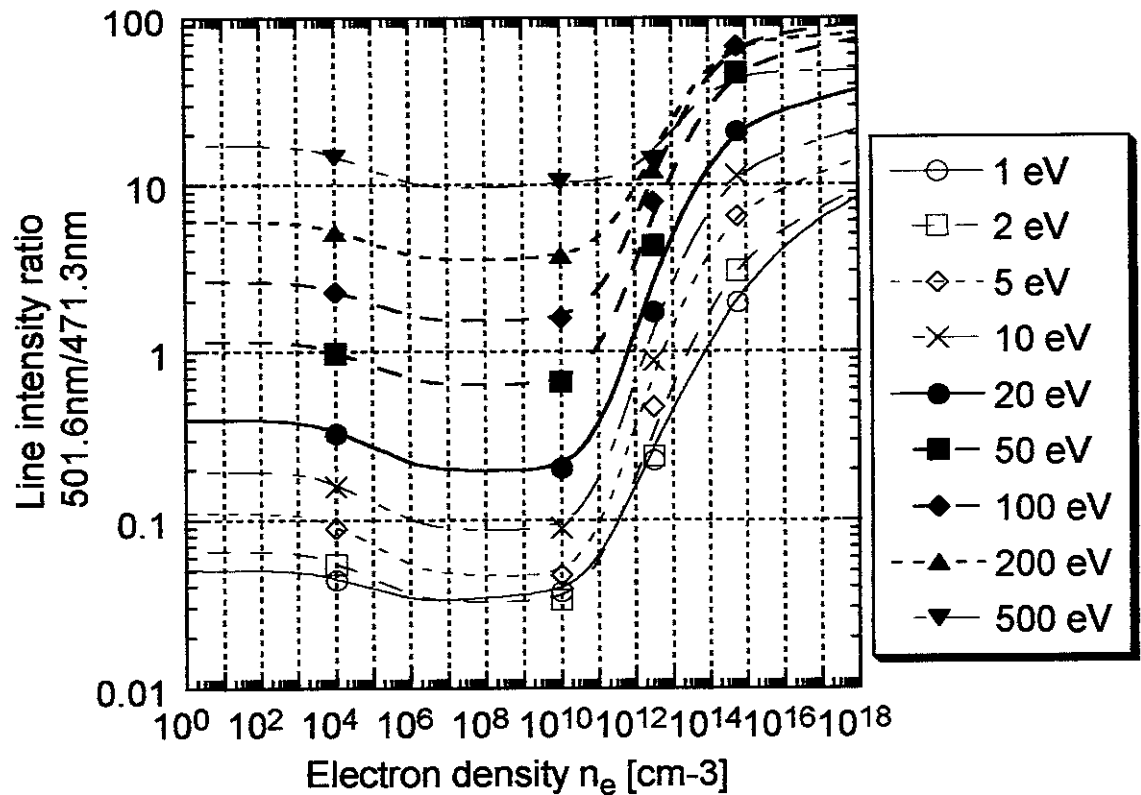


Fig. A2(c)

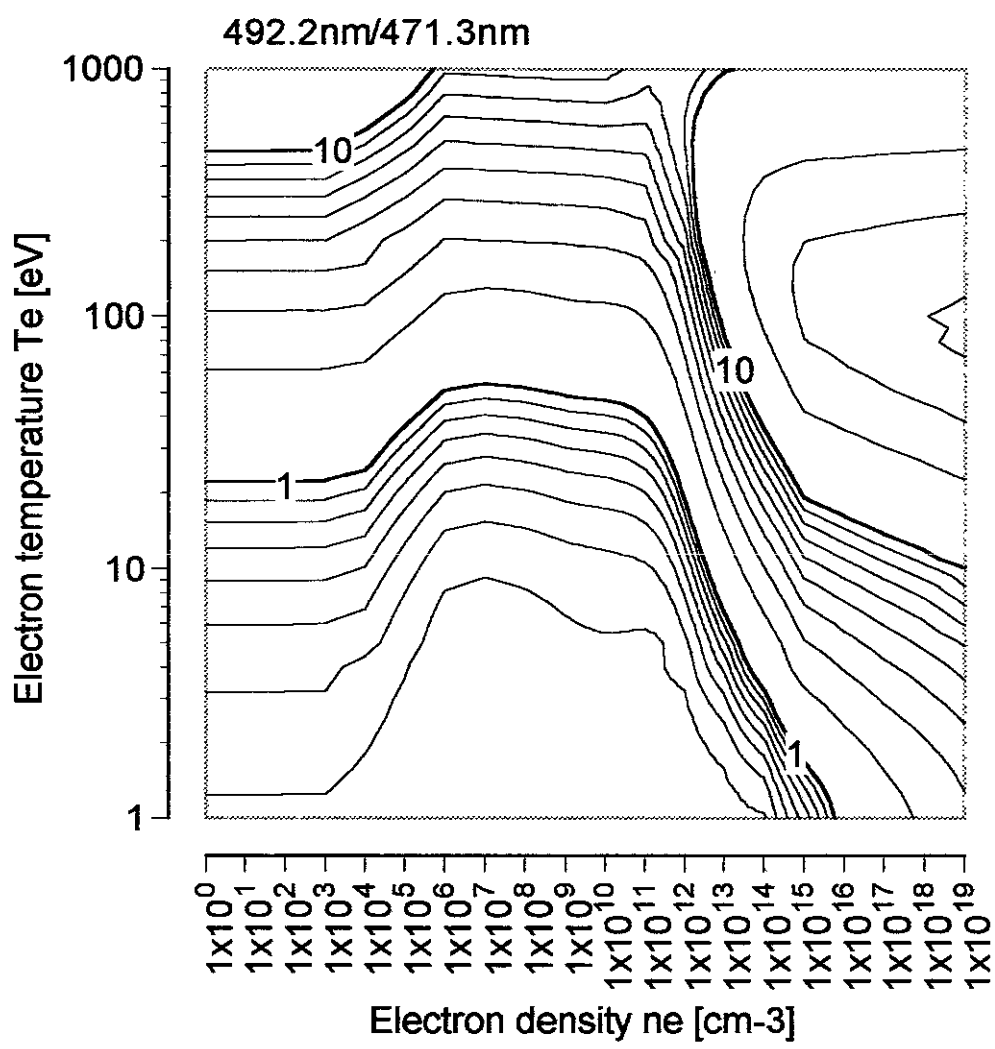


Fig. A3(a)

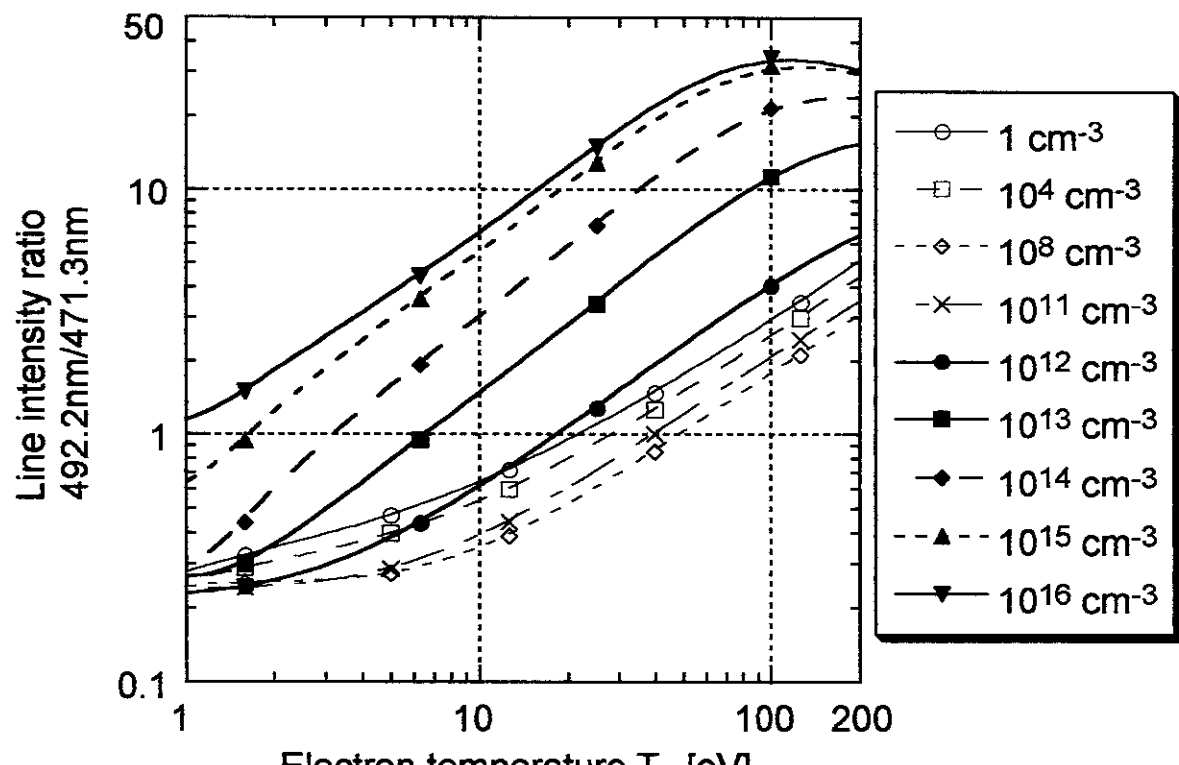


Fig. A3(b)

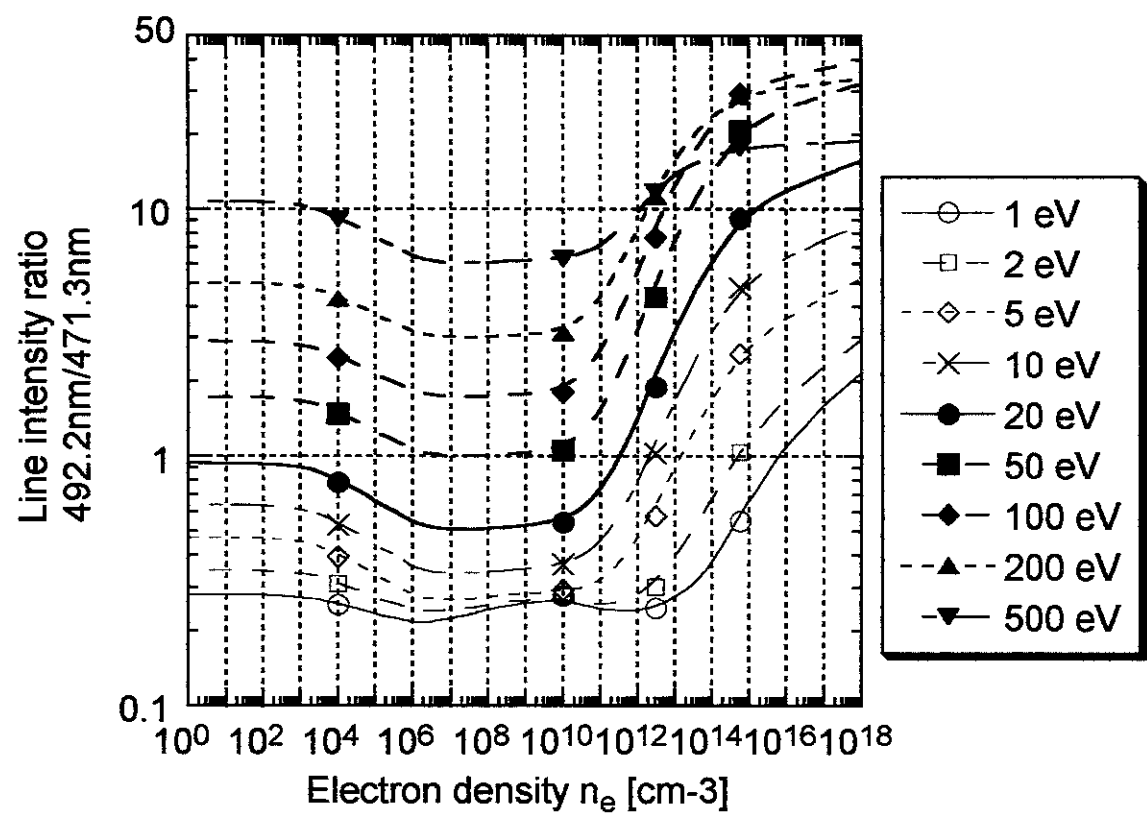


Fig. A3(c)

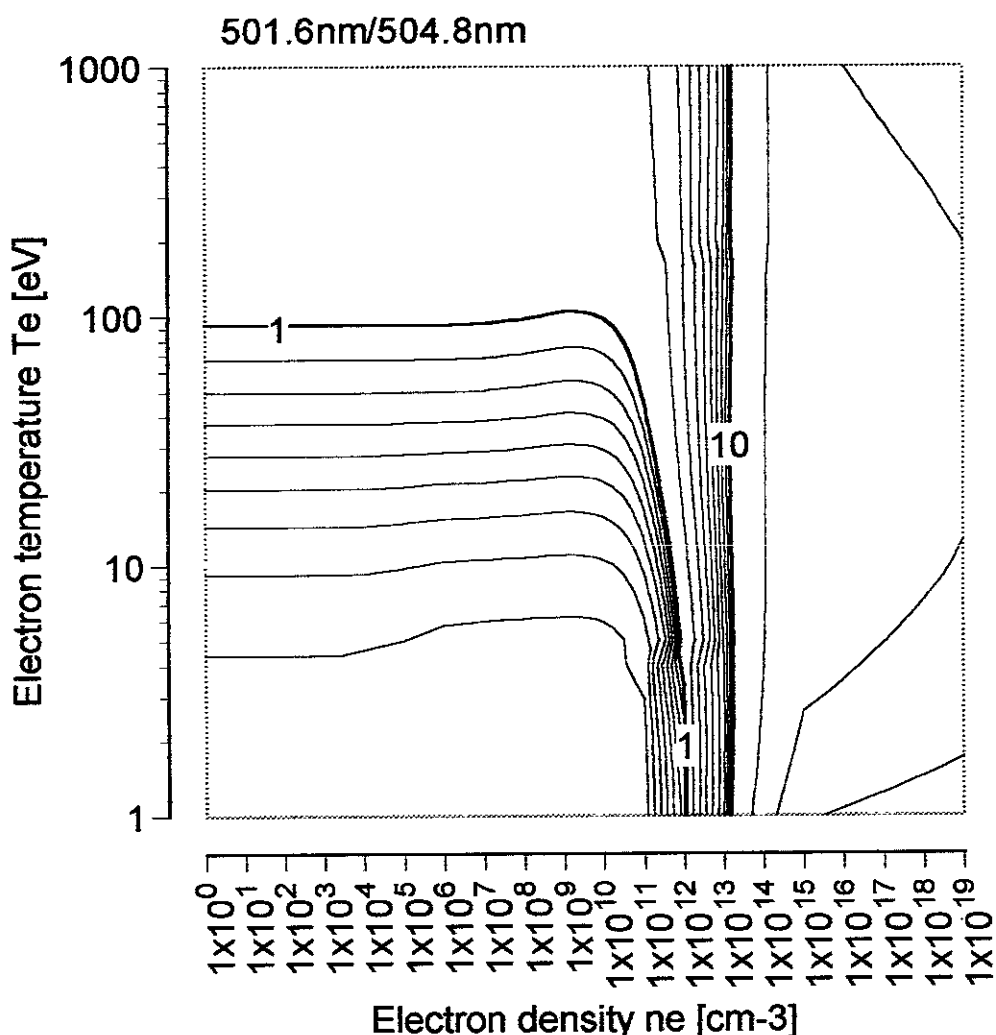


Fig. A4(a)

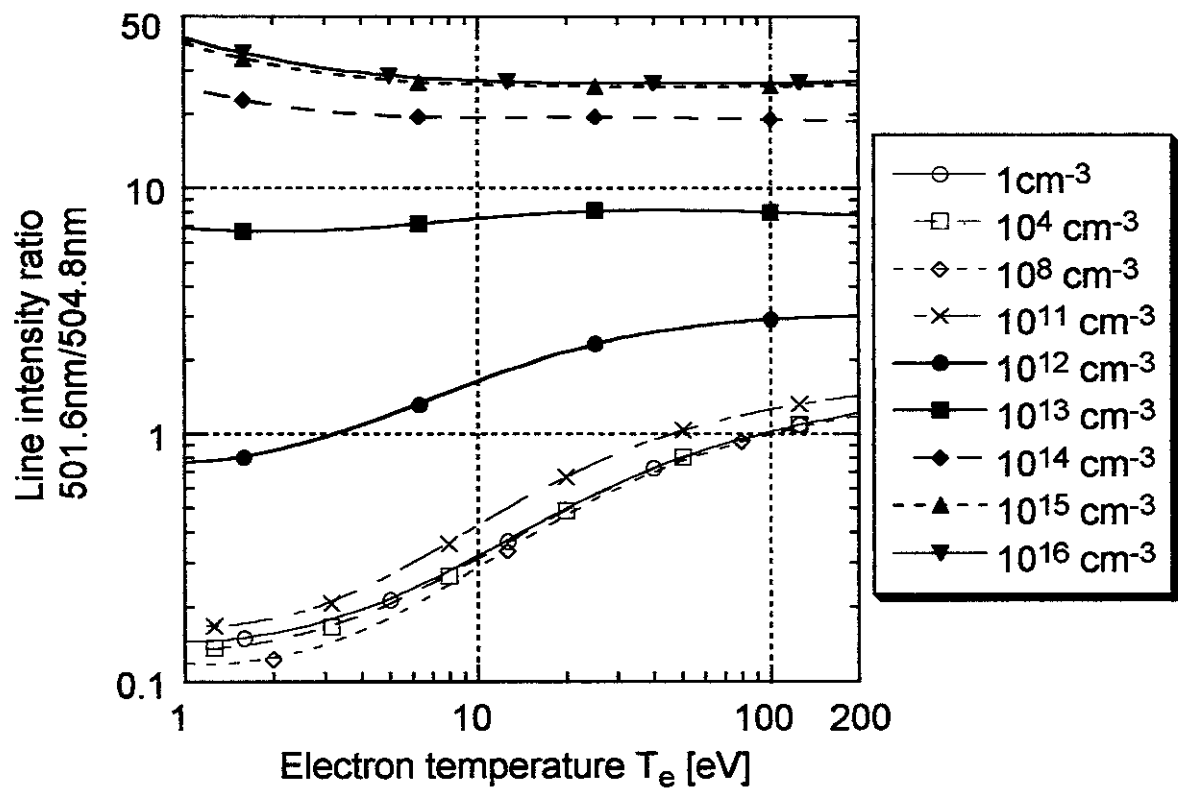


Fig. A4(b)

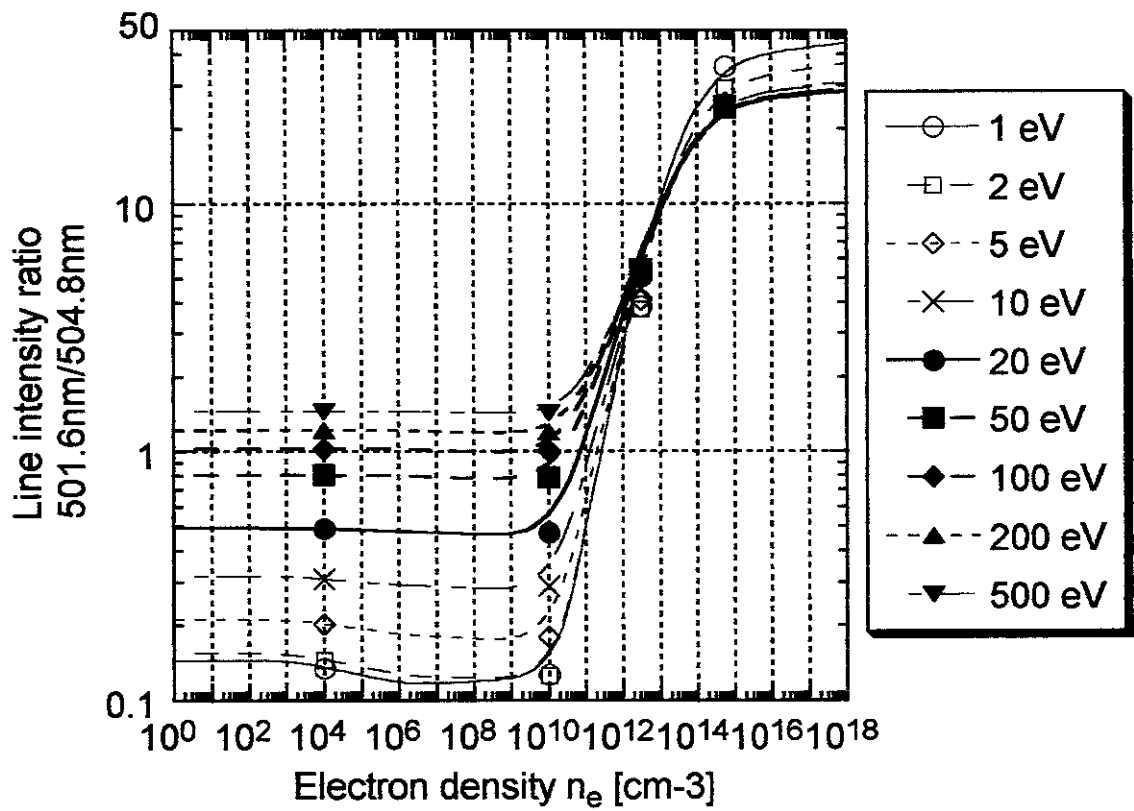


Fig A4(c)

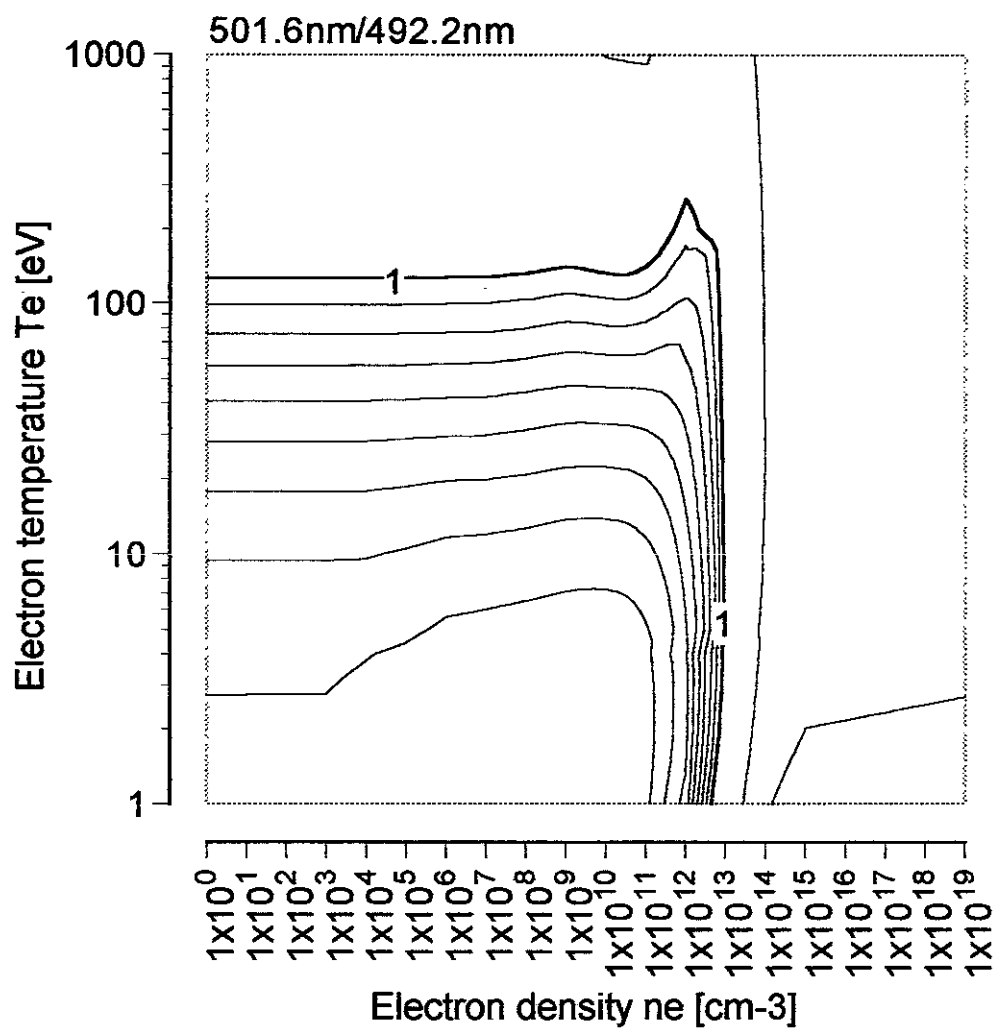


Fig. A5(a)

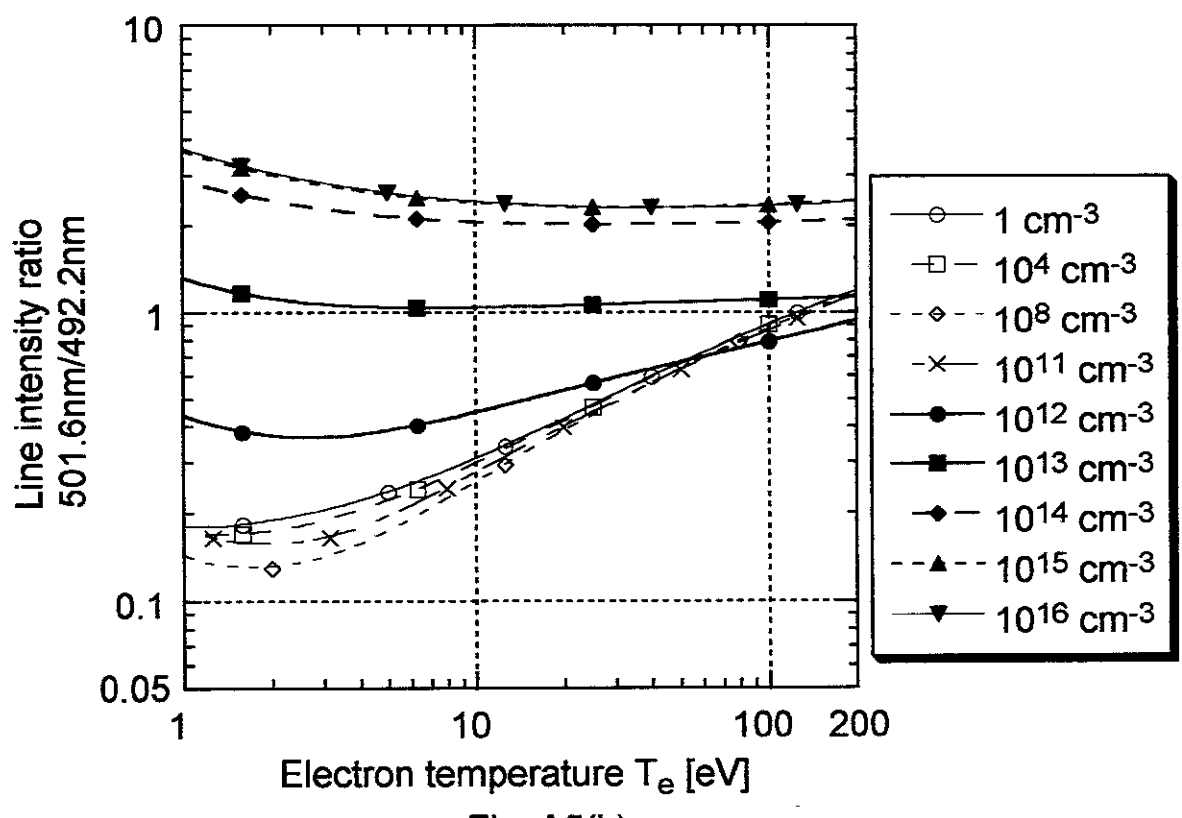


Fig. A5(b)

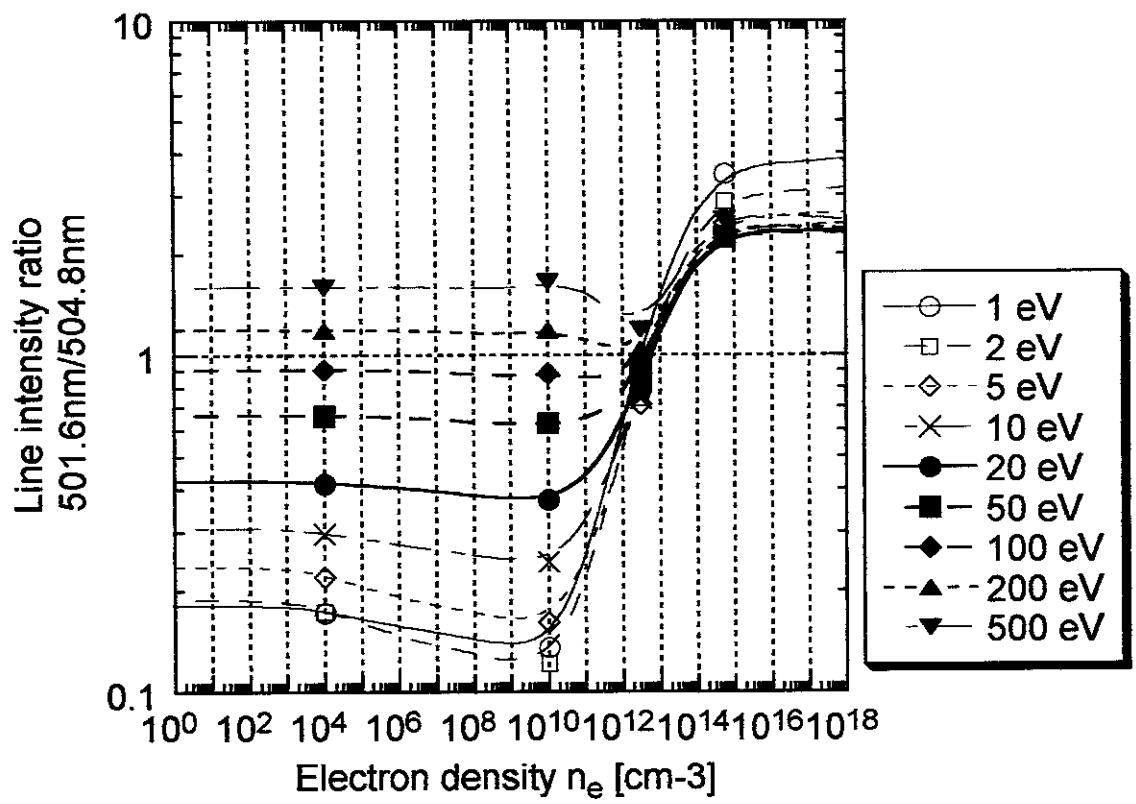


Fig. A5(c)

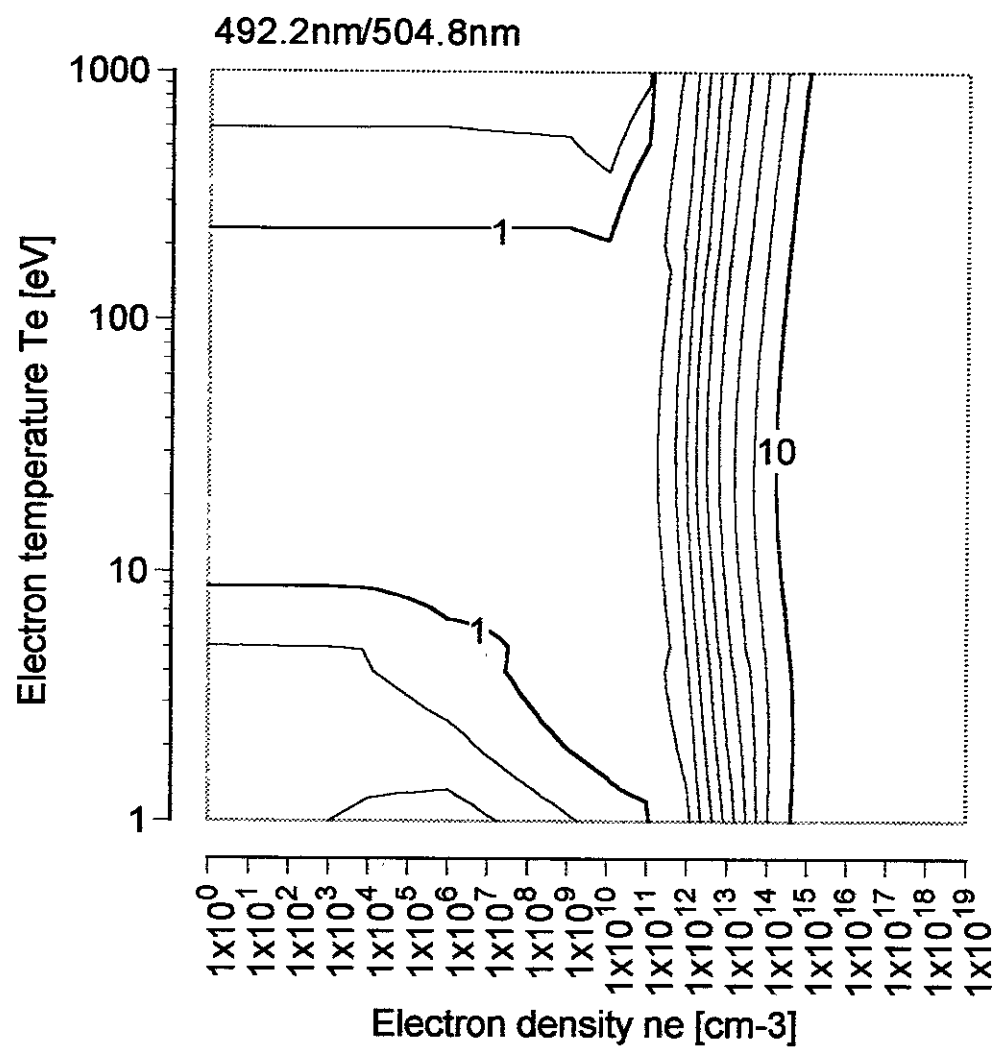


Fig. A6(a)

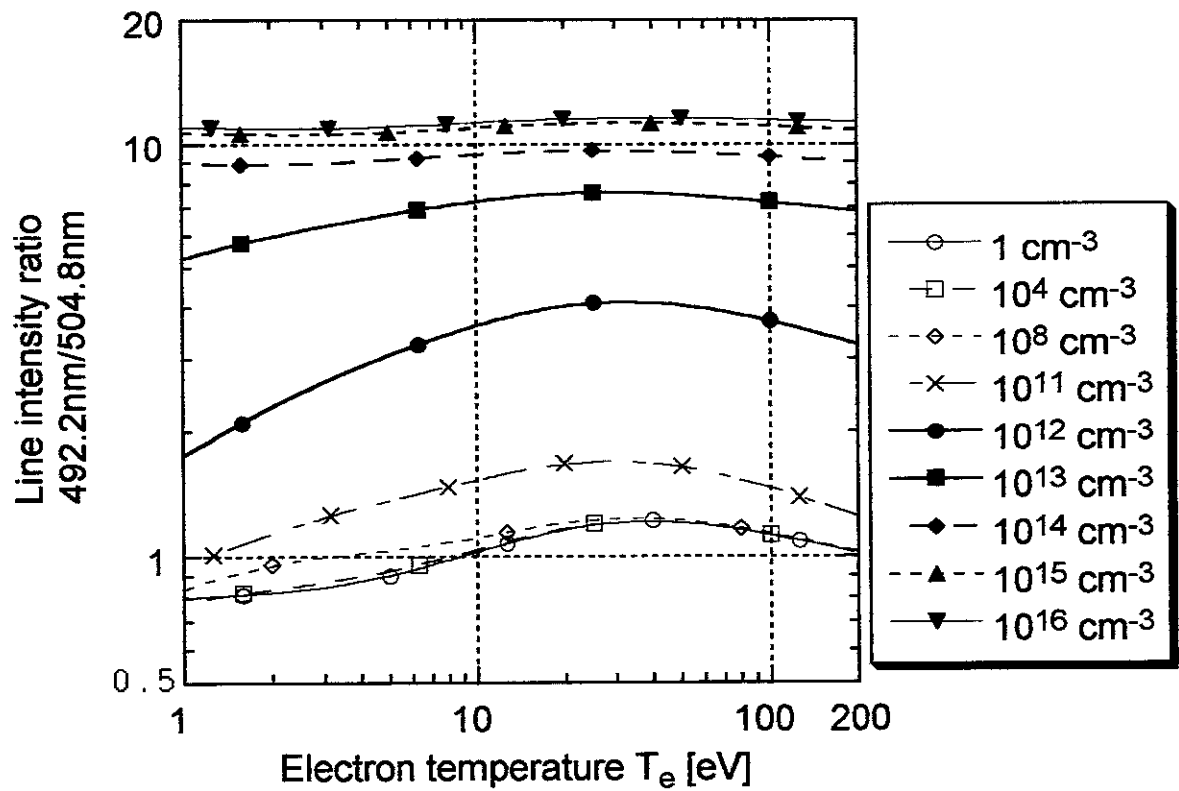


Fig. A6(b)

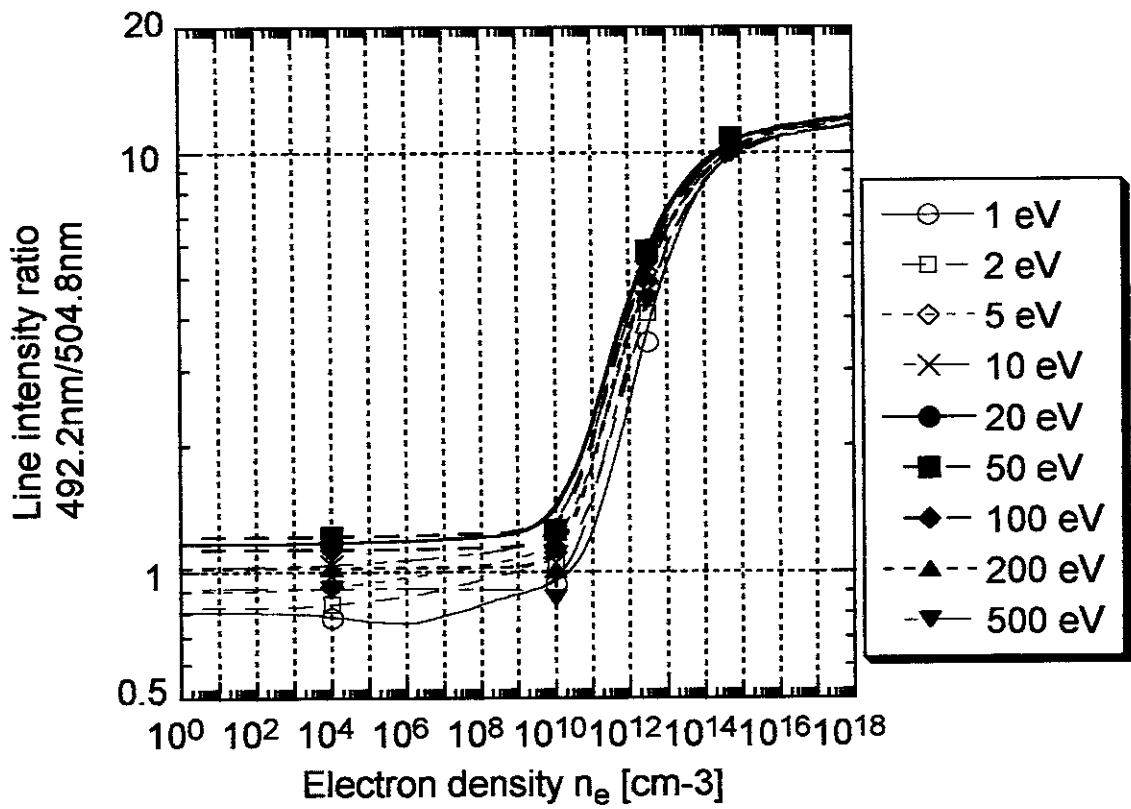


Fig. A6(c)

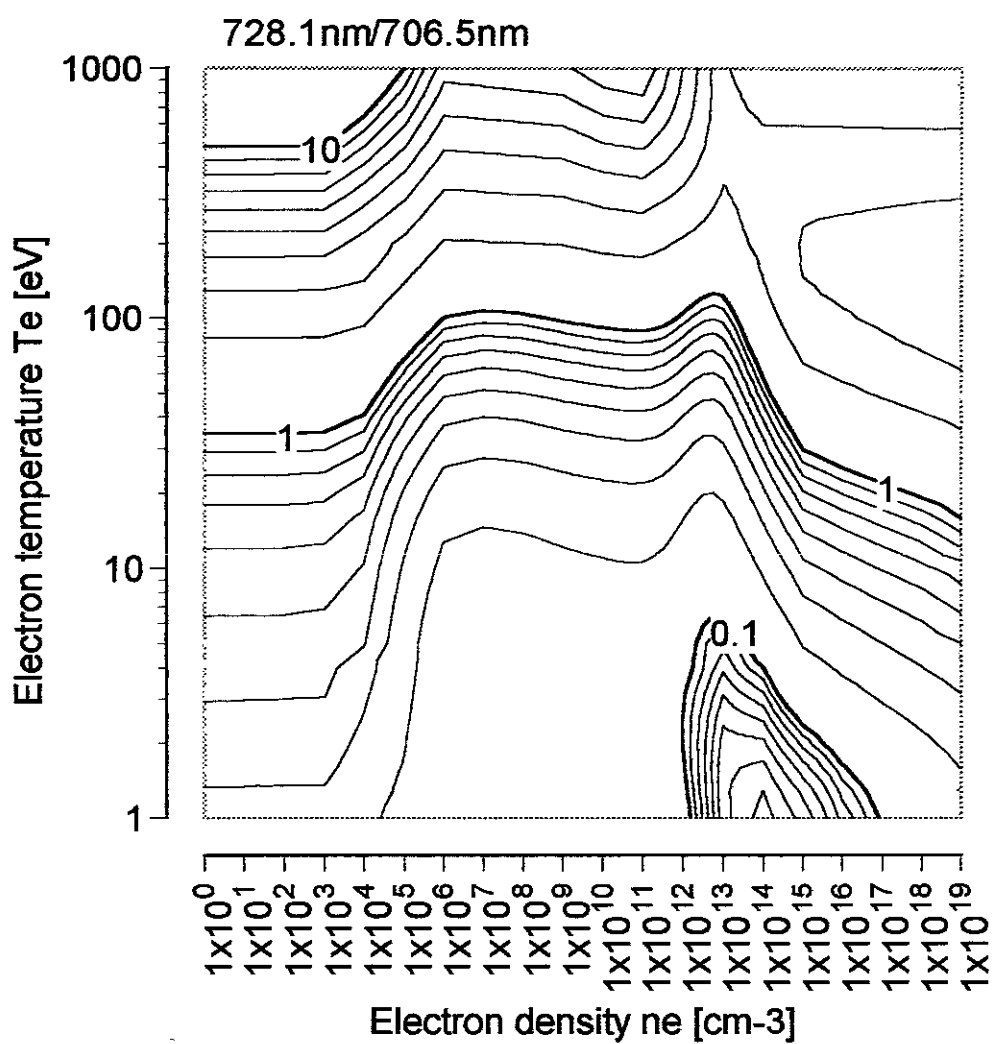


Fig. A7(a)

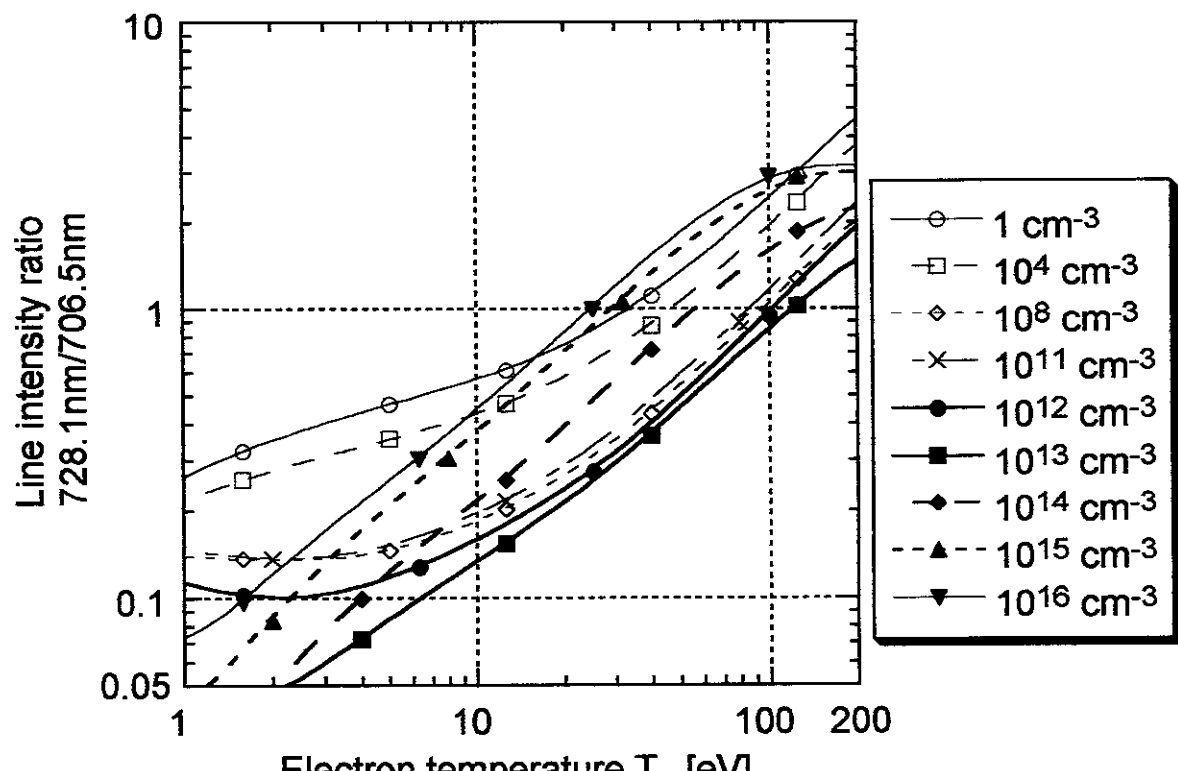


Fig. A7(b)

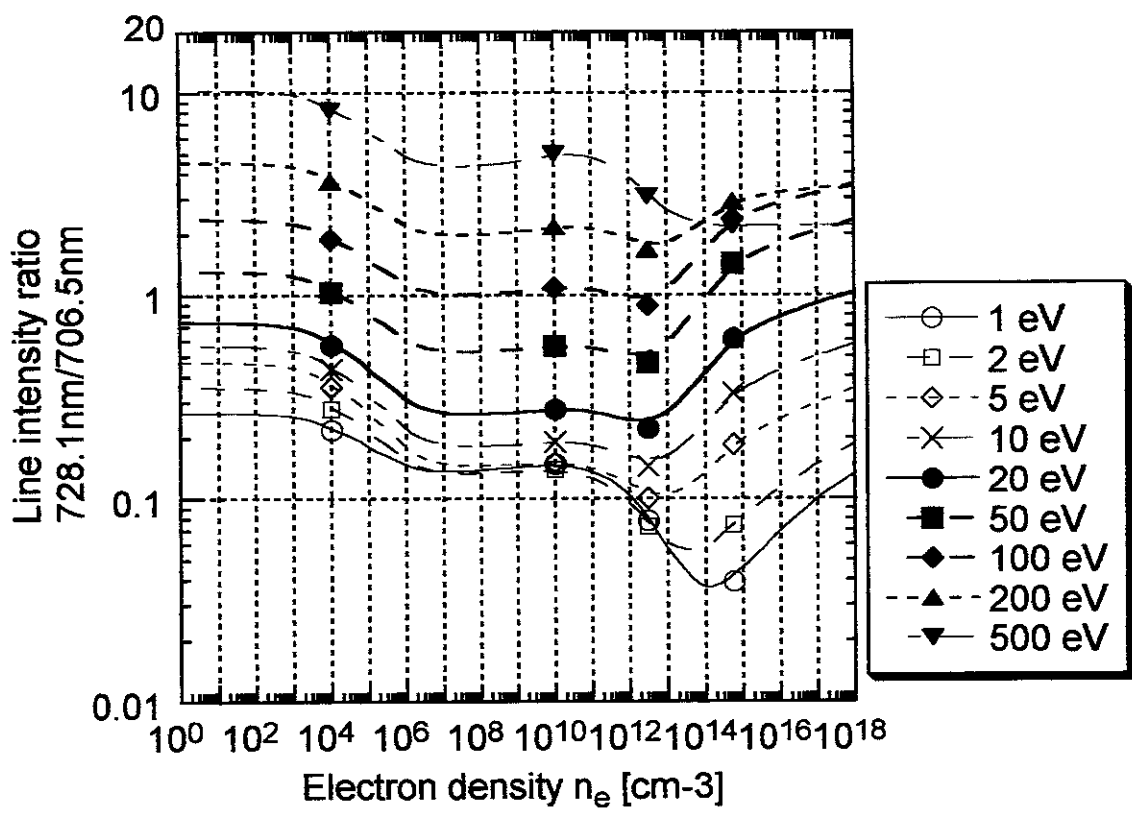


Fig. A7(c)

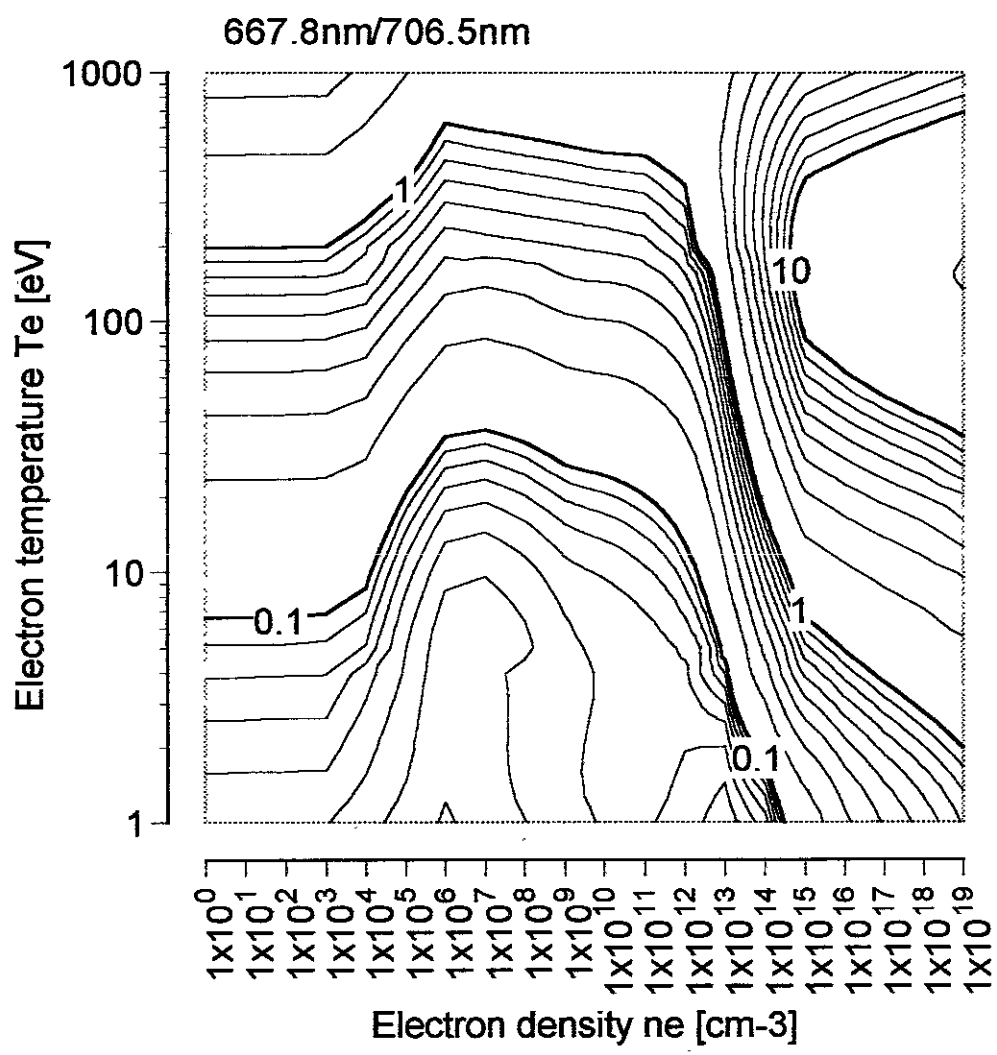


Fig. A8(a)

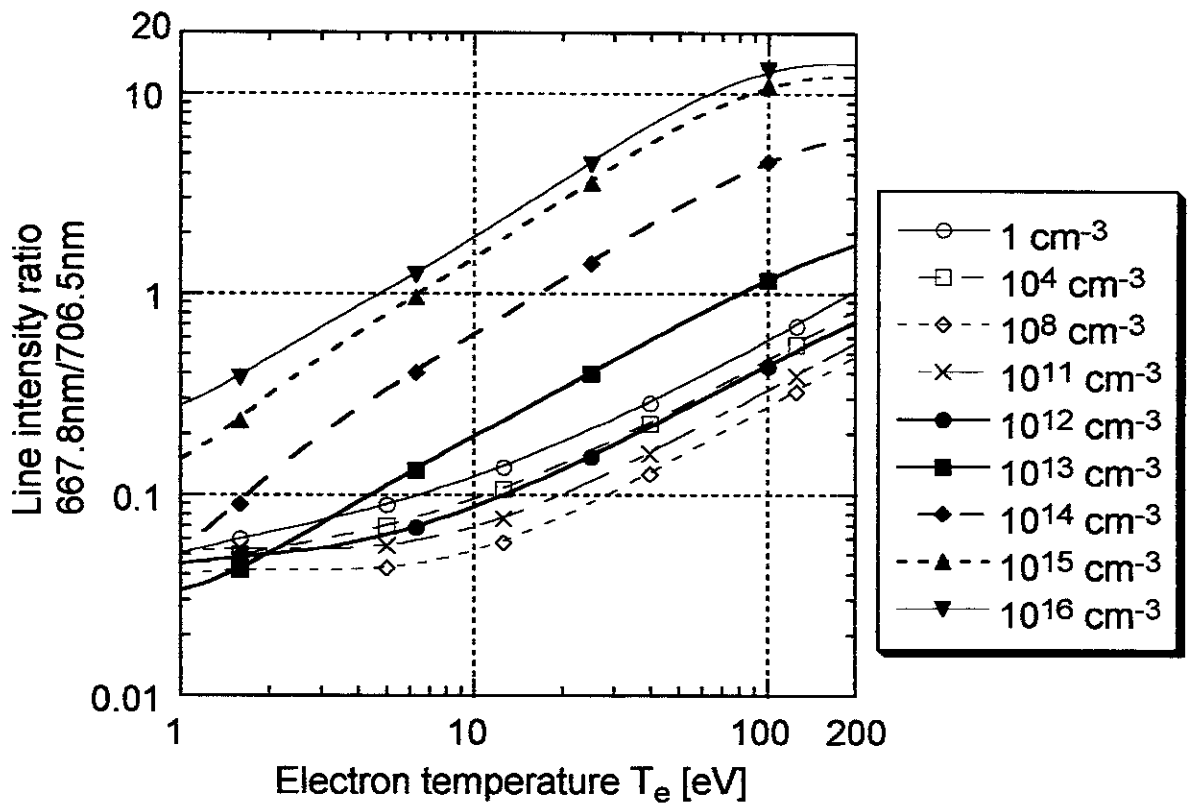


Fig A8(b)

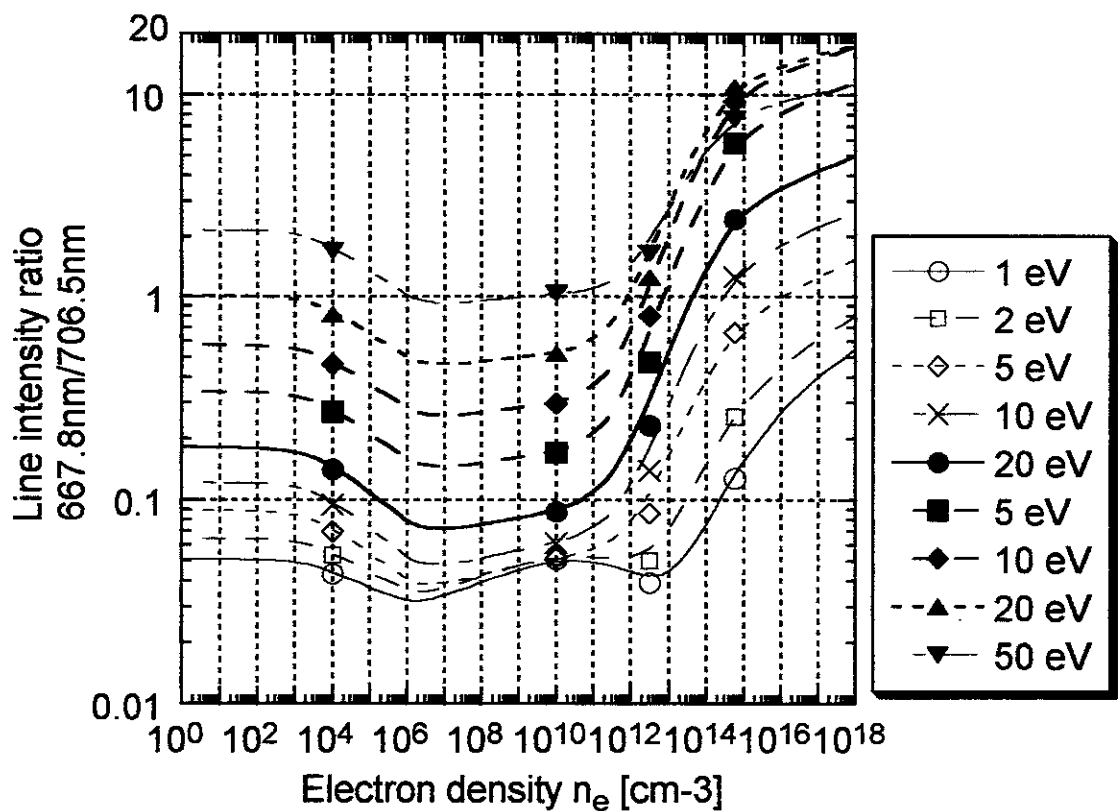


Fig. A8(c)

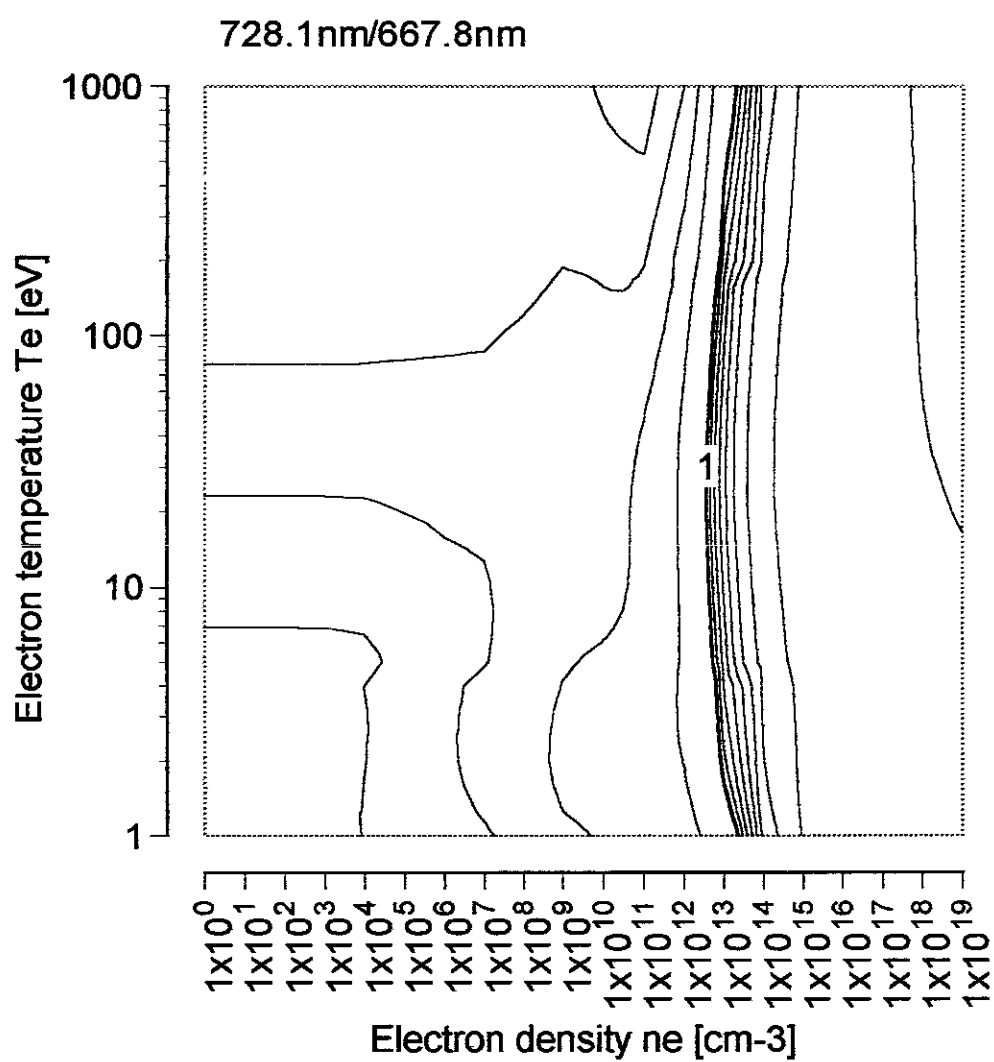


Fig. A9(a)

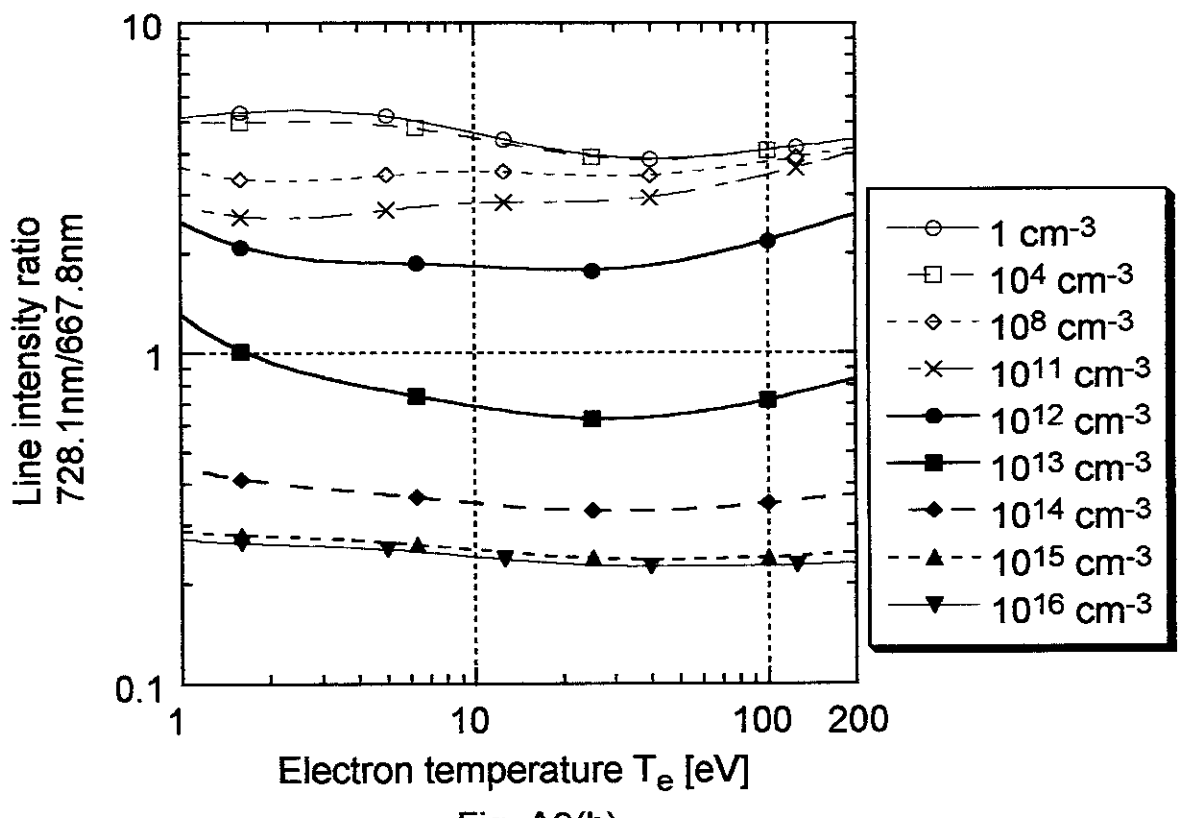


Fig. A9(b)

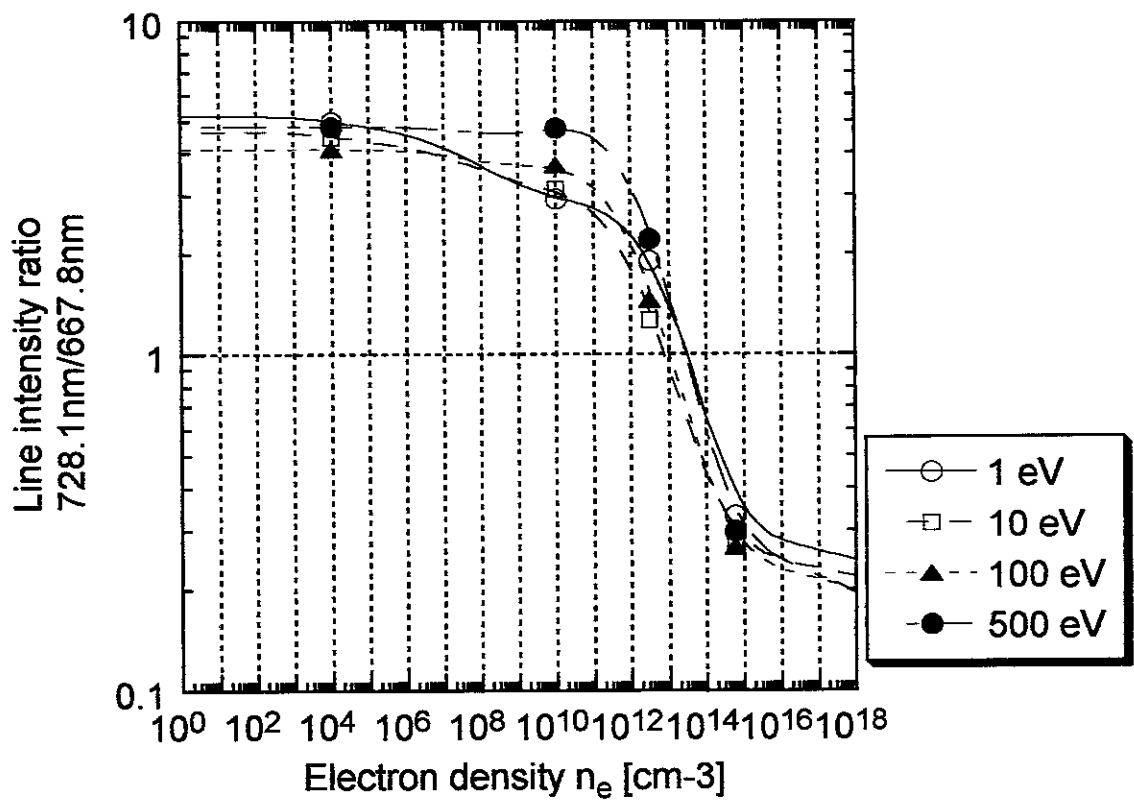


Fig. A9(c)

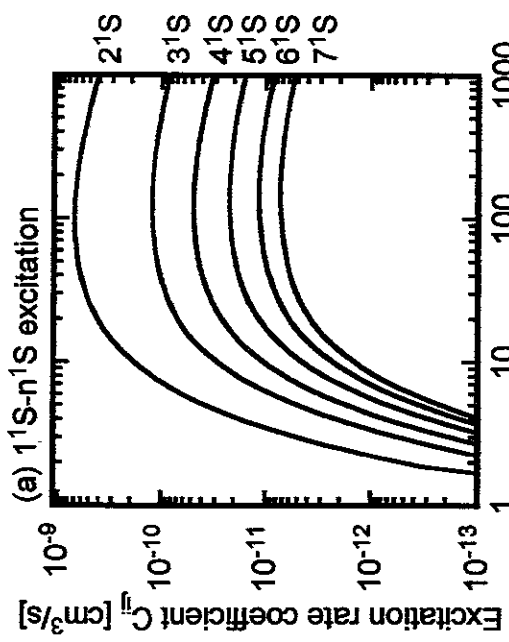


Fig. B1(a)

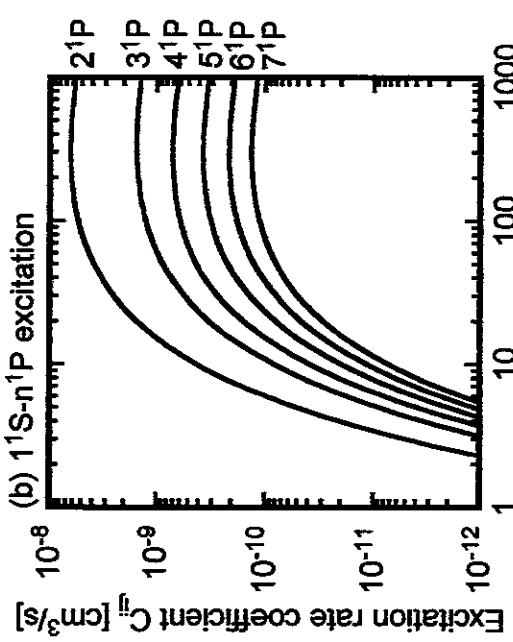


Fig. B1(b)

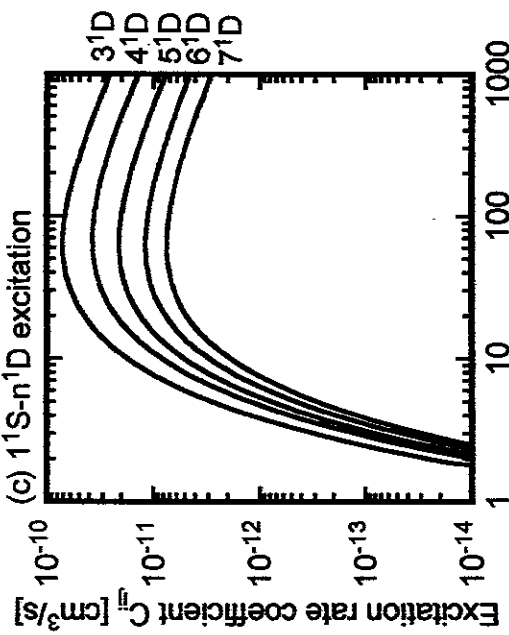


Fig. B1(c)

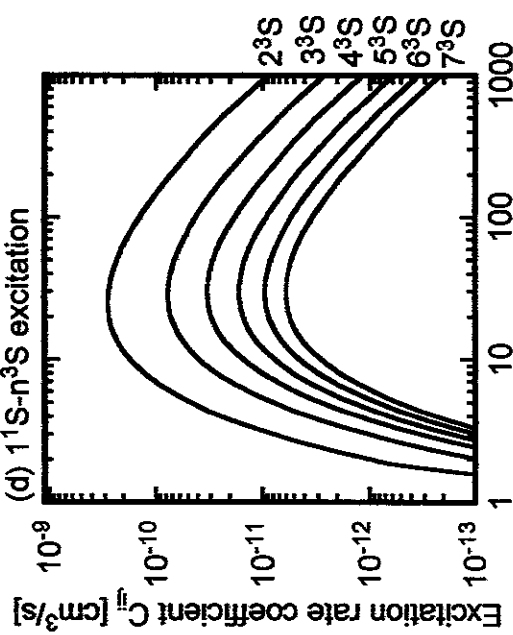


Fig. B1(d)

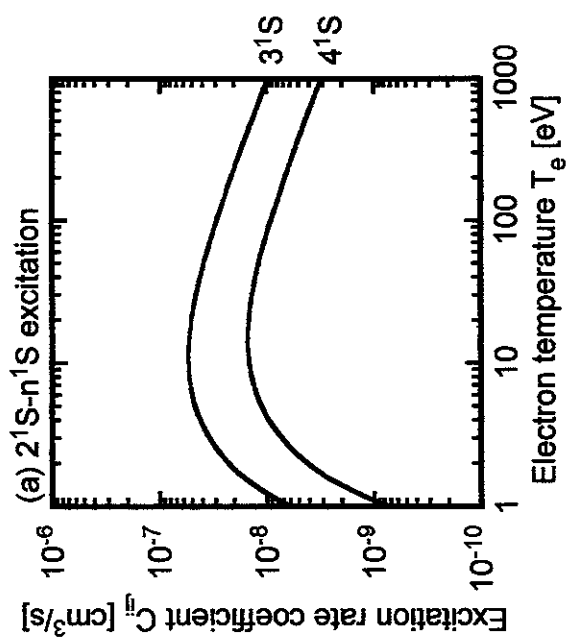


Fig. B2(a)

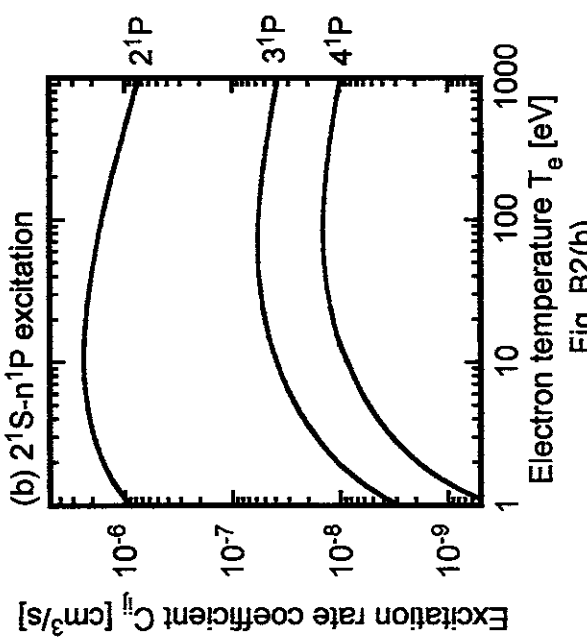


Fig. B2(b)

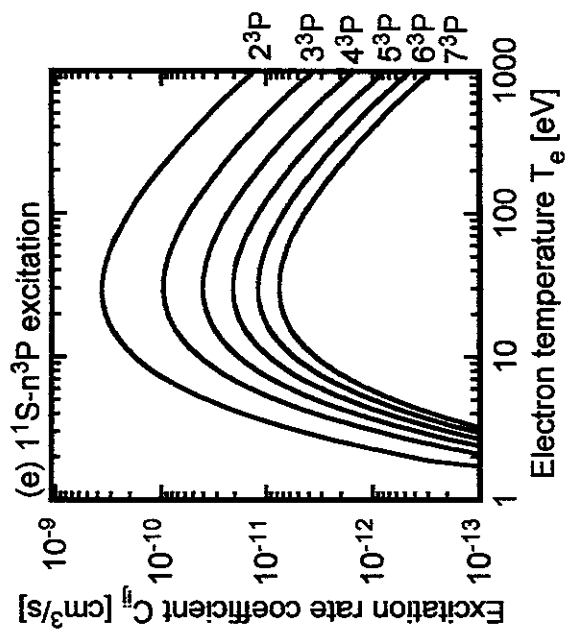


Fig. B1(e)

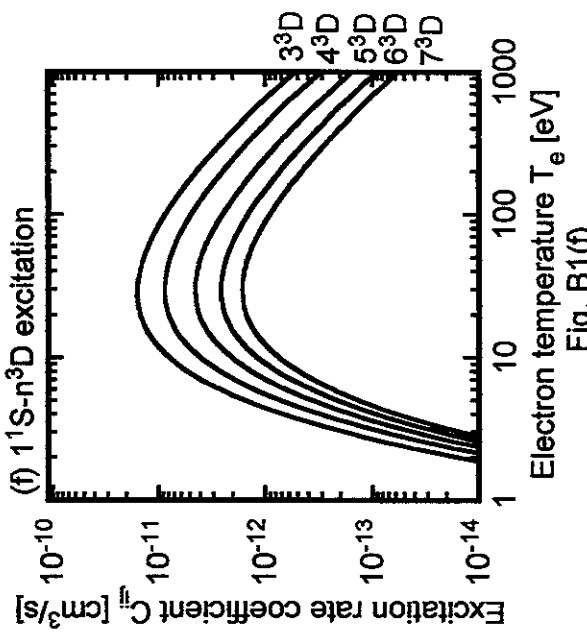


Fig. B1(f)

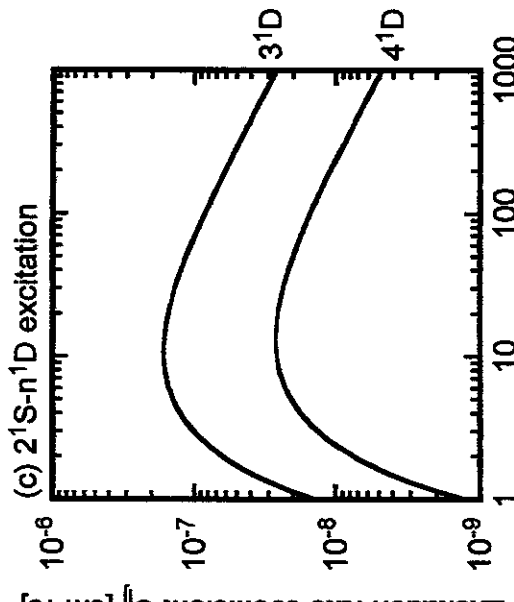


Fig. B2(c)

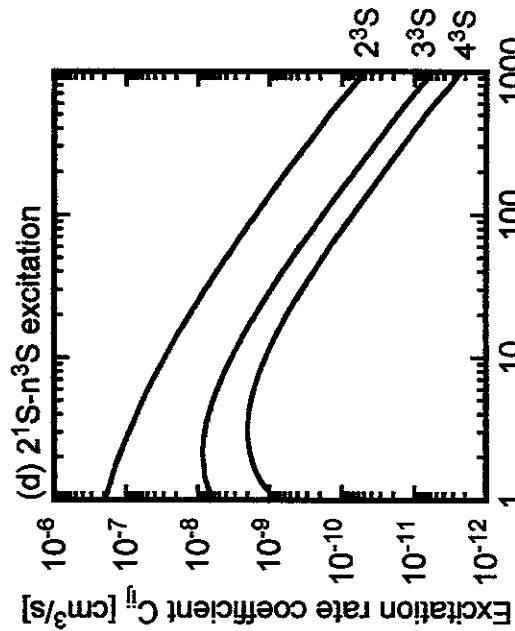


Fig. B2(d)

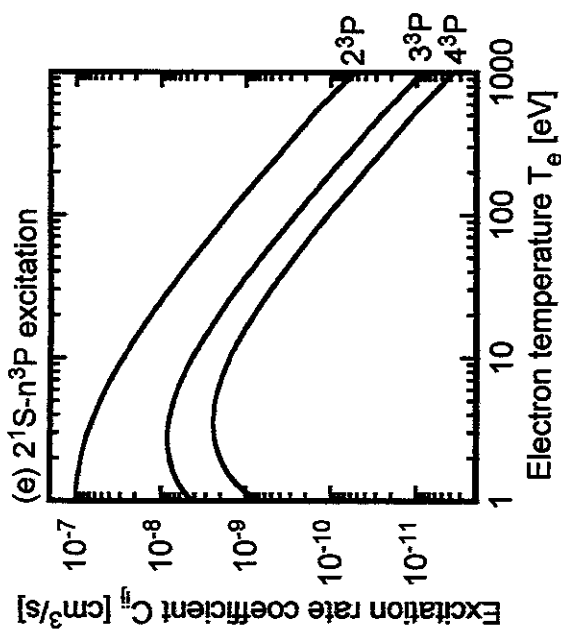


Fig. B2(e)

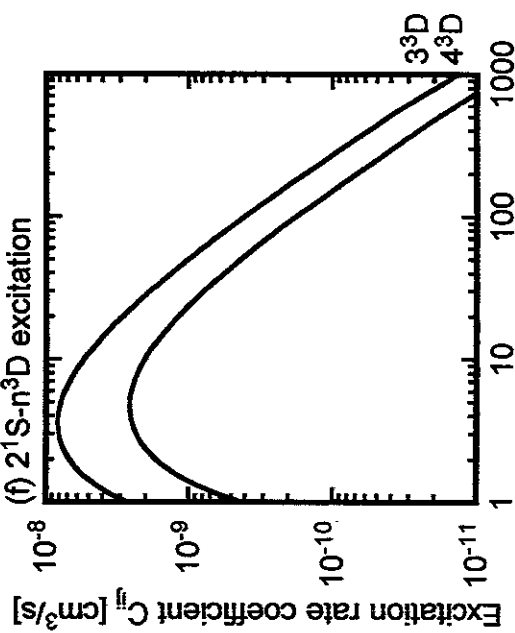


Fig. B2(f)

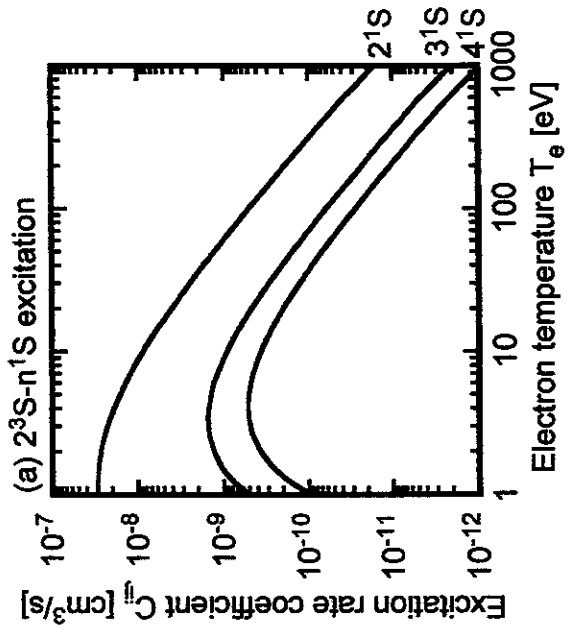


Fig. B3(a)

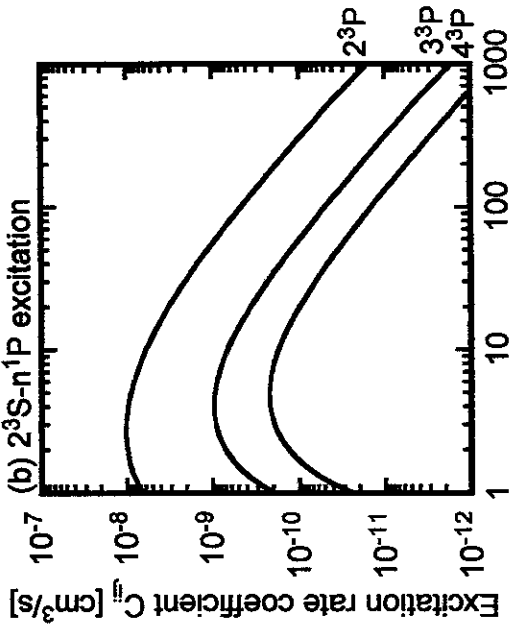


Fig. B3(b)

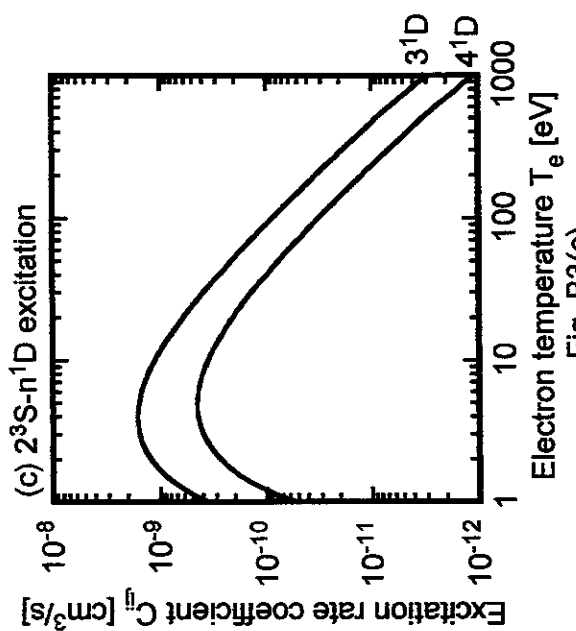


Fig. B3(c)

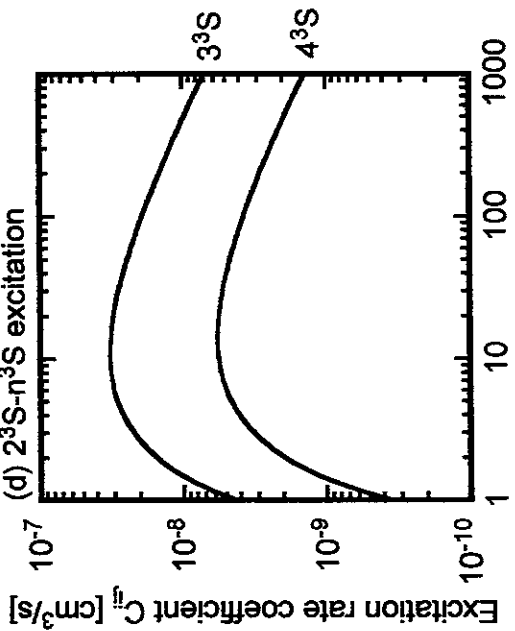


Fig. B3(d)

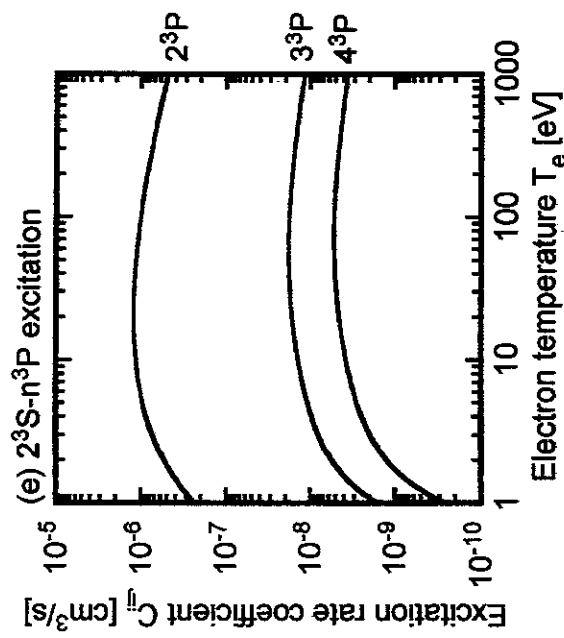


Fig. B3(e)

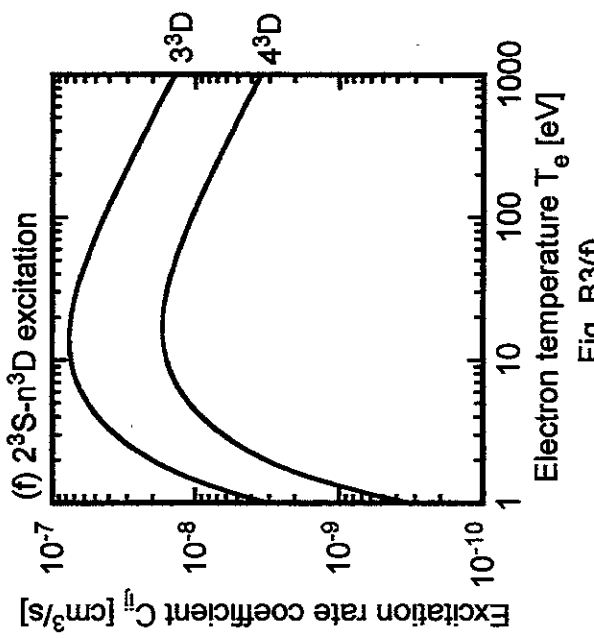


Fig. B3(f)

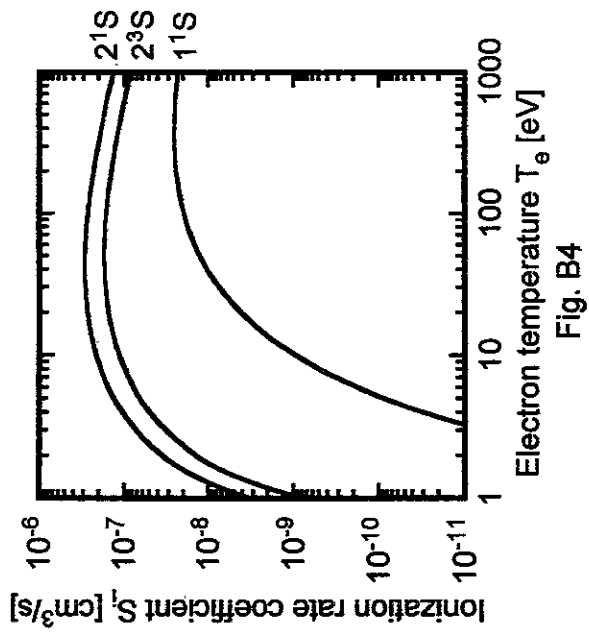


Fig. B4

Publication List of NIFS-DATA Series

- NIFS-DATA-1 Y. Yamamura, T. Takiguchi and H. Tawara,
Data Compilation of Angular Distributions of Sputtered Atoms; Jan. 1990
- NIFS-DATA-2 T. Kato, J. Lang and K. E. Berrington,
Intensity Ratios of Emission Lines from OV Ions for Temperature and Density Diagnostics ; Mar. 1990 [At Data and Nucl Data Tables 44(1990)133]
- NIFS-DATA-3 T. Kaneko,
Partial Electronic Straggling Cross Sections of Atoms for Protons; Mar. 1990
- NIFS-DATA-4 T. Fujimoto, K. Sawada and K. Takahata,
Cross Section for Production of Excited Hydrogen Atoms Following Dissociative Excitation of Molecular Hydrogen by Electron Impact ; Mar. 1990
- NIFS-DATA-5 H. Tawara,
Some Electron Detachment Data for H⁻ Ions in Collisions with Electrons, Ions, Atoms and Molecules – an Alternative Approach to High Energy Neutral Beam Production for Plasma Heating–; Apr. 1990
- NIFS-DATA-6 H. Tawara, Y. Itikawa, H. Nishimura, H. Tanaka and Y. Nakamura,
Collision Data Involving Hydro-Carbon Molecules ; July 1990 [Supplement to Nucl. Fusion 2(1992)25; Atomic and Molecular Processes in Magnetic Fusion Edge Plasmas (Plenum, 1995) p461]
- NIFS-DATA-7 H.Tawara,
Bibliography on Electron Transfer Processes in Ion-Ion/Atom/Molecule Collisions -Updated 1990-; Aug. 1990
- NIFS-DATA-8 U.I.Safranova, T.Kato, K.Masai, L.A.Vainshtein and A.S.Shlyapzeva,
Excitation Collision Strengths, Cross Sections and Rate Coefficients for OV, SiXI, FeXXIII, MoXXXIX by Electron Impact (1s²2s²-1s²2s2p-1s²2p² Transitions) Dec.1990
- NIFS-DATA-9 T.Kaneko,
Partial and Total Electronic Stopping Cross Sections of Atoms and Solids for Protons; Dec. 1990
- NIFS-DATA-10 K.Shima, N.Kuno, M.Yamanouchi and H.Tawara,
Equilibrium Charge Fraction of Ions of Z=4-92 (0.02-6 MeV/u) and Z=4-20 (Up to 40 MeV/u) Emerging from a Carbon Foil; Jan.1991 [AT.Data and Nucl. Data Tables 51(1992)173]
- NIFS-DATA-11 T. Kaneko, T. Nishihara, T. Taguchi, K. Nakagawa, M. Murakami, M. Hosono, S. Matsushita, K. Hayase, M. Moriya, Y.Matsukuma, K.Miura and Hiro Tawara,
Partial and Total Electronic StoppingCross Sections of Atoms for a Singly Charged Helium Ion: Part I;
Mar. 1991
- NIFS-DATA-12 Hiro Tawara,
Total and Partial Cross Sections of Electron Transfer Processes for Be⁹⁺ and B⁹⁺ Ions in Collisions with H, H₂ and He Gas Targets -Status in 1991-; June 1991
- NIFS-DATA-13 T. Kaneko, M. Nishikori, N. Yamato, T. Fukushima, T. Fujikawa, S. Fujita, K. Miki, Y. Mitsunobu, K. Yasuhara, H. Yoshida and Hiro Tawara,
Partial and Total Electronic Stopping Cross Sections of Atoms for a Singly Charged Helium Ion : Part II;
Aug. 1991
- NIFS-DATA-14 T. Kato, K. Masai and M. Arnaud,
Comparison of Ionization Rate Coefficients of Ions from Hydrogen through Nickel ; Sep. 1991
- NIFS-DATA-15 T. Kato, Y. Itikawa and K. Sakimoto,
Compilation of Excitation Cross Sections for He Atoms by Electron Impact; Mar. 1992
- NIFS-DATA-16 T. Fujimoto, F. Koike, K. Sakimoto, R. Okasaka, K. Kawasaki, K. Takiyama, T. Oda and T. Kato,
Atomic Processes Relevant to Polarization Plasma Spectroscopy , Apr. 1992
- NIFS-DATA-17 H. Tawara,

Electron Stripping Cross Sections for Light Impurity Ions in Colliding with Atomic Hydrogens Relevant to Fusion Research; Apr. 1992

- NIFS-DATA-18 T. Kato,
Electron Impact Excitation Cross Sections and Effective Collision Strengths of N Atom and N-Like Ions -A Review of Available Data and Recommendations- ; Sep. 1992 [Atomic Data and Nuclear Data Tables, 57, 181-214 (1994)]
- NIFS-DATA-19 Hiro Tawara,
Atomic and Molecular Data for H₂O, CO & CO₂ Relevant to Edge Plasma Impurities , Oct. 1992
- NIFS-DATA-20 Hiro. Tawara,
Bibliography on Electron Transfer Processes in Ion-Ion/Atom/Molecule Collisions -Updated 1993-; Apr. 1993
- NIFS-DATA-21 J. Dubau and T. Kato,
Dielectronic Recombination Rate Coefficients to the Excited States of C I from C II; Aug. 1994
- NIFS-DATA-22 T. Kawamura, T. Ono, Y. Yamamura,
Simulation Calculations of Physical Sputtering and Reflection Coefficient of Plasma-Irradiated Carbon Surface; Aug. 1994 [J. Nucl. Mater., 220 (1995) 1010]
- NIFS-DATA-23 Y. Yamamura and H. Tawara,
Energy Dependence of Ion-Induced Sputtering Yields from Monoatomic Solids at Normal Incidence; Mar. 1995 [At. Data and Nucl. Data Tables, 62 (1996) 149]
- NIFS-DATA-24 T. Kato, U. Safranova, A. Shlyaptseva, M. Cornille, J. Dubau,
Comparison of the Satellite Lines of H-like and He-like Spectra; Apr. 1995 [Atomic Data and Nuclear Data Tables, 67., 225 (1997)]
- NIFS-DATA-25 H. Tawara,
Roles of Atomic and Molecular Processes in Fusion Plasma Researches - from the cradle (plasma production) to the grave (after-burning) -; May 1995
- NIFS-DATA-26 N. Toshima and H. Tawara
Excitation, Ionization, and Electron Capture Cross Sections of Atomic Hydrogen in Collisions with Multiply Charged Ions; July 1995
- NIFS-DATA-27 V.P. Shevelko, H. Tawara and E.Salzborn,
Multiple-Ionization Cross Sections of Atoms and Positive Ions by Electron Impact; July 1995 [Suppl. Nucl. Fusion, 6 (1996) 101]
- NIFS-DATA-28 V.P. Shevelko and H. Tawara,
Cross Sections for Electron-Impact Induced Transitions Between Excited States in He: n, n'=2,3 and 4; Aug. 1995 [Suppl. Nucl. Fusion, 6 (1996) 27]
- NIFS-DATA-29 U.I. Safranova, M.S. Safranova and T. Kato,
Cross Sections and Rate Coefficients for Excitation of Δn = 1 Transitions in Li-like Ions with 6<Z<42; Sep. 1995 [Physica Scripta, 54, 68-84 (1996)]
- NIFS-DATA-30 T. Nishikawa, T. Kawachi, K. Nishihara and T. Fujimoto,
Recommended Atomic Data for Collisional-Radiative Model of Li-like Ions and Gain Calculation for Li-like Al Ions in the Recombining Plasma; Sep. 1995
- NIFS-DATA-31 Y. Yamamura, K. Sakaoka and H. Tawara,
Computer Simulation and Data Compilation of Sputtering Yield by Hydrogen Isotopes (¹H⁺, ²D⁺, ³T⁺) and Helium (⁴He⁺) Ion Impact from Monatomic Solids at Normal Incidence; Oct. 1995
- NIFS-DATA-32 T. Kato, U. Safranova and M. Ohira,
Dielectronic Recombination Rate Coefficients to the Excited States of CII from CIII; Feb. 1996 [Physica Scripta, 53, 461-472 (1996), Physica Scripta, 55, 185-199 (1997)]
- NIFS-DATA-33 K.J. Snowdon and H. Tawara,
Low Energy Molecule-Surface Interaction Processes of Relevance to Next-Generation Fusion Devices;

Mar. 1996 [Comm. At. Mol. Opt. Phys. 34 (1998) 21]

- NIFS-DATA-34 T. Ono, T. Kawamura, K. Ishii and Y. Yamamura,
Sputtering Yield Formula for B₄C Irradiated with Monoenergetic Ions at Normal Incidence; Apr. 1996 [J. Nucl. Mater., 232 (1996) 52]
- NIFS-DATA-35 I. Murakami, T. Kato and J. Dubau,
UV and X-Ray Spectral Lines of Be-Like Fe Ion for Plasma Diagnostics; Apr. 1996 [Physica Scripta, 54, 463-470 (1996)]
- NIFS-DATA-36 K. Moribayashi and T. Kato,
Dielectronic Recombination of Be-like Fe Ion; Apr. 1996 [Physica Scripta. Vol.55, 286-297 (1997)]
- NIFS-DATA-37 U. Safronova, T. Kato and M. Ohira,
Dielectronic Recombination Rate Coefficients to the Excited States of CII from CIV; July 1996 [J. Quant. Spectrosc. Radiat. Transfer, 58, 193 - 215, (1997)]
- NIFS-DATA-38 T. Fujimoto, H. Sahara, G. Csanak and S. Grabbe,
Atomic States and Collisional Relaxation in Plasma Polarization Spectroscopy: Axially Symmetric Case; Oct. 1996
- NIFS-DATA-39 H. Tawara (Ed.)
Present Status on Atomic and Molecular Data Relevant to Fusion Plasma Diagnostics and Modeling; Jan. 1997
- NIFS-DATA-40 Inga Yu. Tolstikhina,
LS-Averaged I/Z Method as a Tool of Studying the Interactions of Highly Charged Ions with a Metal Surface; Jan. 1997
- NIFS-DATA-41 K. Moribayashi and T. Kato,
Atomic Nuclear Charge Scaling for Dielectronic Recombination to Be-like Ions; Apr. 1997
- NIFS-DATA-42 H. Tawara,
Bibliography on Electron Transfer Processes in Ion-ion / Atom / Molecule Collisions -Updated 1997 -; May 1997
- NIFS-DATA-43 M. Goto and T. Fujimoto,
Collisional-radiative Model for Neutral Helium in Plasma: Excitation Cross Section and Singlet-triplet Wavefunction Mixing; Oct. 1997
- NIFS-DATA-44 J. Dubau, T. Kato and U.I. Safronova,
Dielectronic Recombination Rate Coefficients to the Excited States of CI From CII; Jan. 1998
- NIFS-DATA-45 Y. Yamamura, W. Takeuchi and T. Kawamura,
The Screening Length of Interatomic Potential in Atomic Collisions; Mar. 1998
- NIFS-DATA-46 T. Kenmotsu, T. Kawamura, T. Ono and Y. Yamamura,
Dynamical Simulation for Sputtering of B4C; Mar. 1998
- NIFS-DATA-47 I. Murakami, K. Moribayashi and T. Kato,
Effect of Recombination Processes on FeXXIII Line Intensities; May 1998
- NIFS-DATA-48 Zhijie Li, T. Kenmotsu, T. Kawamura, T. Ono and Y. Yamamura,
Sputtering Yield Calculations Using an Interatomic Potential with the Shell Effect and a New Local Model; Oct. 1998
- NIFS-DATA-49 S. Sasaki, M. Goto, T. Kato and S. Takamura,
Line Intensity Ratios of Helium Atom in an Ionizing Plasma; Oct. 1998